This is to certify that the
dissertation entitled

PROTON CONDUCTING MATERIALS: SYNTHESIS,
CHARACTERIZATION, AND APPLICATION IN FUEL CELLS

presented by

QIN YUAN

has been accepted towards fulfillment
of the requirements for the

DOCTORAL degree in CHEMISTRY

Major Professor's Signature

15 December 2009

Date

PROTON CONDUCTING MATERIALS: SYNTHESIS, CHARACTERIZATION, AND APPLICATION IN FUEL CELLS

By

Qin Yuan

A DISSERTATION

Submitted to
Michigan State University
in partial fulfillment of the requirements
for the degree of

DOCTOR OF PHILOSOPHY

Chemistry

2009

ABSTRACT

PROTON CONDUCTING MATERIALS:
SYNTHESIS, CHARACTERIZATION, AND APPLICATION IN FUEL CELLS

By

Qin Yuan

Recently, there has been considerable interest in the development of fuel cells, especially hydrogen powered fuel cells, which cleanly convert the chemical energy of fuels directly into electric energy and heat with high efficiency. A key component of hydrogen based fuel cells is the proton exchange membrane (PEM), which transports protons from the anode to the cathode and separates fuel and oxidant. Nafion, the prototype PEM, has a high proton conductivity and chemical and mechanical stability at moderate temperatures in the harsh fuel cell environment. Despite the high performance of Nafion in fuel cells, its high manufacturing cost, drastically reduced proton conductivity above 80 °C, environmental incompatibility, and severe methanol permeability limit its use in fuel cell applications.

We synthesized poly(sodium 4-styrenesulfonate)-coated silica nanoparticles via surface initiated atom transfer radical polymerization (ATRP). After acidification, we used a solution-casting process to embed the proton conducting nanoparticles in a poly(vinylidene fluoride) (PVDF) matrix. In this blend PEM system, the silica nanoparticles were the proton transport medium, while PVDF gave the membrane favorable mechanical properties: toughness, resilience, and minimal swelling. The proton conductivities were comparable to

Nafion 117, and depended on the volume fraction of the nanoparticles in the membarne.

We also synthesized uniform magnetic nanoparticles with magnetite cores, a silica buffer layer, and poly(4-styrenesulfonic acid) grown from the particle surfaces. Applying an external magnetic field during membrane casting aligned the particles in the through-plane direction, increasing the conductivity for a given volume fraction of particles. These "magnetic" PEMs had higher conductivity and better dimensional stability than Nafion 117.

Sulfonated polyimides (SPIs) have proven to be one of the best alternatives to Nafion due to their excellent thermal, chemical, and mechanical stability, high proton conductivity, good film-forming ability, and low gas permeability. Using a polycondensation reaction, we synthesized a SPI and prepared PEMs from the SPI/PVDF blends. Transmission electron microscopy showed that the blends have a phase-separated morphology that evolved into a bicontinuous morphology when the SPI weight fraction exceeded 30 %. The conductivities were comparable to those of Nafion 117. These blends are good candidates for high temperature fuel cell applications.

To my family

ACKNOWLEDGMENTS

I would like to sincerely thank my advisor, Dr. Gregory Baker for his guidance, assistance, and patience. My five-year experience in the Baker group is one of the most important treasures in my life. I would like to thank my committee members, Dr. William Wulff, Dr. Chi-Kwong Chang, and Dr. Merlin Bruening for their guidance and helpful suggestions.

My thanks go to both previous and current Baker group members: Xuwei, Ping, Ying, Leslie, Feng, Bao, DJ, Erin, Sampa, Tom, Hui, Gina, Quanxuan, Heyi, Wen, and Yiding and all my friends at Michigan State University. Thanks to Dan Holmes, Kathy Severin, Riu Huang, and Alicia Pastor for their help on various instruments.

Finally, I would like to thank my family for always believing in me and my husband, Jun, for his love, support, and encouragement. I have benefited a lot from his polymer background.

TABLE OF CONTENTS

LIST OF TABLES

LIST OF FIGURES

LIST OF SCHEMES

Images in this dissertation are presented in color.

LIST OF ABBREVIATIONS

σ	conductivity
A	ampere
AC	alternating current
AFM	atomic force microscopy
BPSH	bisulfonated poly(arylene ether sulfone)
CTAB	cetyltrimethylammonium bromide
Da	Dalton
DMF	dimethylformamide
DMFC	direct methanol fuel cell
DEG	diethylene glycol
DMSO	dimethyl sulfoxide
DSC	differential scanning calorimetry
EDX	dispersive X-ray
EFTEM	energy-filtered transmission electron microscopy
emu	electromagnetic unit
Et_3N (TEA)	triethyl amine
GPC	gel permeation chromatography
h	hour
Hz	hertz
IEC	ion exchange capacity
IR	infrared spectroscopy
mA	miliampere

m	meta
M	mole per liter
$[M]_o$	initial monomer concentration
meq	milliequivalent
MHz	megahertz
MNT	magnetite
M_n	number average molecular weight
M_w	weight average molecular weight
NaSS	sodium 4-styrenesulfonate
NBIm	4-nitrobenzimidazole
NMR	nuclear magnetic resonance
Oe	oersted
p	para
ppm	parts per million
PAA	poly(acrylic acid)
PDDA	poly(diallyldimethylammonium chloride)
PDI	polydispersity index
PEI	poly(ether imide)
PEM	proton exchange membrane
PEO	poly(ethylene oxide)
PES	poly(ether sulfone)
PI	polyimide
PMB	poly(methylbutylene)
PMMA	poly(methyl mathacrylate)

PSf	polysulfone
PSS	poly(styrenesulfonate)
PSSA	sulfonated polystyrene
PSSH	poly(4-styrenesulfonic acid)
PSSNa	poly(sodium 4-styrenesulfonate)
PSt	polystyrene
PVDF	poly(vinylidene fluoride)
rt	room temperature
RH	relative humidity
S	Siemens
SEM	scanning electron microscopy
SPEEK	sulfonated poly(ether ether ketone)
SPEKK	sulfonated poly(ether ketone ketone)
SPI	sulfonated polyimide
t	reaction time
T	temperature
TEOS	tetraethyl orthosilicate
TEM	transmission electron microscopy
T_g	glass transition temperature
TGA	thermal gravimetric analysis
THF	tetrahydrofuran
V	volts
XRD	X-ray diffraction

Chapter 1 Introduction

Recently, there has been considerable interest in the development of fuel cells, especially hydrogen powered fuel cells, which cleanly convert the chemical energy of fuels directly into electric energy and heat with high efficiency. The proton exchange membrane (PEM), which transports protons from the anode to the cathode and acts as a separator to prevent mixing of reactant gases, is one of the most important components of hydrogen fuel cells.[1] Currently, the state-of-the-art PEM is Nafion which was commercialized by DuPont in the late 1960s. As shown in **Figure 1**, Nafion has a perfluorinated backbone with pendent fluorosulfonic acids and has demonstrated excellent performance in the harsh fuel cell environment.[2] In PEM fuel cells, Nafion can continuously work for up to 60,000 h with high conductivity (80 mS/cm) at 80 °C.[3] Nafion's outstanding performance as a PEM has spurred researchers to study the morphology of hydrated Nafion, and by inference, the mechanism responsible for its proton conductivity.

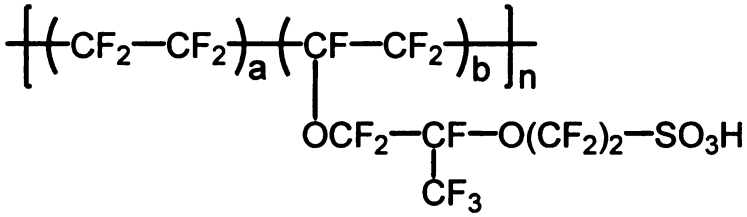

Figure 1. Chemical structure of Nafion.

Nafion conducting mechanism

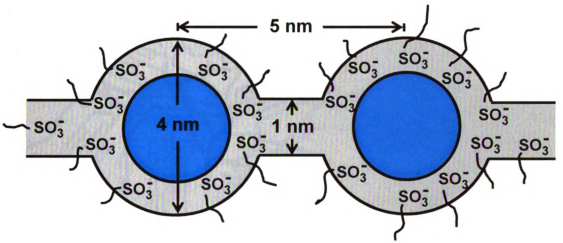

Figure 2. Gierke's cluster-network model for the morphology of hydrated Nafion.[4]

A common starting point for understanding hydrated Nafion is Gierke's cluster model.[5-7] Gierke *et al.* proposed that water-swollen Nafion is comprised of approximately spherical ionic clusters with an inverted micelle structure, interconnected by small channels to form a continuous conductive pathway as shown in **Figure 2**. As the water content increases, the ionic clusters grow and combine into larger but fewer clusters in fully hydrated Nafion materials. Though the cluster-network model has been widely used to explain Nafion's morphology-performance relationships, recent experiments have inspired alternative models for Nafion's morphology. Rubata and co-workers introduced a polymer-bundle model, where elongated polymeric aggregates are surrounded with ionic charges (**Figure 3**).[8-10] The local orientation for these aggregates had a correlation length of a few hundreds of nanometers at both high and low hydration levels. The main difference from the Gierke model is that water molecules are located in an intrinsic fibrillar structure rather than spherical cavities.

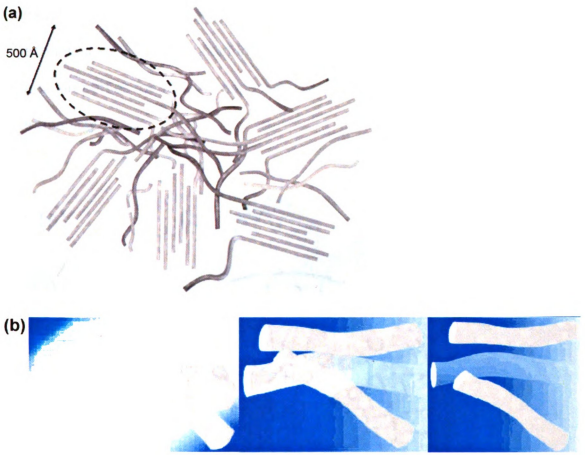

Figure 3. Polymer-bundle model. **(a)** Schematic view of polymer aggregate domains inside a bundle. **(b)** Schematic view of nanoscopic swelling between three polymer aggregates inside a bundle with different water contents. (from almost dry membrane (left) up to diluted solution (right)). (Reprinted with permission from *Macromolecules* **2004**, *37*, 7772-7783. Copyright 2004 American Chemical Society)

The recent work of Schmidt-Rour supports a parallel water-channel model for Nafion.[11] They proposed that hydrophilic side groups align to form water channels with an average diameter of 2.4 nm (**Figure 4b**). The channels were stabilized by stiff hydrophobic backbone segments surrounding the channels, resulting in a cylindrical inverted micelle structure (**Figure 4a**). Consistent with other models,[6,12] the Schmidt-Rour model gave a 10-20 nm repeat length between crystallites. The crystallites are an important component in Nafion's

structure as they function as physical cross-links responsible for Nafion's mechanical stability, as shown in **Figure 4c**. The water-channel model explains many properties of Nafion, especially its high proton conductivity and water permeability.[13]

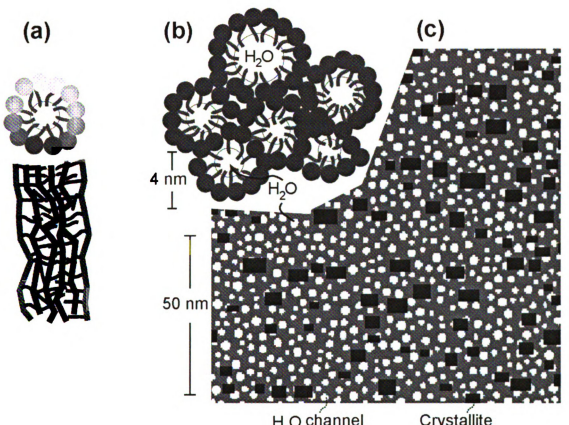

Figure 4. Parallel water-channel model of Nafion. **(a)** Two views of an inverted-micelle cylinder, with ionic side chains filling the water channel and hydrophobic polymer backbone on the outside. **(b)** Schematic view of the approximately hexagonal packing of inverted-micelle cylinders. **(c)** Cross-sections through water channels (white) and crystallites (black) in the non-crystalline Nafion matrix. (Reprinted with permission from *Nat. Mater.* **2008**, *7*, 75-83. Copyright 2007 Nature Publishing Group)

Though the actual morphology of hydrated Nafion is still under investigation, it is widely agreed that Nafion's phase separation into two domains

accounts for its high proton conductivity.[4,14,15] The two domains function separately: the hydrophilic domain affords proton transport while the hydrophobic domain provides mechanical and chemical stability. This has been confirmed by the work of Xu and coworkers, who found that when Nafion was dissolved and recast into membranes, its proton conductivity was four orders of magnitude lower due to the break-down of Nafion's phase-separated structure.[16] Despite having favorable PEM characteristics for fuel cell applications, Nafion has significant drawbacks. The most critical limitation is its high price, which is a significant cost of a fuel cell device and has limited the market penetration.[17] Also, its poor performance in direct methanol fuel cells (DMFCs), and a drastic decrease in proton conductivity at elevated temperatures and/or low humidity limit Nafion to applications to temperatures <90 °C.[1,2]

For applications in automotive, stationary, and portable power areas, PEMs must satisfy several critical requirements including (1) high proton conductivity (>10 mS/cm at 25 °C), (2) low electronic conductivity, (3) good chemical, mechanical and thermal stability, (4) low permeability to fuel and oxidant, and (5) low cost (<$200/m^2).[18] For fuel cells to replace combustion engines, the U.S. Department of Energy has set a target for PEM performance: a proton conductivity of 100 mS/cm at operating conditions of 120 °C and 50 % relative humidity.

Extensive research has focused on modifying Nafion to overcome the drawbacks of Nafion and make it more suitable for fuel cell applications, as well as developing alternatives to Nafion.

Inorganic-Nafion composite membranes

Silicon oxide nanoparticles

SiO_2 has been extensively explored as an additive to enhance Nafion's physical properties.[19-25] Nafion/silica composite membranes were prepared by the addition of silica nanoparticles or sol-gel polymerization of silica precursors catalyzed by the sulfonic acid groups of Nafion. The as-synthesized membranes were reported to have outstanding performance at high temperatures. For example, organic-inorganic hybrid Nafion membranes were synthesized via an in situ sol-gel process, which formed mesoporous silica with sulfonic acid groups (**Figure 5**).[19] The mesoporous silica resulted from the co-condensation of tetraethoxysilane and 2-(4-chlorosulfonylphenyl)ethyltrimethoxysilane during the recasting of Nafion membranes, using an organic surfactant as the template. The homogeneous composite membranes had improved dimensional stability and water management compared to conventional Nafion membranes. More importantly, including silica in the membrane increased the proton conductivity at 95 °C and over the entire range of relative humidity, compared to recast Nafion and Nafion 112 membranes, which was ascribed to the presence of the hygroscopic inorganic silica phase within the Nafion.

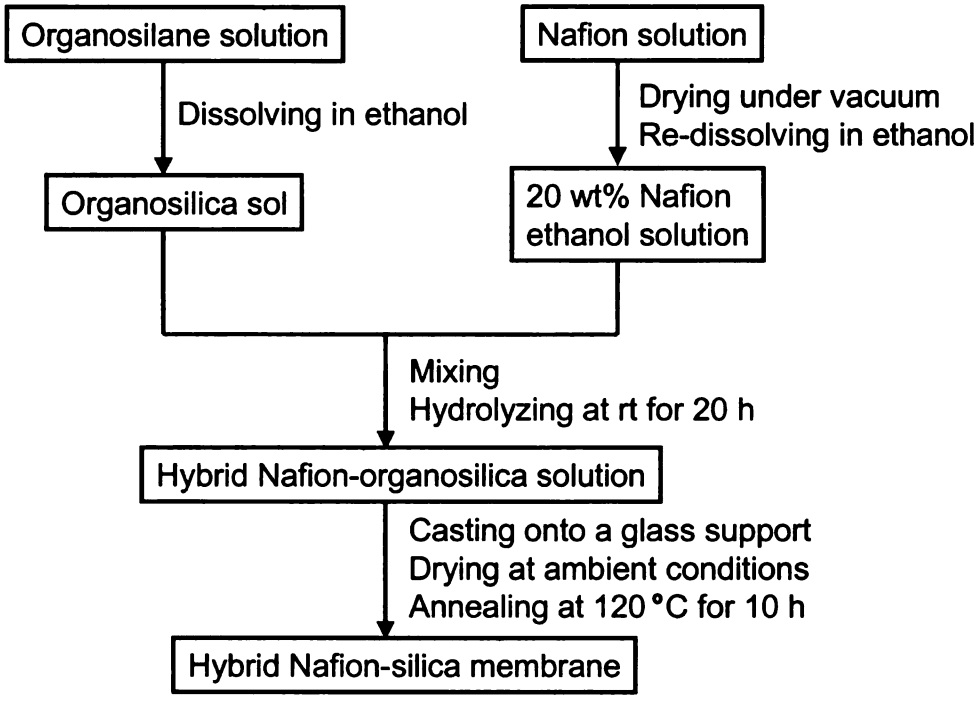

Figure 5. Preparation procedure of Nafion-silica hybrid membranes.[19]

Metal oxide nanoparticles

TiO_2 has a high surface zeta potential and proton-induced charge density over an extended temperature range (25-200 °C) and efficiently binds water molecules through hydrogen bonding.[26,27] The electrochemical performance of Nafion-TiO_2 composite membranes was investigated in a high temperature H_2/O_2 fuel cell. The composite membrane had a two-layer structure and the TiO_2 powder was mainly deposited on one side of the membrane. The performance of a composite membrane with 20 wt% TiO_2 content, tested at 50 % RH, was comparable to a conventional Nafion membrane at 100 % RH. The improved water retention of the composite membrane suggests the possibility of fabricating composite PEMs for operation at 120 °C and 50 % RH conditions without loss of

performance. Due to their excellent properties, a wide variety of metal oxides have been exploited as additives to improve Nafion's performance.[28,29]

Metal nanoparticles

Metal nanoparticles can enhance Nafion's performance in fuel cells. Positively charged Pd nanoparticles were produced by the alcohol-based reduction of metallic ions with poly(diallyldimethylammonium chloride) (PDDA) as the surfactant.[30] Using the electrostatic interactions between the positively charged Pd nanoparticles and the negatively charged sulfonic acid groups of Nafion ionomers, multi-layers of Pd nanoparticles and Nafion ionomers were self-assembled onto Nafion membranes, generating an effective methanol-blocking proton exchange membrane (**Figure 6**). Self-assembly of 3 double-layers of Pd nanoparticles and Nafion ionomers provided a composite membrane with 99 % less methanol crossover and a slight decrease in proton conductivity compared to the original Nafion membrane.

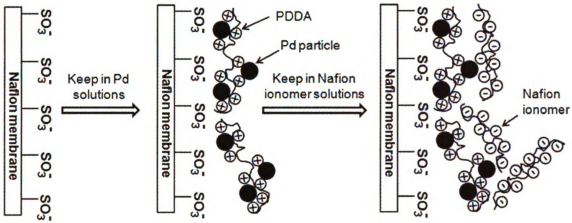

Figure 6. Schematic illustration of multi-layer self-assembly of Pd nanoparticles and Nafion ionomers onto Nafion membranes.[30]

Au nanoparticles can also improve Nafion's performance in direct methanol fuel cells. The self-assembly of ~4 nm charged Au nanoparticles onto Nafion 212 membrane surfaces formed a monolayer structure and drastically reduced the methanol crossover from 168 to 18 mA/cm^2 under the conditions of 2 mol/L methanol and 60 °C.[31] The self-assembly of Pt and other metal nanoparticles onto the surface of Nafion also has been reported,[32] however, these methods usually increase cell resistance and reduce proton conductivity.

Self-humidifying materials

The poor proton conductivity of Nafion at elevated temperatures is attributed to vaporization of water leading to the lack of proton transport vehicles. A class of inorganic-organic composite membranes, "self-humidifying" proton exchange membranes, was developed by Uchida *et al.* to improve the high temperature performance of Nafion.[33,34] Generally, "self-humidifying" membranes contain highly dispersed Pt nanoparticles, which catalyze recombination of

diffused H_2 and O_2 inside the membranes, generating water molecules that "wet" the membranes. A hygroscopic metal oxide is included to adsorb the water produced at the Pt particles and at the cathode. The resulting composite membranes exhibited lower gas and methanol crossover as well as improved water uptake compared to Nafion membranes. In addition, the ohmic resistance of membranes decreased when operated with dry H_2 and O_2 at 80 °C and ambient pressure.

Recently, Gao and coworkers developed a self-humidifying membrane from an exfoliated Pt-clay/Nafion nanocomposite.[35] Instead of using spherical hygroscopic particles, which may have poor compatibility with the membrane material and reduce membrane toughness, they used clay platelets to balance the water content and enhance the mechanical properties of the composite membrane. Monolayers of Pt nanoparticles (2-3 nm) were chemically anchored to the exfoliated clay surfaces through chemical vapor deposition to stabilize Pt nanoparticles (**Figure 7**). The composite membranes were prepared by simple recasting a Nafion solution and Pt-clay. With dry H_2 and O_2, the power density of the Pt-clay/Nafion composite membrane was 170 % higher than commercial Nafion 112 of a similar thickness tested under the same conditions.

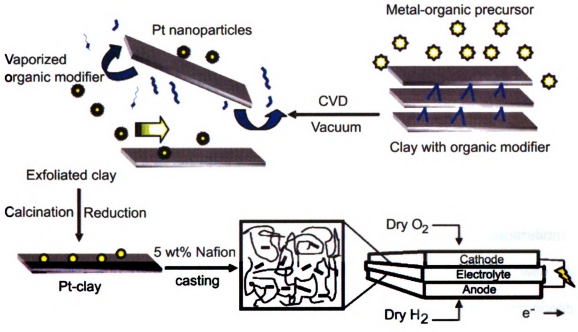

Figure 7. Schematic diagram of preparing exfoliated Pt-clay/Nafion composite membrane. (Reprinted with permission from *Langmuir* **2008**, *24*, 2663-2670. Copyright 2008 American Chemical Society)

Incorporation of inorganic materials in Nafion is a feasible and effective method for improving membrane stability as well as reducing water swelling and methanol crossover. However, improving these properties usually comes at the cost of decreased proton conductivity. More importantly, the cost of Nafion remains a barrier to wider application of Nafion-containing composite membranes. Nafion's cost and its poor performance at high temperature has stimulated research into alternatives to Nafion.

The most widely studied alternatives to Nafion are hydrocarbon polyelectrolytes, such as sulfonated polystyrene,[15,36-57] sulfonated polyimides,[58-84] sulfonated poly(ether ether ketone)s,[14,85-121] and sulfonated polysulfone.[122-142] The proton conductivity of PEMs is a function of both the chemical structure of the polymeric materials and the membrane morphology. Therefore, most

research is aimed at generating inexpensive, chemically and mechanically stable proton conducting membranes from existing polymer materials instead of synthesizing new polyelectrolytes.

Block copolymers as an approach to alternatives to Nafion membranes

Nafion's proton conducting mechanism suggests that developing ionic channels inside membranes by microphase or nanophase separation of hydrophilic and hydrophobic segments would be the key to PEMs with high proton conductivity. Designing well-defined block copolymers with incompatible blocks is a useful approach to achieve microphase-separated structures, such as cylinders, lamellar, and spheres.[143] Extensive research effort has been devoted to PEMs fabricated from block copolymer systems, which have proton conducting hydrophilic blocks and mechanically stable hydrophobic blocks. These materials provide an insight into the relationship between polymer structure, morphology and proton conductivity.[82,128,134,144-156] In block copolymer-based PEMs, phase-separated morphologies are common; the ionic phase is composed of hydrophilic segments that support proton conductivity while the insulating hydrophobic phase affords dimensional stability.

Sulfonated block co-polyimides PEM

Polyimides are often described as high-performance materials due to their excellent thermal, chemical, and mechanical stability, good film-forming ability, and low gas permeability. Sulfonated block co-polyimides are widely studied as

alternatives to Nafion membranes.[1,82,83,114,149,157,158] Usually, the synthesis of sulfonated block co-polyimides involves a two-pot procedure as shown in **Scheme 1**.[83] Fluorinated block co-polyimides were synthesized with different block lengths and diamine compositions, and were found to have proton conductivities that depended on the block lengths. The conductivities of sulfonated block copolymers increased with the block length, which was explained as the influence of block lengths on the distribution of ionic channels. Furthermore, the conductivities of sulfonated block co-polyimides were higher than the corresponding random copolymer membranes, which was ascribed to ionic channels formed by phase separation of hydrophilic and hydrophobic sequences in block co-polyimides.

Scheme 1. Synthesis of sulfonated block co-polyimides.[83]

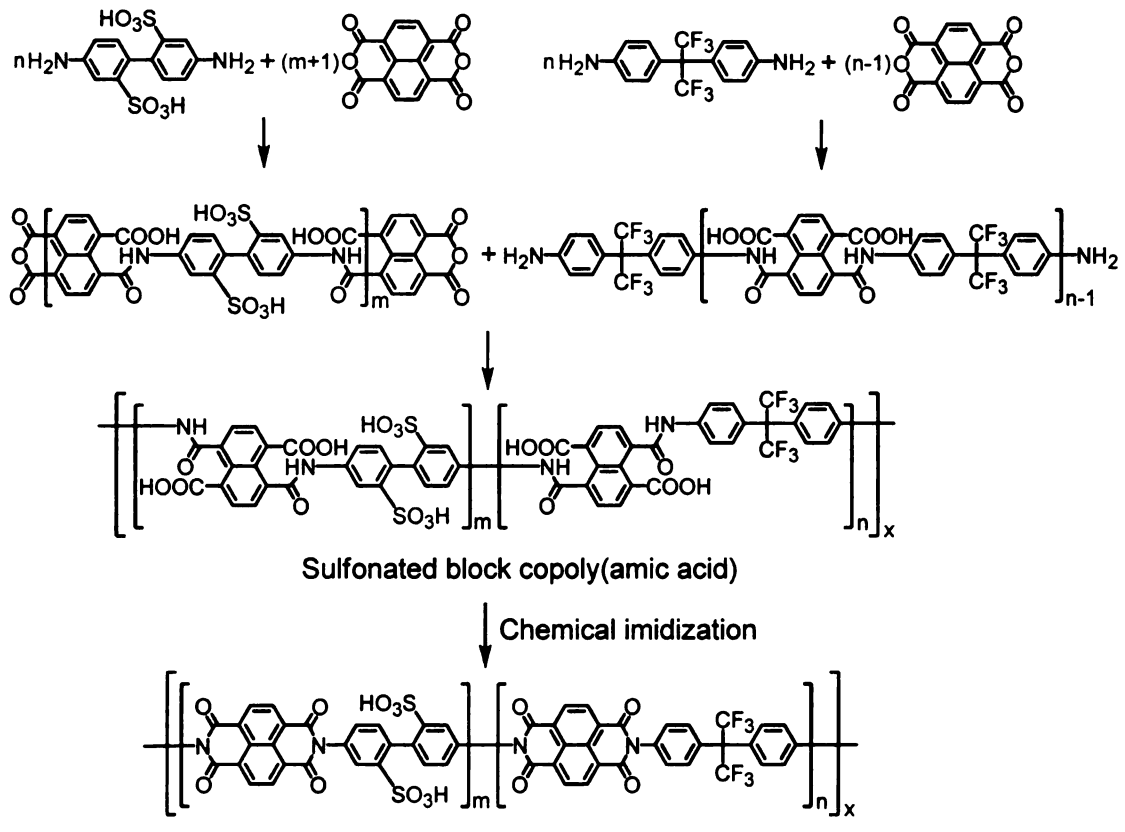

Sulfonated block co-poly(arylene ether sulfone) PEM

Another extensively explored block copolymer system is sulfonated block co-poly(arylene ether sulfone)s. These polymers are one of the most promising low-cost alternatives to Nafion membranes. Like polyimides, poly(arylene ether sulfone)s have excellent thermal, chemical, and mechanical stability, superior hydrolytic stability, and good processability. PEMs solvent-cast from hydrophilic-hydrophobic poly(arylene ether sulfone) block copolymers (**Scheme 2**) showed increases in proton conductivity and water uptake as the block length is increased.[152,156] Using shorter blocks resulted in reduced water uptake, and

lower proton and water transport, comparable to random copolymers. However, membranes produced with long block lengths exhibited higher proton conductivities than random copolymers with similar ion exchange capacity (IEC) values under partially hydrated conditions, which was ascribed to the unique microstructure and phase-separated morphology of hydrophilic-hydrophobic block copolymers. Water analysis supported different microstructures and morphologies for the block copolymer and random copolymer: phase-separated morphologies in block copolymers but closed and isolated morphological structures in random copolymers, despite having similar chemical structures and chemical compositions. This implies that proton transport is controlled by not only the acidity, but also the morphology of the membrane system.

Scheme 2. Synthesis of segmented sulfonated multiblock co-poly(arylene ether sulfone) with different linkage composition.[156]

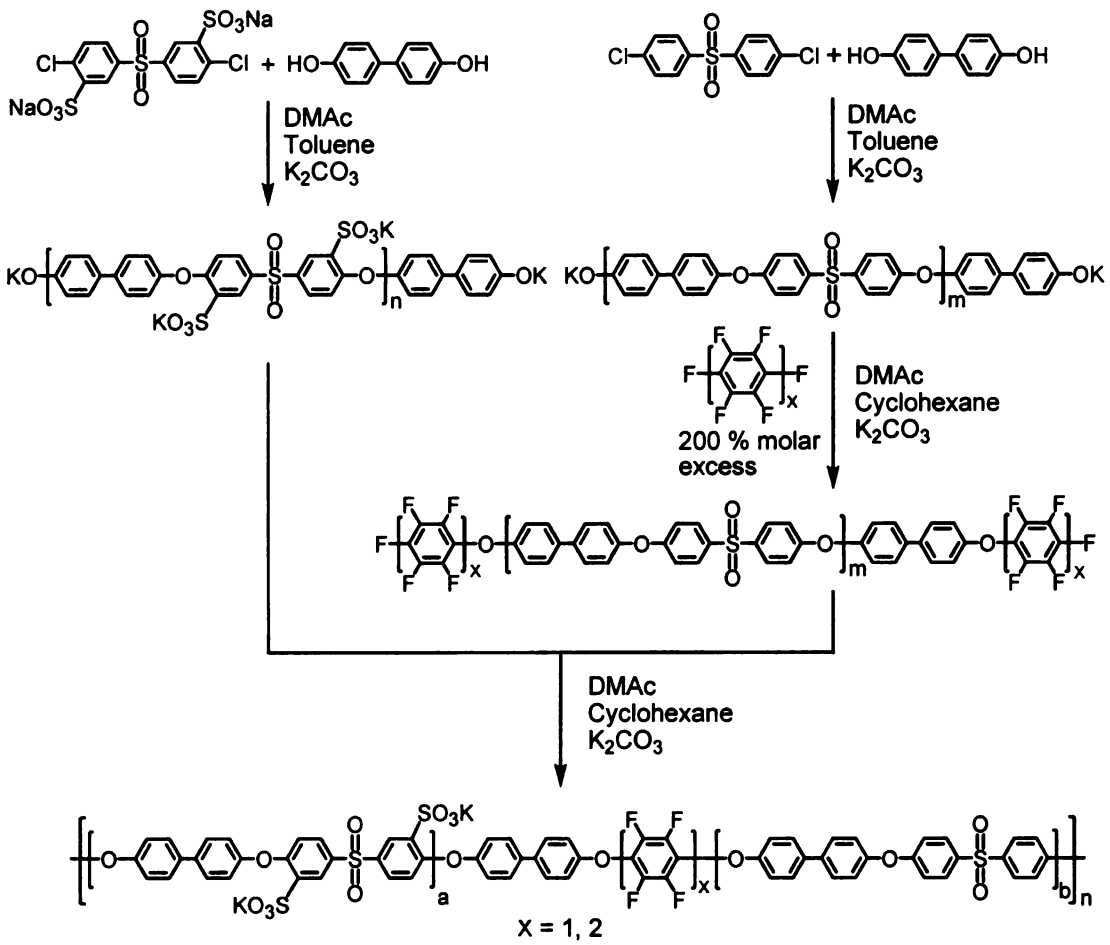

Sulfonated poly(arylene ether sulfone)-*b*-polyimide PEM

In addition to block co-polyimides or block co-poly(arylene ether sulfone)s, PEMs were also fabricated from more complicated block copolymer architectures. As shown in **Figure 8,** PEMs based on a bisulfonated poly(arylene ether sulfone)-*b*-polyimide (BPSH-*b*-PI) copolymer exhibit well-defined hydrophilic and hydrophobic domains, and the block copolymer morphologies correlate to the block lengths (**Figure 9**).[149] Tapping mode AFM phase images show that the

dark ionic regime and the bright nonionic regime increased when the block lengths increased, and eventually forming a long-range bicontinuous lamellar microstructure. In addition to the well-defined phase-separated morphology, the hydrolytic stability of the block copolymer in 80 °C water was greater than random polyimide copolymers.

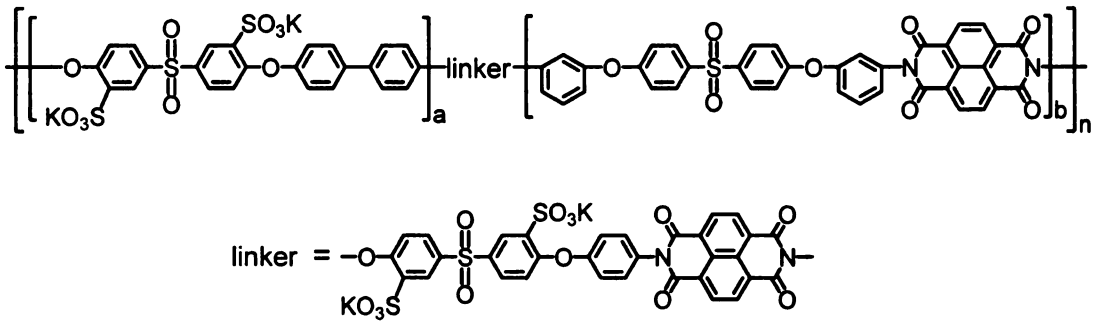

Figure 8. Structure of segmented bisulfonated poly(arylene ether sulfone)-*b*-polyimide (BPSH-*b*-PI) copolymer.

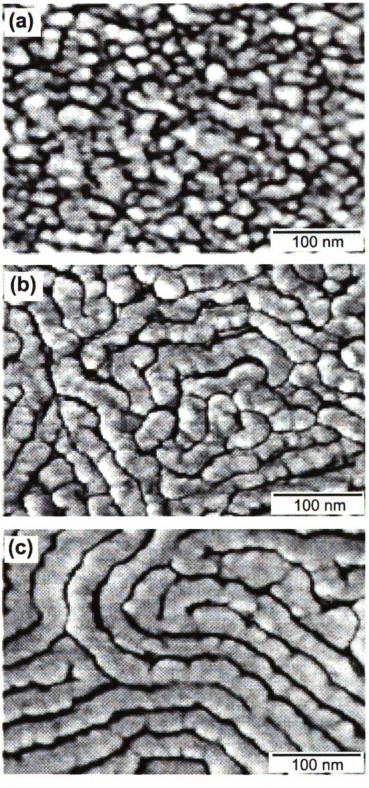

Figure 9. Tapping mode AFM phase images of BPSH-*b*-PI copolymers with different block lengths. (both block lengths increase from top to bottom) (Reprinted with permission from *J. Polym. Sci. Pol. Chem.* **2007**, *45*, 4879-4890. Copyright 2007 Wiley InterScience)

Sulfonated polysulfone-*b*-poly(vinylidene fluoride) PEM

Poly(vinylidene fluoride) (PVDF) is chemically and mechanically stable and is commonly used as the hydrophobic component of block copolymer-based PEMs. For example, Holdcroft *et al.* synthesized sulfonated polysulfone-*b*-poly(vinylidene fluoride) (PSf-*b*-PVDF) copolymers from the polycondensation of an α,ω-dihydroxybisphenol A and α,ω-dibromo poly(vinylidene fluoride) as illustrated in **Scheme 3**.[123] After sulfonation, the copolymers were cast into PEMs to test their performance. Despite their relatively low ion exchange capacity, the sulfonated PSf-*b*-PVDF copolymers exhibited higher proton conductivities than sulfonated polysulfones, which was attributed to greater phase separation in the block copolymer system, as has been proposed for other block copolymer systems.

Scheme 3. Synthesis of Bisphenol A PSf-*b*-PVDF copolymers.[123]

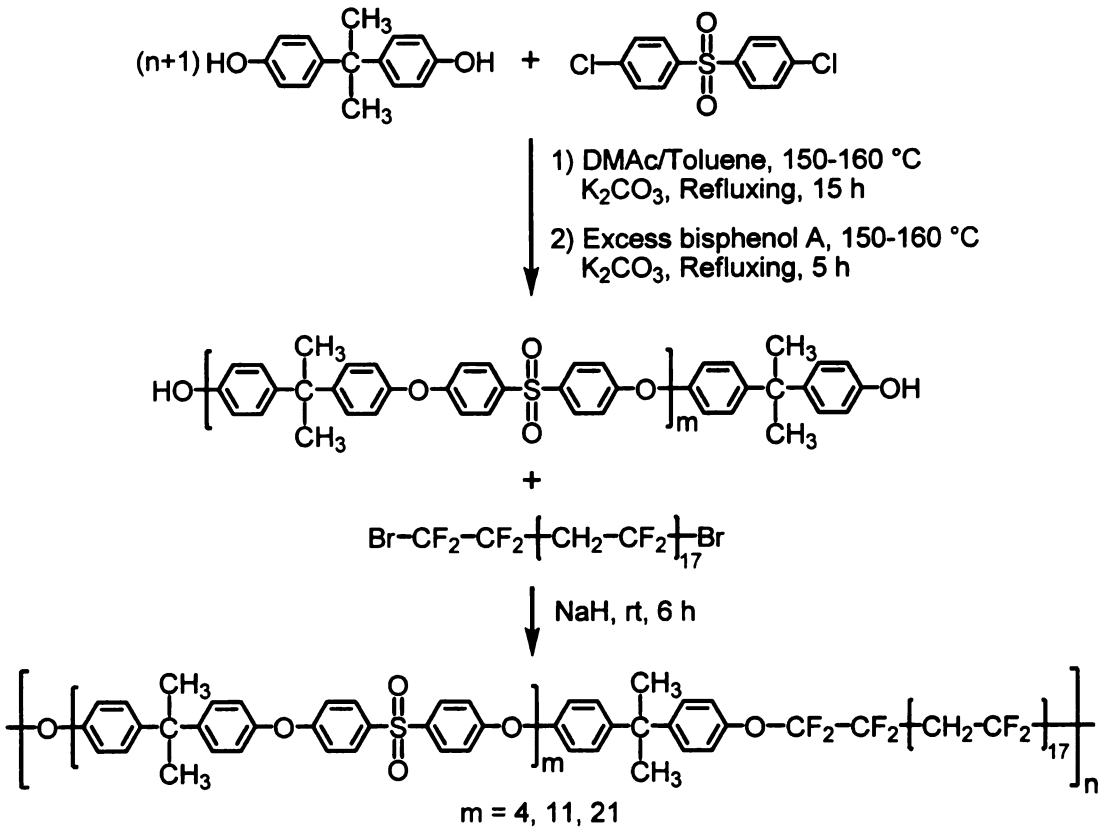

Sulfonated poly(styrenesulfonate)-*b*-poly(methylbutylene) PEM

In addition to high performance polyelectrolyte systems, similar phase-separated structures have been developed in block copolymer systems containing polystyrene. For example, PEMs obtained from poly(styrenesulfonate)-*block*-poly(methylbutylene) (PSS-*b*-PMB) copolymers spontaneously formed hydrophilic PSS and hydrophobic PMB domains, which resulted in microphase separation.[159] The water uptake of the PEMs, which had a hydrophilic domain width ranging from 2 to 5 nm, increased as the surrounding air temperature increased from room temperature to 90 °C at a constant relative

humidity, whereas Nafion 117 became drier under the same conditions. Consistently, the proton conductivity of these PEMs increased with increasing temperatures. This unexpected behavior might be due to capillary condensation, which suppressed solvent evaporation at elevated temperatures. This interesting discovery might enable high temperature PEM fuel cells.

Block copolymers also show better performance at low hydration levels compared to homopolymers and random copolymers, which results from ionic channels formed upon microphase separation of the hydrophilic and the hydrophobic blocks. However, obtaining high proton conductivity and mechanical stability in block copolymers usually correlates with difficulty in optimizing the physiochemical properties of individual blocks and increased membrane synthesis and production costs. In addition, some block copolymers suffer from severe swelling and poor mechanical strength problems.[160]

Polymer blends as an approach to alternatives to Nafion membranes

Polymer blending is a useful route to Nafion alternative membranes. Instead of integrating the hydrophilic segment (proton conductivity) and the hydrophobic component (mechanical strength) in a single polymer structure, blending a polyelectrolyte with a non-conductive hydrophobic material has become a popular route to PEMs.[60,61,101,119,161-170] Blending is usually based on commercially available and inexpensive polymer precursors and thus it is a simple and cost-effective route to PEMs. Compared to block copolymer-based PEMs, the blending concept eliminates the need to optimize the mechanical,

chemical and physical properties in a single polymer chain and it has the potential to develop a wide variety of PEMs. A range of membrane properties, such as proton conductivity, water uptake, and mechanical strength, can be easily tailored by (1) adjusting the relative ratio of two blending materials, (2) varying the ion exchange capacity of the hydrophilic component, or (3) modifying the backbones of the blend components.

Polymer blends have been extensively studied and have had some success as Nafion alternative membranes. In order to form stable membranes, research attention needs to be directed to the different kinds of interactions between the blending materials, as shown in **Figure 10.**[170]

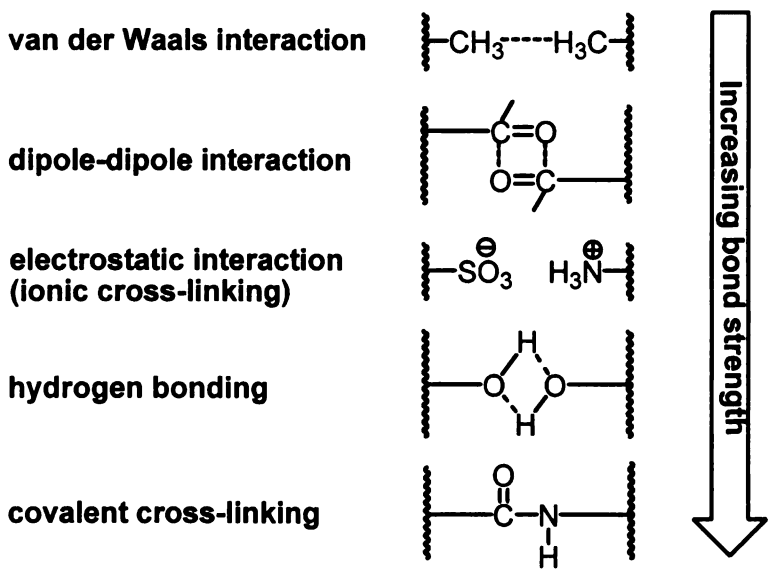

Figure 10. Specific interactions between blending materials.[170]

Van der Waals/dipole-dipole interaction

PVDF has been widely studied as the hydrophobic material in blend membranes.[49,108,171-173] The large dipole moment associated with the CF_2 moiety favors mixing with polar polymers such as poly(methyl methacrylate) (PMMA). A clever blending example is the mixing of sulfonated poly(styrene-*b*-methyl methacrylate) (PSSA-*b*-PMMA) and PVDF; PMMA is miscible with PVDF but PSSA is immiscible. Since the blend membranes were stained with RuO_4, the dark regimes represent the hydrophilic component (PSSA) while the brighter areas correspond to the hydrophobic PMMA and PVDF (**Figure 11**).[49] The membrane proton conductivity increased with the degree of sulfonation in PSSA-*b*-PMMA and also was enhanced by a well-ordered phase-separated morphology. The membranes in **Figure 11a** and **Figure 11b** had the same degree of sulfonation but the membrane shown in **Figure 11a** had smaller domains due to a lower PVDF content. Not surprisingly, it also had a higher proton conductivity. Interestingly, a comparison between the two membranes in **Figure 11a** and **Figure 11c**, which had the same PVDF content but different sulfonation levels, shows that the hydrophilic domain increased as the sulfonation level increased due to the aggregation of more sulfonic acid groups. The membrane in **Figure 11c** formed the best-ordered phase-separated microstructure and exhibited the highest proton conductivity. The morphological structure of the blend membrane was easily controlled by varying the blend ratio of the two blending materials.

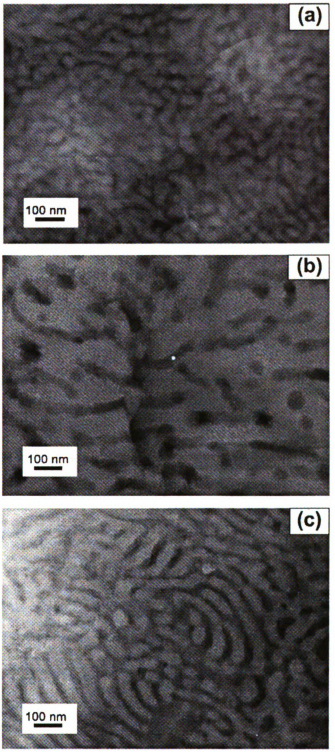

Figure 11. TEM images of blend membranes with different degrees of sulfonation and blend ratios: **(a)** S24F22; **(b)** S24F41; and **(c)** S39F22. (SxxFyy, where xx represents the sulfonation level and yy stands for the content of PVDF in the blend membrane) (Reprinted with permission from *J. Power Sources* **2009**, *188*, 127-131. Copyright 2009 Elsevier)

Hydrogen bonding interaction

Blend membranes from sulfonated poly(ether ketone ketone) (SPEKK), the proton-conducting component, and poly(ether sulfone) (PES) resolved the swelling problem of SPEKK to some extent despite the immiscibility of SPEKK with PES.[169] Blending PES with the highly sulfonated SPEKK provided robust membranes. In this example, the membrane morphology can be controlled by balancing the polymer composition, mixing ratios, solution casting solvent and temperature. At certain sulfonation levels of SPEKK, the blend membrane phase separated into co-continuous morphologies. Similar improved properties were seen in blends of sulfonated polyimide (SPI) and PES.[60] The addition of PES reduced the excessive swelling of SPI membranes and greatly increased both the stability and tensile strength of the SPIs membrane.

Hong and coworkers proposed a convenient way to fabricate PEMs from blends of polystyrene (PS), poly(ethylene oxide) (PEO), and a fine powder of poly(styrene sulfonic acid) (PSSA) powder.[174] In the blend membrane, PSSA acted as a proton source and as a compatibilizer, a polymer that improves the miscibility between the two polymers, in this case, hydrophilic PEO and hydrophobic PS (**Figure 12a**). PS provided the mechanical strength of the blend membrane while PEO conveyed protons to the cathode under an electric field as illustrated in **Figure 12b**. When the PEO and PS mix well, the hydrophobic PS component limits water evaporation at elevated temperatures which may be relevant to designs of PEMs for application at elevated temperatures.

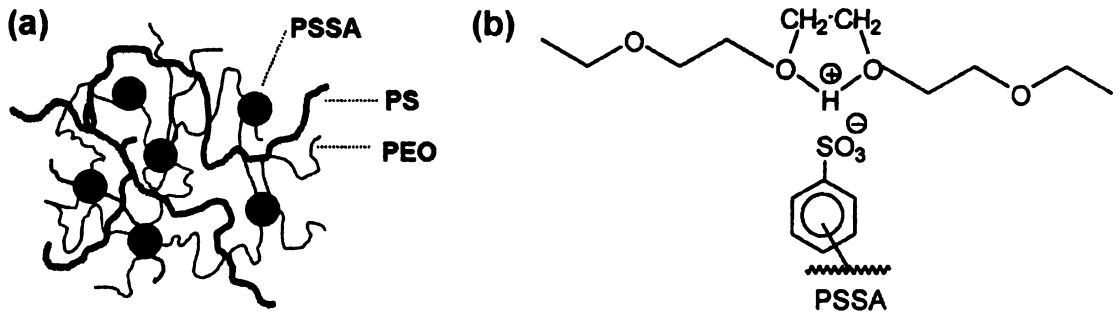

Figure 12. (a) Schematic view of the polymer blend. **(b)** A schematic diagram of the formation of a H-bonding complex between the sulfonic acid group and PEO units.[174]

Electrostatic interaction (ionic cross-linking)

Ionic cross-linking in blend membranes utilizes acid-base interactions such as those between sulfonic acid groups and the nitrogen atoms of imidazole groups. These materials have been explored in direct methanol fuel cells.[85,110,119,175] Blending sulfonated poly(ether ether ketone) (SPEEK) with polysulfone-4-nitrobenzimidazole (PSf-NBIm, **Figure 13**) formed membranes with lower methanol crossover than SPEEK and Nafion 115 membranes in direct methanol fuel cells.[85] The size of the ionic clusters formed from the sulfonic acid groups of SPEEK increased in the blend membrane, owing to the addition of the polar nitrobenzimidazole side groups to ionic clusters. These membranes had reduced uptake of water and methanol/water solutions. Membranes with 2.5 and 5.0 wt% PSf-NBIm contents had higher proton conductivities than SPEEK, and the imidazole groups were thought to facilitate proton conduction from one sulfonate to another (**Figure 14**). Imidazoles can act as a proton conducting solvent and replace the acid/water complex in conventional PEMs, making high proton conductivity under anhydrous conditions possible.

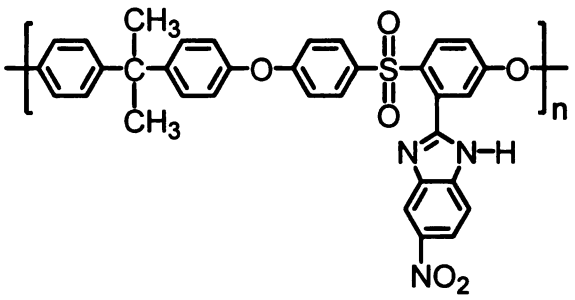

Figure 13. Structure of polysulfone bearing 4-nitrobenzimidazole side groups.[85]

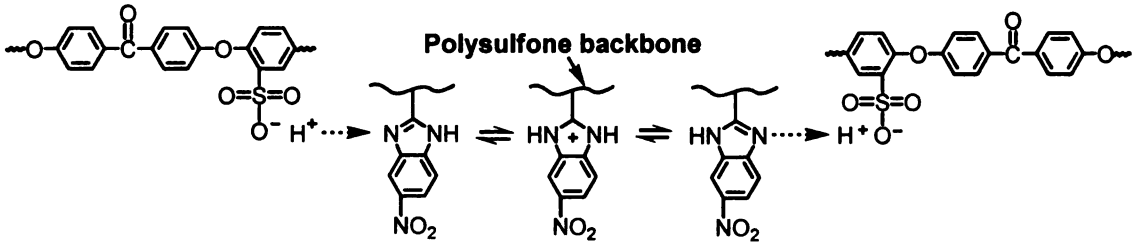

Figure 14. Schematic view of the proton transfer mechanism with electrostatic interaction between SPEEK/PSf-NBIm blending materials.[85]

Covalent cross-linking

One disadvantage of ionically cross-linked blend membranes from PSf and polybases is that the electrostatic interaction breaks down in aqueous environment at elevated temperatures (T>70-90 °C), leading to brittle membranes.[170] Cross-linking via covalent bonds is more robust and has played an important role in improving membrane performance.[116,176,177] For example, the thermally activated condensation of SPEEK and polyols bridges neighboring chains (**Figure 15**). Cross-linking improved the stability and mechanical strength of SPEEK membranes and suppressed excessive water uptake. Though cross-linking reduced the number of available sulfonic acid groups for proton

conduction, the blend membrane showed only a slight reduction in proton conductivity compared to a pure SPEEK membrane.

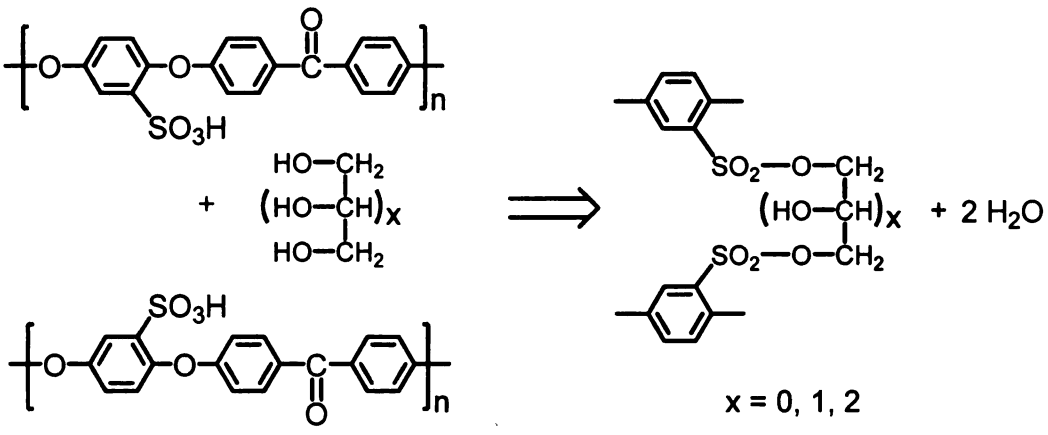

Figure 15. Illustration of possible SPEEK cross-linking reaction.[177]

Both polymer blends and block copolymers have had some success as alternatives to Nafion membranes. In block copolymers, the hydrophilic and hydrophobic components are part of a single polymer structure, which lessens concerns of miscibility and the interactions of different chemical blocks. Blend membranes distribute the functions of proton transport and mechanical stability into different materials, which cannot be realized in homopolymer based membranes. Despite significant improvement in fuel cell membrane performance, controlling membrane microstructure has been mostly overlooked. It is known that the phase-separated morphology of Nafion is critical for its success as a fuel cell membrane, and controlling the microstructure in alternative membranes is desirable. For example, with no control over the alignment of proton conductive

polymers, blend membranes are generally associated with improved mechanical properties but with a sacrifice of proton conductivity.

Controlling the ionic channels of PEMs

Recently, Gao *et al.* utilized self-assembly of surface-charged latex particles to form ionic channels for proton conduction.[178] In their work, the latex particles were synthesized by aqueous emulsion polymerization of two hydrophobic monomers, butyl acrylate and methyl methacrylate, a cross-linker, *N,N'*-methylene-bis-(acrylamide), and a charged monomer, sodium styrene sulfonate, resulting in particles with charged surfaces. Membranes were developed by solvent casting an aqueous dispersion of cross-linked particles, followed by acidification, which provided particles with hydrophobic cores and proton-conducting surfaces. Continuous ionic channels naturally developed upon annealing, resulting in no or a very low percolation threshold (**Figure 16**). In these membranes, the charged particles were not physically packed as in amorphous membranes, but instead they adhered to each other by either intersphere cross-linking and/or entangling chains. Therefore, the resulting membranes had significantly higher proton conductivities than amorphous membranes with the same charge content. However, the membranes swelled excessively reducing their mechanical stability. A better approach is needed to solve the swelling problem while minimizing the percolation threshold.

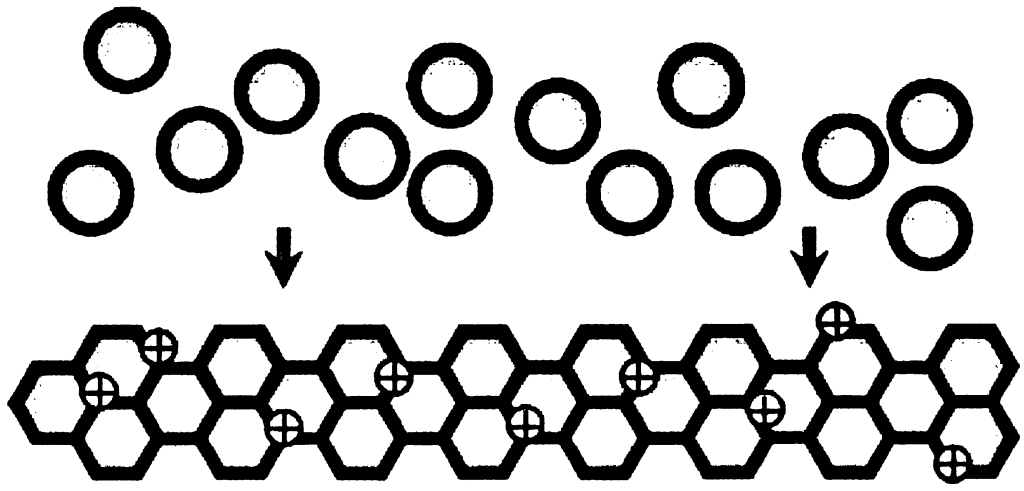

Figure 16. Schematic illustration of precursor particles with hydrophobic cores (grey) and ionic surface (dark) and a film fabricated by self-assembly of the particles. (Reprinted with permission from *Macromolecules* **2005**, *38*, 5854-5856. Copyright 2005 American Chemical Society)

Electric field aligned blend membranes

Gao's model suggests that aligning proton conductive particles in a suitable hydrophobic matrix might lower the percolation threshold and solve the swelling problem. Particle alignment can be accomplished by applying an external driving force while curing membranes, such as an electric or magnetic field. Oren *et al.* first utilized this principle to align ion exchange particles in a two-component RTV silicon rubber matrix by the application of an AC electric field during the fabrication of ion-exchange membranes.[179] As shown in **Figure 17a**, particles dispersed randomly in the absence of an electrical field. With the application of the electric field, long chain-like aggregates aligned along the field (**Figure 17b**). The alignment shifted the percolation threshold for ionic conduction, from 40 % particle content for membranes with randomly distributed particles to 10 % for membranes with ordered particles. For a given ionic conductivity,

membranes with aligned particles required fewer particles than conventional membranes with randomly dispersed particles. The benefits of a low particle content include reduced water uptake and increased mechanical stability.

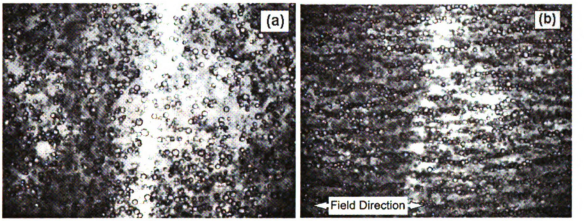

Figure 17. Light microscopy photographs of **(a)** non-ordered; and **(b)** ordered ion-exchange particles in the polymeric component of the rubber. 100X, electric field: 1330V/cm, 50 Hz. (Reprinted with permission from *J. Membr. Sci.* **2004**, *239*, 17-26. Copyright 2004 Elsevier)

Oren *et al.* successfully reduced the percolation threshold, but the conductivity mechanisms for ions and protons may be different. Shaw *et al.* extended Oren's work to proton conductivity, and investigated the effects of the electric field amplitude and frequency on the alignment of sulfonated crosslinked polystyrene ion exchange resin (acid form) in a poly(dimethylsiloxane) matrix perpendicularly to the membrane plane.[180] As illustrated in **Figure 18**, a membrane with 5 wt % particles showed no alignment in AC fields <150 V/mm at 5 Hz; alignment only occurred when the electric field exceeded a certain threshold. Membranes with aligned particles had higher proton conductivities and less water uptake than membranes with unaligned particles.

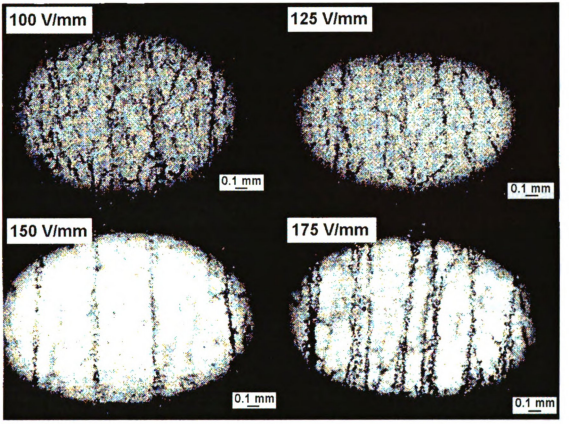

Figure 18. Optical micrographs of the alignment of sulfonated crosslinked polystyrene ion exchange resin in a poly(dimethylsiloxane) matrix under AC electric field of different magnitudes at 5 Hz frequency. (Reprinted with permission from *ANTEC* **2005**, 1731-1735. Copyright 2005 Society of Plastics Engineers)

Later, the same group extended the electric field alignment of polyelectrolytes to a blend of SPEKK and a poly(ether imide) (PEI), which resulted in a thousand-fold increase in conductivity at low humidity due to the formation of aligned proton conducting channels in SPEKK.[101]

Magnetic field aligned blend membranes

Although the application of electric fields has successfully aligned polyelectrolytes while casting blend membranes, there are limitations to this

technique. There must be sufficient dielectric contrast between polyelectrolyte and the matrix, and the matrix must sustain a high field and have sufficient mobility. These restrictions have hindered the broad application of this processing technique due to a limited choice of matrix materials. An alternative technique, using magnetic fields as the external driving force, is more suitable for polyelectrolyte alignment in blend membranes, as most polymers are anti-ferromagetic and hence are good matrix materials. Unlike electric fields, magnetic fields are not restricted in terms of the applied field strength, but only require that the polyelectrolytes have sufficient magnetization to respond to a magnetic field.

Recently, the Shaw group synthesized proton conducting magnetic nanoparticles via the emulsion polymerization of styrene, divinylbenzene, and sodium 4-styrenesulfonate (NaSS) in the presence of a γ-Fe_2O_3 dispersion. Subsequent acidification provided the sulfonic acid, as demonstrated in **Figure 19**.[181] During the membrane casting process, an external magnetic field was used to align proton conductive magnetic nanoparticles in SPEKK. Successful alignment of the magnetic nanoparticles can be seen in **Figure 20b,** while processing the membrane without a magnetic field resulted in randomly dispersed particles, as illustrated in **Figure 20a**. Not surprisingly, the conductivity of membranes with aligned particles was twice that of unaligned controls. However, the proton conductivity of the blend membrane was much lower than a standard SPEKK membrane, which was ascribed to the decreased IEC of the blend membrane.

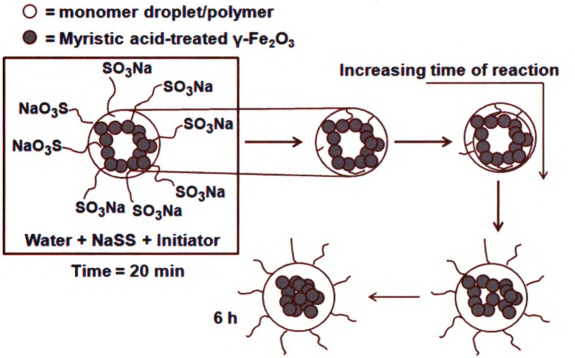

Figure 19. Schematic diagram of the proposed mechanism for the formation of magnetic particles.[181]

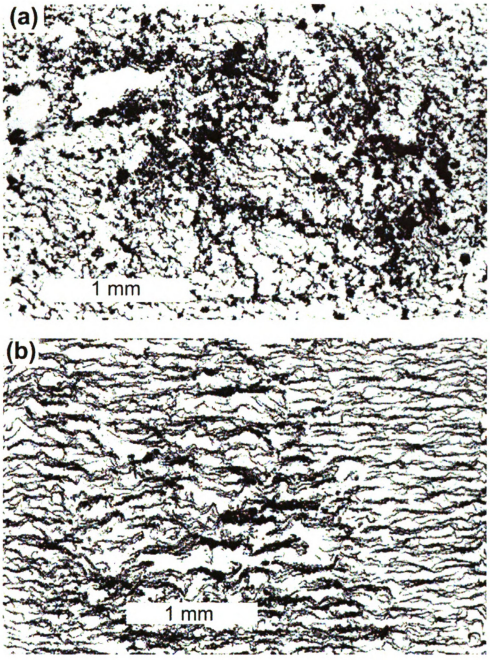

Figure 20. Images of SPEEK membranes with magnetic nanoparticles **(a)** randomly dispersed; and **(b)** aligned in magnetic field. (Reprinted with permission from *J. Membr. Sci.* **2007**, *303*, 64-71. Copyright 2007 Elsevier)

While Shaw *et al.* showed that magnetic fields can be used to align magnetic nanoparticles in a SPEEK matrix, there are limitations to Shaw's approach. The γ-Fe_2O_3 particles were confined to the surfaces of composite

particles instead of being encapsulated by the polymer, making γ-Fe_2O_3 particles vulnerable to the strong acidic environment of PEMs (γ-Fe_2O_3 particles dissociate in acid). Secondly, the magnetic particles were aligned in the plane of the membrane, while real PEMs require through-plane proton conducting paths. Finally, both the magnetic particles and the matrix (SPEEK) are hydrophilic, which would likely result in excessive swelling and low mechanical strength membranes. Nevertheless, using magnetic fields to align conductive paths may be a useful technique for improving blend membrane performance.

Chapter 2 Direct Polymerization of Sodium 4-Styrenesulfonate from Silica Nanoparticle Surface: Kinetics, Characterization, and Application in Fuel Cells

Introduction

Ionic transport in polymers primarily depends on the number of charge carriers and their mobility. Practical polymer electrolytes are required to provide high ionic conductivity and chemical and thermal stability, while maintaining sufficient mechanical properties to serve as an electrode separator. In the case of lithium ion systems, conductivity is correlated with the segmental mobility of the polymer host, and therefore polymers with low glass transition temperatures (T_g) are ideal hosts for electrolytes.[182,183] However, low T_g materials have poor mechanical properties and must be used in conjunction with an external electrode separator. Similar challenges are encountered with membranes for fuel cell applications. For example, highly sulfonated polymers have good proton conductivities, but tend to swell excessively.[2]

One solution to the challenge of synthesizing polymers that simultaneously have high conductivity and good mechanical properties is to design electrolytes from polymers that spontaneously separate into ion-conducting and hydrophobic phases. To ensure high conductivity, the phases need to be bicontinuous while maintaining good mechanical properties. There are many variants of this approach, including block copolymers,[151,184] polymer blends,[108] and various nanoparticles dispersed in polymer hosts.[25,31]

The phase-separated polymers approach is particularly useful in the design of proton exchange membranes (PEMs) for fuel cells. Structural studies of hydrated Nafion, the prototype PEM, show a continuous network of proton conducting channels stabilized by the perfluorocarbon backbone of the polymer.[4,11] Recent alternative membranes, designed to overcome Nafion's limited temperature range (<90 °C), mimic the Nafion structure by incorporating both hydrophobic segments and highly sulfonated blocks to effect phase separation on the nano-scale.[134,148,185]

A simpler approach to bicontinuous electrolytes is to blend a polyelectrolyte material with a hydrophobic non-conductive material.[60,61,101,119,161-169] The blending concept eliminates the need to optimize the proton transport and physical properties in a single polymer chain. Blending is usually based on commercially available and inexpensive precursor polymers, and therefore blending can be a simple and cost-effective route to PEMs. A popular hydrophobic material in blend membranes is poly(vinylidene fluoride) (PVDF), which is easy to process into membranes, commercially available, and chemically and mechanically stable.[49,108,171-173] A widely studied polyelectrolyte material for PEMs is poly(4-styrenesulfonic acid) (PSSH) because of its high sulfonation level, low cost, and the simplicity of synthesis.[36-41]

Blends also have limitations. They must be available with a stable bicontinuous morphology, and the polymers that comprise the conductive phase cannot leach from the PEM. Leaching can be inhibited by binding polymers to nanoparticles, in effect, increasing their polymer molecular weight and reducing

their mobility. Core-shell particles coated with proton-conducting polyelectrolytes can take advantage of both the inorganic and organic functional groups[186,187] and are good candidates for the hydrophilic component in blend membranes.

There are many methods that generate polymer shells from inorganic nanoparticle cores, such as the "grafting from"[188,189] and "grafting to"[190,191] techniques, and electrostatic self-assembly.[192] Among these, atom transfer radical polymerization (ATRP) has been the primary methodology for growing polymers of precise molar mass, architecture, and functionality from inorganic nanoparticles.[186,188,193-200] ATRP has been applied to a rich variety of monomers to prepare polyelectrolyte end chain-immobilized nanoparticles.

In this report, we test the utility of blends comprised of functionalized nanoparticles in a hydrophobic matrix (PVDF). Silica particles were modified with a thick layer of PSSH via ATRP. These particles can be synthesized by two methods: grow polystyrene from silica particles and then sulfonate the polystyrene, or directly polymerize sodium 4-styrenesulfonate onto silica particles[199] followed by acidification. The "post-sulfonation" approach usually results in low degrees of sulfonation, cross-linking, and polymer chain degradation,[2] while direct polymerization of sodium 4-styrenesulfonate places one sulfonic acid on each monomer, occurs at ambient temperature, and has no significant side reactions.[199]

Herein, we report the synthesis and characterization of hybrid nanoparticles (silica-PSSNa) comprised of ~7 nm diameter silica cores and a poly(sodium 4-styrenesulfonate) (PSSNa) shell. After acidification, the hybrid

nanoparticles were blended with PVDF, and composite membranes were prepared using a solution-casting method. The as-synthesized membranes had proton conductivities comparable to, or higher than Nafion 117 membranes. Compared to conventional PSSH blend membranes, the advantage of this strategy is 100 % degree of sulfonation owing to the presence of one sulfonate group per polymer repeating unit. In addition, despite the high degree of sulfonation, PSSH-coated silica nanoparticles do not leach from the membrane when hydrated.

Results and discussion

Surface-initiated ATRP of sodium 4-styrenesulfonate

The synthetic route to hybrid poly(4-styrenesulfonic acid)/silica particles is shown in **Scheme 4**. Colloidal silica (Snowtex-XS, Nissan Chemical Corporation) was received in the form of an aqueous dispersion in pH 9-10 water. Ion exchange with cetyltrimethylammonium bromide (CTAB) rendered the particles hydrophobic, causing them to aggregate.[201] **Figure 21** shows IR spectra for the Snowtex-XS particles and their derivatives. Bands at 3000-2800 cm^{-1} confirmed the presence of the CTAB ion on the particle surface. Treating the particles with (11-(2-bromo-2-methyl)propionyloxy) undecyltrichlorosilane immobilized an α-bromodimethyl ester, an ATRP initiator, to the silica nanoparticle surface. The appearance of a band at 1730 cm^{-1} (C=O), a broad C-O stretching band at 1200-1000 cm^{-1}, and further development of the C-H bands at 3000-2800 cm^{-1} are consistent with the successful anchoring of the initiator to the nanoparticle

surface. Finally, PSSNa was grown from the nanoparticle surface at room temperature using ATRP (water/methanol (v/v = 3/1), $[M]_o$:[surface initiator]:[CuBr]:[$CuBr_2$]:[bpy] = 70:1:2:0.2:6) to yield hybrid poly(sodium 4-styrenesulfonate)/silica (silica-PSSNa) nanoparticles. The particles were collected by centrifugation followed by further purification and no PSSNa polymer was found in the reaction solution implying that the polymerization was restricted to the particle surfaces. The IR spectrum of silica-PSSNa-3 (**Table 1**) is consistent with a substantial shell of PSSNa grown from the particles: new bands appeared for sp^2 C-H stretching (3200-3000 cm^{-1}), a sharp in plane bending peak at 1010 cm^{-1} and a pattern of combination and overtones (2000-1800 cm^{-1}) consistent with a 1,4-substituted benzene ring, and most prominently, ν_a and ν_s bands for the sulfonate group (S=O, 1200 and 1040 cm^{-1}). Acidification with 1M HCl converted the sodium salt to the corresponding sulfonic acid.

Scheme 4. Synthetic route to hybrid poly(4-styrenesulfonic acid)/silica nanoparticles.

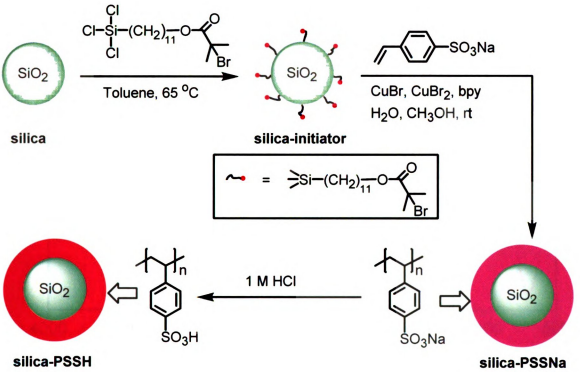

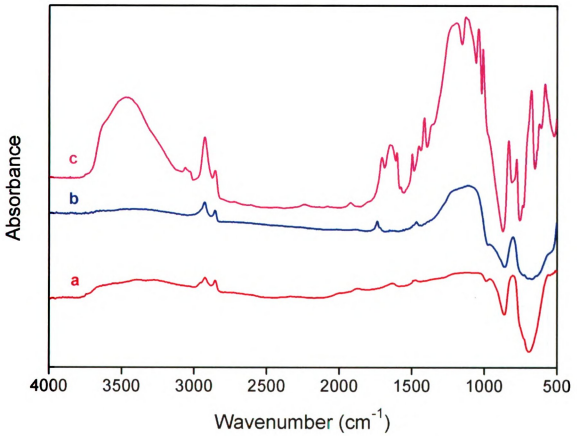

Figure 21. FTIR spectra of **(a)** Snowtex-XS nanoparticles, CTAB salt; **(b)** nanoparticles with surface anchored initiators; and **(c)** silica/PSSNa-3 nanoparticles. Samples were made into pellets with KBr.

Thermal gravimetric analysis (TGA) results are consistent with the IR data. As shown in **Figure 22**, CTAB modified Snowtex-XS nanoparticles have an onset for weight loss at ~230 ºC, and a final weight loss of ~13 % at 900 ºC, which corresponds to decomposition of CTAB, and loss of water due to condensation of surface silanols. The silica-initiator particles also showed an onset for weight loss at ~230 ºC. Their 27 % weight loss at 900 ºC is consistent with thermal degradation of surface initiator moiety.

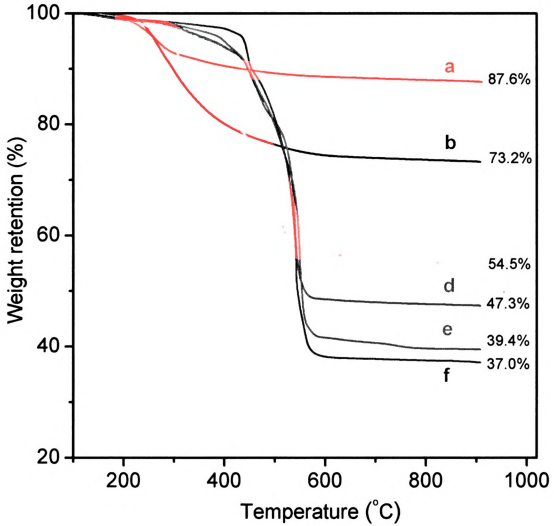

Figure 22. Thermogravimetric analysis of **(a)** Snowtex-XS nanoparticles, CTAB salt; **(b)** silica-initiator nanoparticles; **(c)** silica-PSSNa-1 nanoparticles; **(d)** silica-PSSNa-2 nanoparticles; **(e)** silica-PSSNa-3 nanoparticles; and **(f)** linear PSSNa. See **Table 1** for details of silica-PSSNa-(1-3). All samples were run in air at a heating rate of 10°/min.

To synthesize particles with predictable surface polymer molecular weights, we characterized the kinetics for surface-initiated ATRP of sodium 4-styrenesulfonate. Since tracking the course of the polymerization was complicated by the poor solubility of silica-PSSNa particles in the polymerization solution (water and methanol), we chose to follow monomer consumption by ^{1}H

NMR, using sodium *p*-toluenesulfonate as an internal standard because of its similar structure and solubility, and its distinct proton chemical shifts. Monomer consumption was calculated from the integration of the ^{1}H NMR resonances for the methyl group of sodium *p*-toluenesulfonate (2.27 ppm) and the vinyl proton at 5.3 ppm in sodium 4-styrenesulfonate (**Figure 23**).

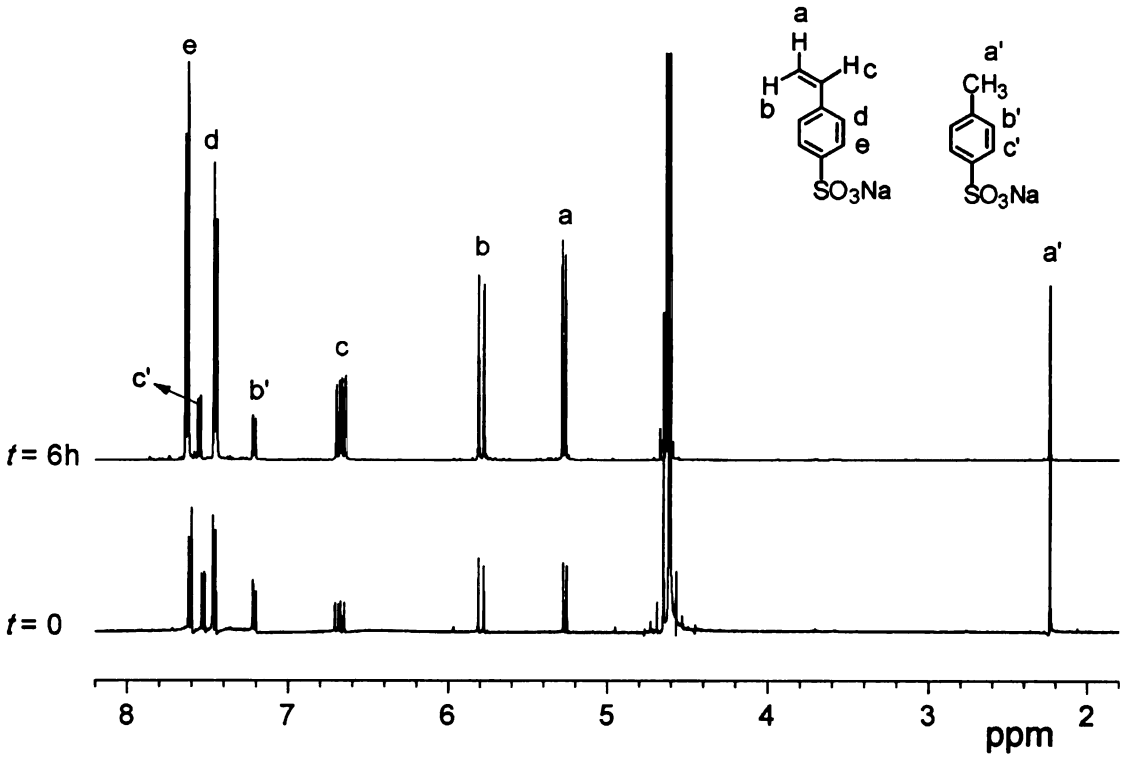

Figure 23. 500 MHz ^{1}H NMR spectra of a representative polymerization sample for the kinetic study.

The plot of $\ln([M]_o/[M])$ as a function of polymerization time is nearly linear up to 69 % conversion (240 min) consistent with a surface polymerization first-order in monomer concentration (**Figure 24**). At higher conversions, curvature in the polymerization data indicates a decreasing polymerization rate, likely due to fewer growing chains as a result of termination (Equilibrium effects might also

affect the polymerization, but $[M]_{eq}$ is not known for sodium 4-styrenesulfonate). We were pleased that the silica nanoparticles did not have a negative effect on the surface polymerization. Samples taken at t = 20 min (conversion = 10 %, silica-PSSNa-1), t = 1 h (26 %, silica-PSSNa-2), and t = 4 h (69 %, silica-PSSNa-3) were isolated by centrifugation and purified for further characterization.

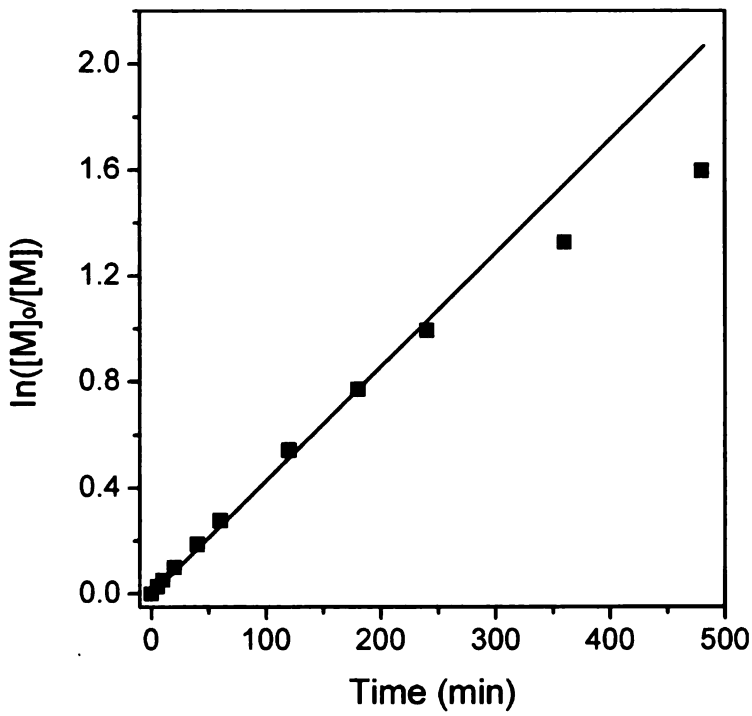

Figure 24. Surface polymerization kinetics of sodium 4-styrenesulfonate from silica nanoparticles. The polymerization was run at room temperature in water/methanol (v/v = 3/1) and an initial monomer concentration ($[M]_o$) of sodium 4-styrenesulfonate is 0.5 mM. The ratios of $[M]_o$:[standard]:[surface initiator]: [CuBr]:[$CuBr_2$]:[bpy] were approximately 70:10:1:2:0.2:6.

Three samples: silica-PSSNa-1, silica-PSSNa-2, and silica-PSSNa-3, which were prepared by polymerizing sodium 4-styrene sulfonate from silica-initiator surfaces for increasing reaction times, were characterized by TGA (**Figure 22**). Their weight loss at 900 °C increased from 45 % (silica-PSSNa-1) to

53 % (silica-PSSNa-2) to 61 % (silica-PSSNa-3), indicating that the PSSNa molecular weight increases with the polymerization time. The TGA trace of linear PSSNa exhibited three mass loss events. While definite assignments are not possible without corroboration by other techniques, the weight losses likely correspond to elimination of residual water, desulfonation, and finally degradation of the polymer backbone commencing at ~450 °C. The onset for degradation of silica-PSSNa-1 was ~280 °C, much lower than silica-PSSNa-2 and silica-PSSNa-3. The small mass loss, the shorter polymerization time, and a degradation onset comparable to the silica-initiator particles all argue for silica-PSSNa-1 being comprised of low molecular weight PSSNa chains. Interestingly, linear PSSNa had a nonvolatile residue at 900 °C even in an oxidative atmosphere.[202]

Consistently with the NMR data, the TGA results indicate increasing molecular weights with polymerization time. Using the residual mass of both the silica-initiator nanoparticles and linear PSSNa at 900 °C, and the monomer conversions determined by ^{1}H NMR, the expected TGA weight loss at 900 °C was calculated for silica-PSSNa-1, silica-PSSNa-2, and silica-PSSNa-3 (**Table 1**). The data are in reasonable agreement with the actual TGA losses, ~4 % less than expected. The result suggests that the amount of surface-grafted PSSNa increased linearly with monomer conversion, polymerization in solution was insignificant, the number of growing chains on particle surface was constant, and the surface ATRP was a living/controlled reaction from t = 20 min to t = 4 h.

Table 1. Characteristics of particles isolated at different polymerization time.

Particles	ATRP time (min)[a]	Monomer conversion (%)[b]	Calculated TGA weight retention at 900 °C (%)[c]	Actual TGA weight retention at 900 °C (%)[d]
silica-PSSNa-1	20	10.4	58.1	54.5
silica-PSSNa-2	60	25.7	50.1	47.3
silica-PSSNa-3	240	69.4	43.3	39.5

[a] The polymerization was run at room temperature in water/methanol (v/v = 3/1) and an initial monomer concentration ($[M]_o$) of sodium 4-styrenesulfonate is 0.5 mM. The ratios of $[M]_o$:[standard]:[surface initiator]: [CuBr]:[$CuBr_2$]:[bpy] were approximately 70:10:1:2:0.2:6.

[b] determined by 1H NMR, using sodium *p*-toluenesulfonate as an internal standard

[c] run in air at a heating rate of 10 °C/min

The CTAB-coated silica particles have a diameter of around 7 nm, consistent with the data provided by the supplier. As shown in **Figure 25a**, the dried particles agglomerate, but after surface polymerization, the cores of the silica-PSSNa nanoparticles are dispersed, consistent with polymerization of PSSNa from the particle surfaces (**Figure 25b**). Imaging the polyelectrolyte phase required staining with metal ions.

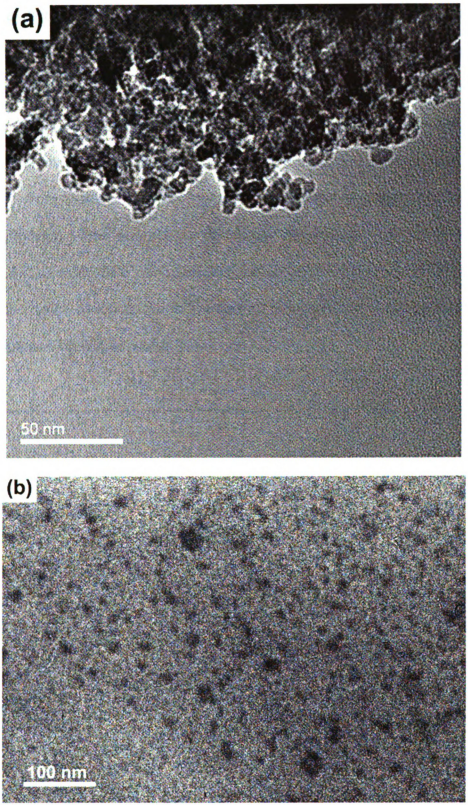

Figure 25. TEM images of **(a)** dried Snowtex-XS nanoparticles, CTAB salt; and **(b)** silica-PSSNa-3 nanoparticles.

The hybrid nanoparticles which were blended with PVDF to make composite membranes were named silica-PSSH nanoparticles and their precursors were silica-PSSNa hybrid nanoparticles. As displayed in **Figure 26**, the FT-IR spectrum of silica-PSSNa hybrid nanoparticles was dominated by the characteristic absorption peaks of PSSNa with the strong O–H stretching bond at 3435 cm^{-1} from water absorbed by the hygroscopic surface poly(sodium 4-styrenesulfonate). The absorption bands of silica-PSSH nanoparticles were similar to the silica-PSSNa nanoparticles, except for the stronger and broader O–H stretching peak, which is due to the strong hydrogen bonding between sulfonic acid groups and absorbed water.

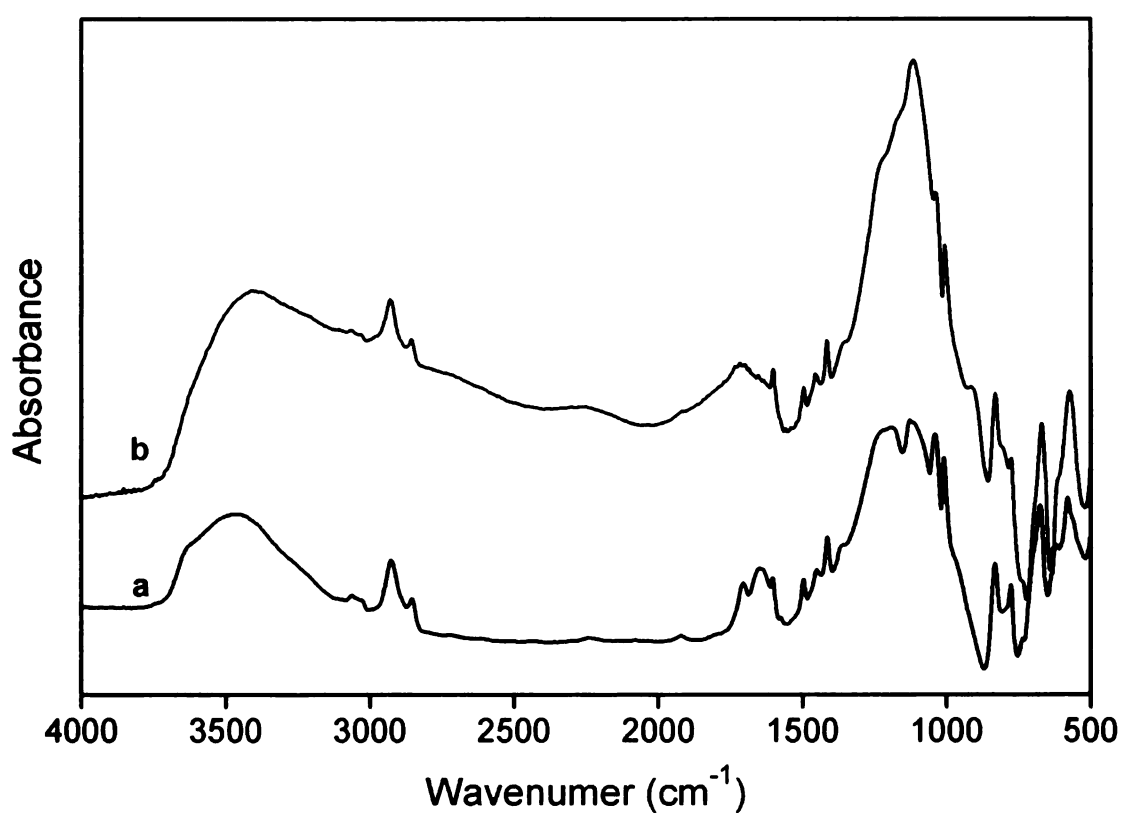

Figure 26. FTIR spectra of **(a)** silica-PSSNa nanoparticles; and **(b)** silica-PSSH nanoparticles.

As shown in **Figure 27**, the weight loss of silica-PSSNa particles at 900 °C was about ~58 %, which indicated a thick polymer layer on the surface of the hybrid nanoparticles. A comparison of the TGA traces of silica-PSSNa and silica-PSSH particles suggested that the free acid was less thermally stable than the sodium salt in an oxidative atmosphere. The initial weight loss for silica-PSSNa nanoparticles occurred at ~400 °C, while silica-PSSH degraded earlier and at 900 °C left a lower non-volatile residue than its sodium salt. The silica-PSSH nanoparticles degraded in two steps: the first step from 200 to 400 °C should correspond to desulfonation, while the second step was more likely the degradation of the polystyrene backbone.

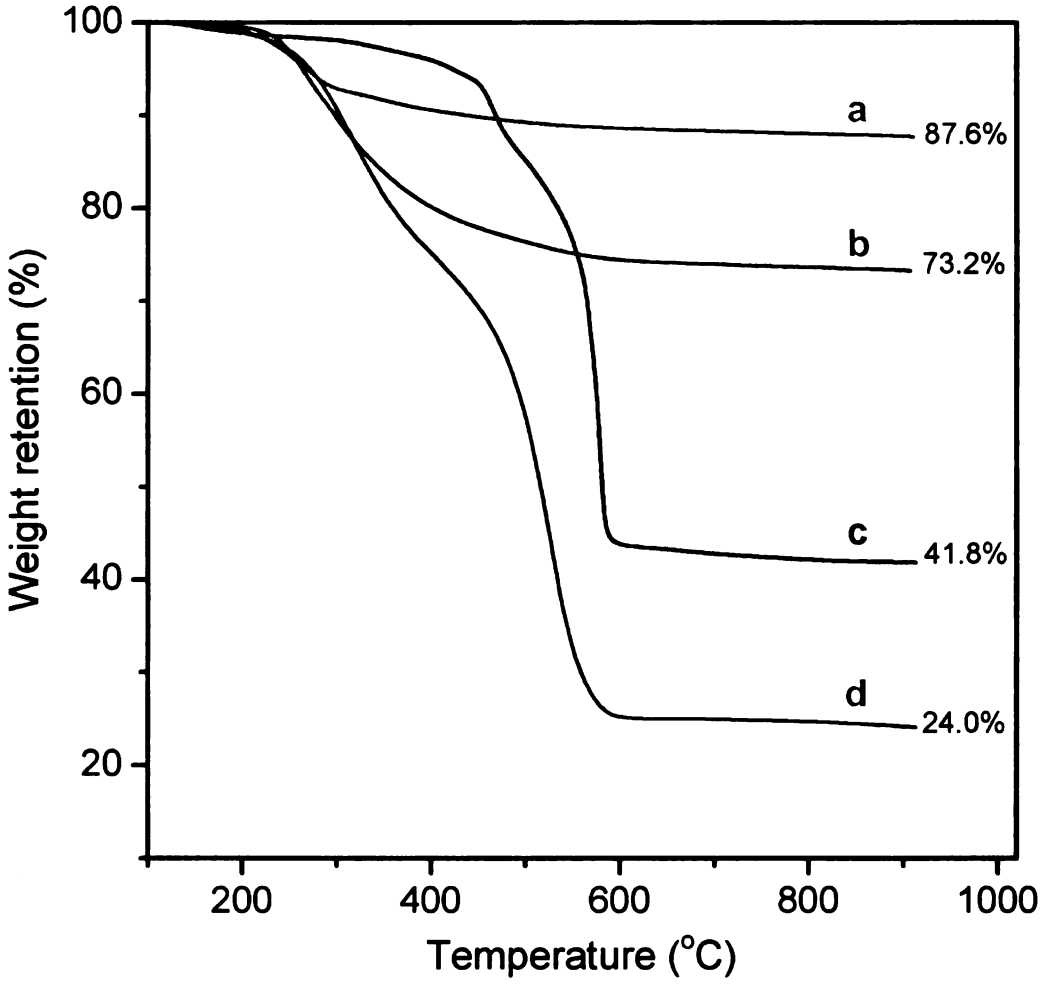

Figure 27. Thermogravimetric analysis of **(a)** Snowtex-XS nanoparticles, CTAB salt; **(b)** silica-initiator nanoparticles; **(c)** silica-PSSNa nanoparticles; and **(d)** silica-PSSH nanoparticles.

Fabrication and characterization of composite PEMs from the blending of silica-PSSH nanoparticles and PVDF

In conventional polystyrene based PEMs, the sulfonic acid groups are introduced after polymerization by sulfonation reagents, such as chlorosulfonic acid, concentrated sulfuric acid, or fuming sulfuric acid. However, most "post-polymerization" sulfonation reactions are associated with low degrees of sulfonation, cross-linking, and polymer degradation.[2] Since it is widely accepted

that PEM conductivity is strongly related to the number of charge carriers (H^+), the preference is the highest degree of sulfonation without sacrificing the PEMs' mechanical properties. The direct polymerization of sulfonated styrene-like monomers provides one sodium sulfonate group per repeating unit, 100 % sulfonation.

Composite membranes were obtained by solution-casting a DMF mixture of silica-PSSH hybrid particles and PVDF onto glass slides at 50 °C followed by further drying under vacuum overnight (**Figure 28**). The dried membranes (15-35 μm thick, ~3x0.5-1 cm^2) were peeled from the glass slides once immersed in water. In composite membranes, silica-PSSH hybrid particles are the proton donors and PVDF provides mechanical stability (**Scheme 5**). **Table 2** summarizes the composition and experimental results for the composite membranes.

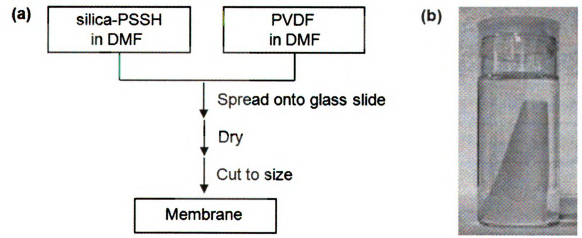

Figure 28. **(a)** Schematic illustration of composite proton exchange membrane fabrication. **(b)** Photo of a 4x4 cm^2 composite membrane with 40 wt% silica-PSSH particles.

Scheme 5. Schematic diagram illustrating the structure of a composite membrane.

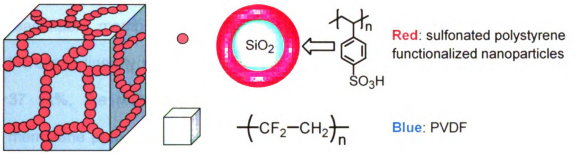

Table 2. Summary of silica-PSSH/PVDF membrane characteristics.

PEMs (particle wt%)	IEC (meq/g)	Conductivity at rt (mS/cm)	Conductivity at 60 °C (mS/cm)	Swelling ratio (%)	Water uptake (wt%)
0	0	0	0	<3	0
10	0.47	2	4	<3	8
20	0.93	22	38	<3	15
30	1.40	27	61	<3	25
40	1.86	60	11	<3	43
50	2.33	70	12	<3	95
Nafion 117[a]	0.9[15]	62	11	18[15]	21

[a] Nafion 117 was included for comparison.

Proper "water management" is critical for PEMs. While water contributes to the dissociation of SO_3H groups and acts as "vehicles" that transport protons from the anode to the cathode, membranes with high water uptake are usually

associated with severe swelling and poor mechanical strength. A proper water uptake is essential for facilitating high proton conductivity as well as maintaining reasonable membrane stability. As shown in **Figure 29**, the water uptake increased linearly with the silica-PSSH particle content up to ~37 wt%. Above 37 wt%, the water uptake increased significantly, indicating a change in membrane phase morphology.[203-205] Generally, when the volume fraction of the conductive phase in a composite membrane is low, sulfonic acid groups are isolated in ionic clusters in the matrix, and only a fraction of the clusters are accessible to water. However, when the particle content reaches the percolation threshold, the volume fraction at which the conductive phase becomes continuous, the water uptake increases rapidly. PVDF is hydrophobic and thus pure PVDF membrane (with 0 wt% particle) has a zero water uptake.

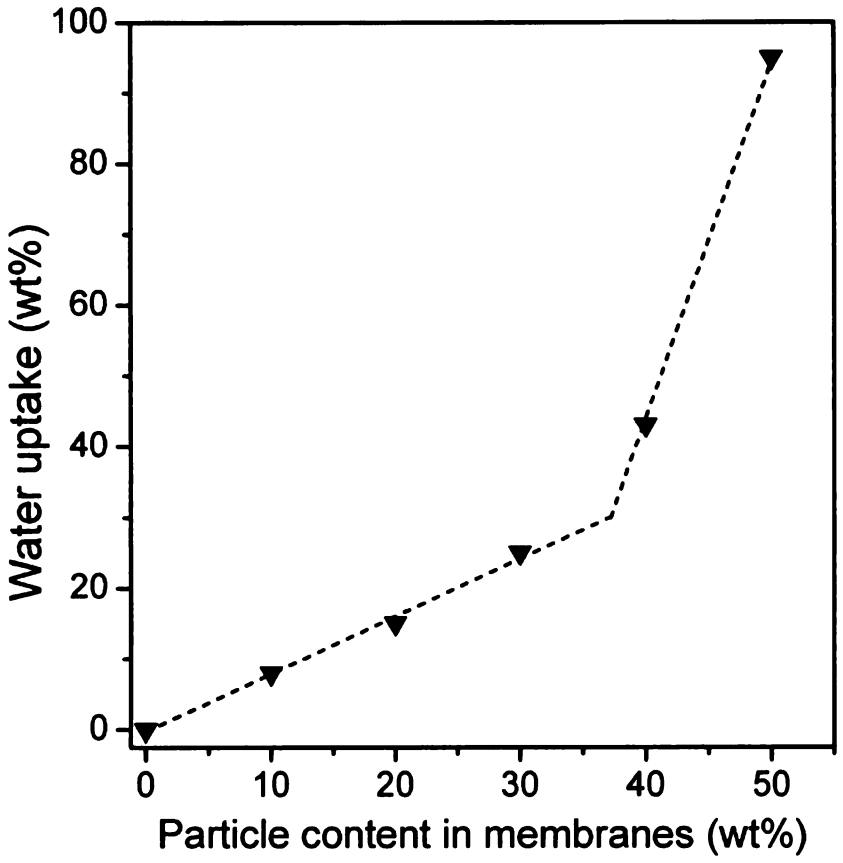

Figure 29. Water uptakes of composite membrane as a function of particle contents. The membrane water uptake was measured gravimetrically at room temperature. (The dotted line is a guide to the eye)

The ion exchange capacity (IEC), expressed as mmol acid/g sample, defines the density of charge carriers in a membrane and is directly related to a membrane's ability to absorb and retain water. Water uptake is directly related to membrane IEC values and a sharp increase in IEC value is usually interpreted as exceeding threshold for forming continuous hydrophilic domains.[50,203,206] As shown in **Figure 30**, the IEC tracks the water uptake vs particle content, as expected, since there is a 1:1 correspondence between the silica-PSSH particle content and the IEC.

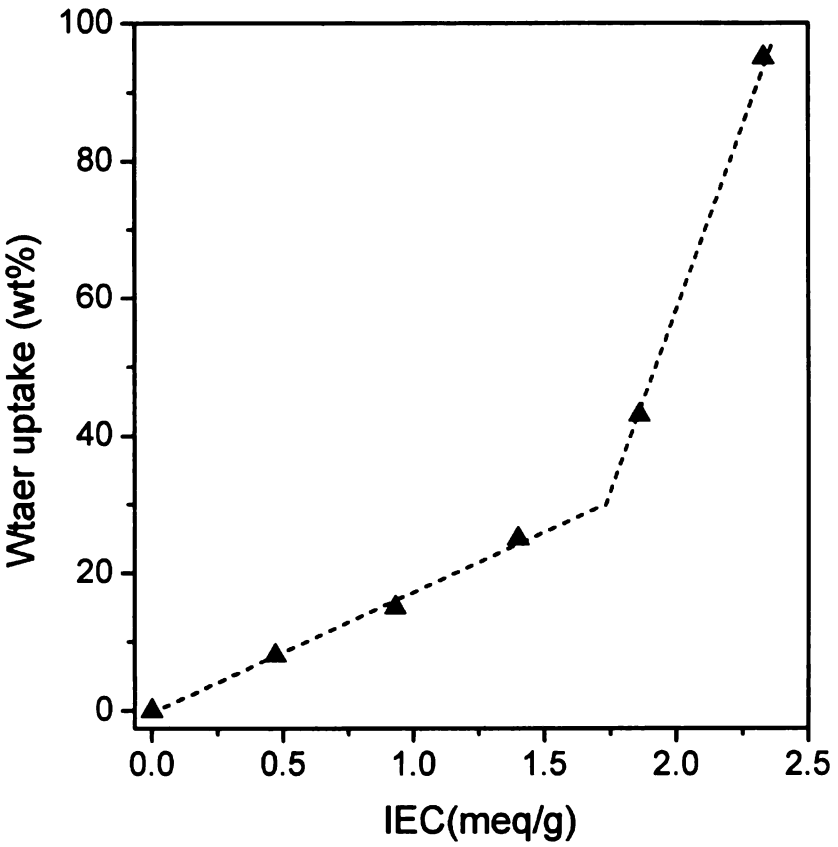

Figure 30. Water uptakes as a function of membrane IEC. The membrane water uptake was measured gravimetrically at room temperature. (Dotted lines were a guide to the eye)

Proton conductivity is one of the most important parameters for evaluating the performance of PEMs as well as the practicability of fuel cells. Since the proton conductivity is strongly related to the number of charge carriers (H^+), a high silica-PSSH particle content is preferred without the sacrifice of PEMs' mechanical properties. As seen in **Figure 31**, the pure PVDF membrane (0 wt% particle) has no measurable proton conductivity, consistent with its lack of charge carriers. However, membranes with silica-PSSH particles were conductive, and the conductivity increased linearly as a function of particle content.

Nafion 117 was used as a benchmark and as a control for the accuracy of conductivity measurements. At room temperature, the proton conductivity of Nafion 117 was 62 mS/cm, which is comparable to the reported data for Nafion 117 at room temperature (60 mS/cm).[207] Membranes with 40 and 50 wt% particles had conductivities of 60 and 70 mS/cm at room temperature, respectively, comparable to or higher than Nafion 117 run under the same conditions. The high conductivity of the PEMs is consistent with a continuous hydrophilic phase comprised of hybrid particles and water, similar to the continuous proton network of channels of Nafion.[11]

The proton conductivity was relatively low at room temperature but increased rapidly as the temperature was raised to 60 °C. Proton transport is thermally activated, so higher temperatures lead to improved proton conductivities.

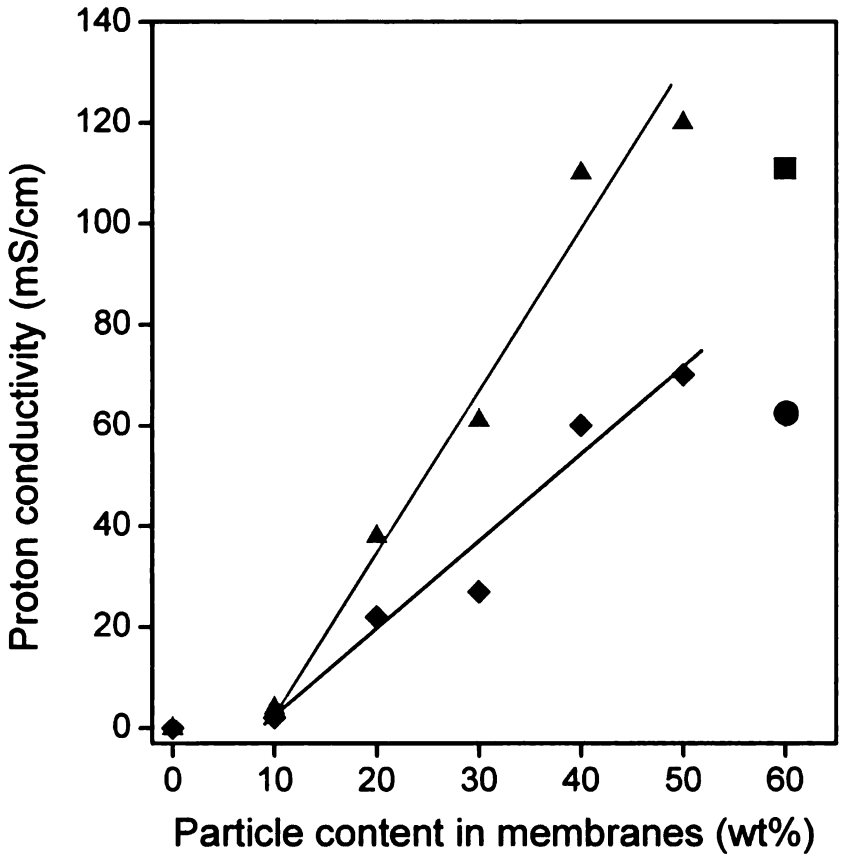

Figure 31. Membrane proton conductivities as a function of particle content for composite PEMs at 100% RH and room temperature (◆) and 60 °C (▲). Data for Nafion 117 at room temperature (●) and at 60 °C (■) was shown for comparison. (Lines were a guide to the eye)

Proton conductivity is strongly correlated to IEC, since the IEC defines the carrier density in membranes. **Figure 32** shows the proton conductivity as a function of membrane IEC. As displayed, the conductivity increased linearly with the increasing IEC.

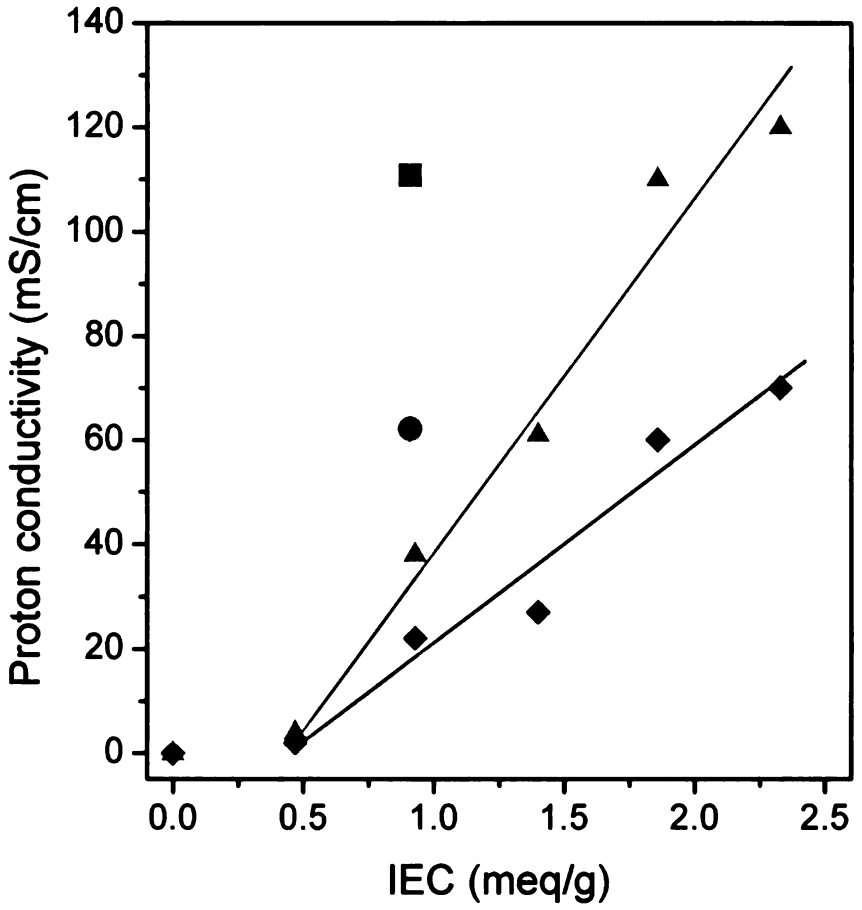

Figure 32. Membrane proton conductivity as a function of IEC for composite PEMs at 100% RH and room temperature (◆) and 60 °C (▲). Data for Nafion 117 at room temperature (●) and at 60 °C (■) was shown for comparison. (Lines were a guide to the eye)

It was of great interest to investigate the proton conductivity vs water uptake, because water molecules were needed as the mobile phase to facilitate proton transport. As demonstrated in **Figure 33**, there was an almost linear relationship between proton conductivity and water uptake up to around 40 wt%, which was followed by a far slower increasing rate. This result suggested a threshold close to 40 wt% water uptake, which was corresponded with 40 wt% particle content in composite membranes.

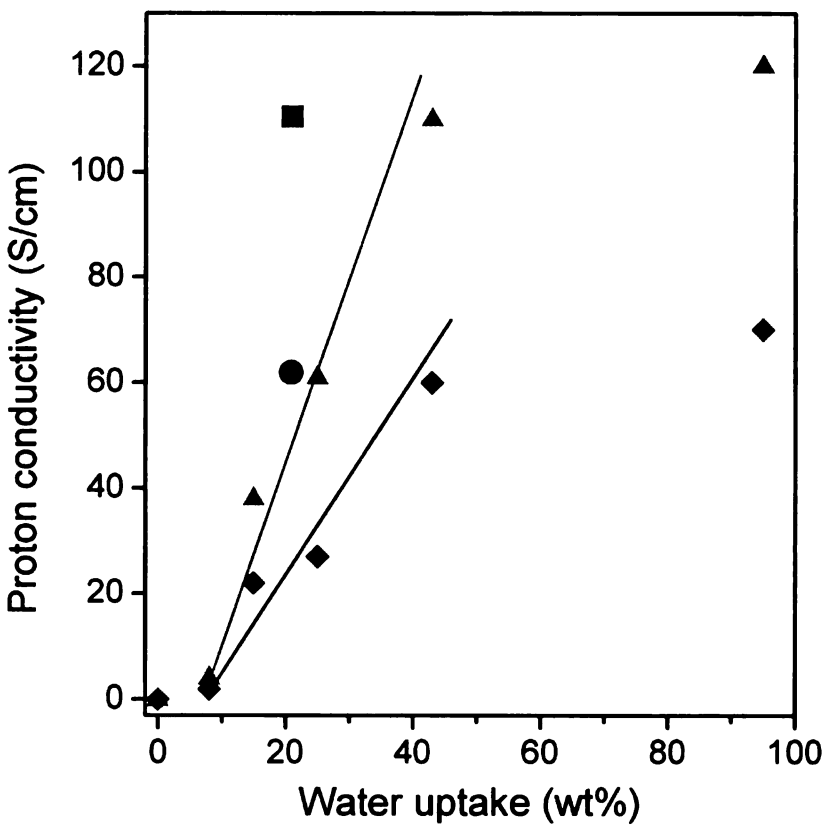

Figure 33. Membrane proton conductivity as a function of water uptake for composite PEMs at 100% RH and room temperature (◆) and at 60 °C (▲). Data for Nafion 117 at room temperature (●) and at 60 °C (■) was shown for comparison. (Lines were a guide to the eye)

The nature of the acid groups, chemical composition, and microstructure of membranes all contribute to the desirable properties of PEMs. In order to study membrane microstructure, the cross-sectional slices of composite membranes with 40 and 50 wt% particles were analyzed with TEM (**Figure 34**). Stained with Ag^+ ions, the hybrid nanoparticles showed up as dark regions in a bright PVDF matrix. A phase-separated morphology was observed in both TEM images. The hybrid nanoparticles aggregated to form continuous domains

immiscible with PVDF matrix, which is consistent with the plot of water uptake vs IEC values.

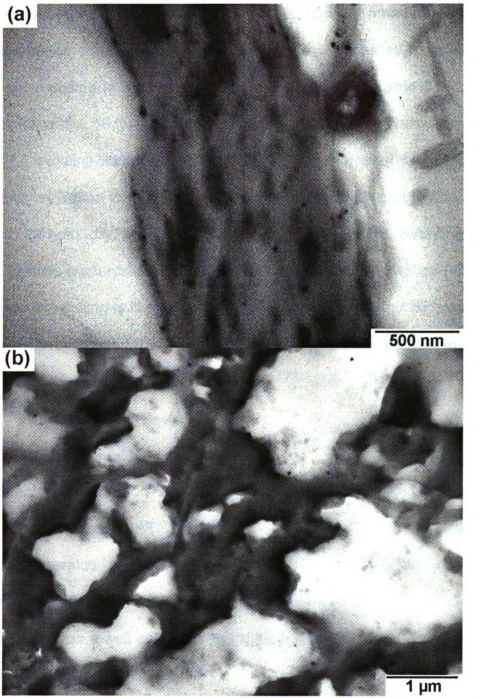

Figure 34. Cross-sectional TEM images of membranes with **(a)** 40 wt% particles; and **(b)** 50 wt% particles.

It has been a significant challenge to design PEMs with high proton conductivity and minimal swelling. Dimensional stability, which is the change in the measured membrane size for the dry and water saturated states, is a very important parameter for practical fuel cell applications. If membranes swell too much, electrodes can detach from the membrane surfaces as most electrodes don't swell, resulting in mechanical stress.[208] As listed in **Table 2**, Nafion 117 swells significantly, 18 % from the dry to wet state. The severe expansion of Nafion 117 explains its poor performance in direct methanol fuel cells, as the permeability of Nafion to methanol is due to the high swelling of Nafion in water. However, in both dry and hydrated states, all composite membranes with different particle contents did not show any measurable size change (<3%). The minimal water swelling is likely due to the crystalline structure of the hydrophobic PVDF, which suppressed the water swelling of silica-PSSH particles in hydrated membranes.

Conclusion

Direct polymerization of sodium 4-styrenesulfonate was carried out on ~7 nm silica particles by ATRP at room temperature in aqueous system. This approach generated polyelectrolyte-coated silica nanoparticles with 100 % polymer sulfonation degree. Kinetic study demonstrated that the surface polymerization was a well controlled polymerization with first order kinetics up to six hours followed by slightly slower reaction rate, which might be due to polymer chain termination. This methodology provides an easy approach to generate

polyelectrolyte functionalized hybrid nanoparticles with a high surface-to-volume ratio. TEM images proved that the anionic polyelectrolyte assisted the dispersion of hybrid particles in water and minimized particle aggregation. IR spectroscopy confirmed the presence of surface functional groups on silica particles and the analysis of the TGA data confirmed the kinetic study results.

Solution-casting the mixture of the acidified hybrid particles and PVDF formed composite proton exchange membranes. In addition to traditional advantages of blend PEMs, such as easy design, synthesis, and processing, the composite membrane system does not have the side effects related to "post-sulfonation" reactions. Both the membrane water uptake and proton conductivity increased linearly with the increase of particles in composite membranes and a drastic increase showed up above a percolation threshold. The composite membranes with 40 and 50 wt% particle contents revealed proton conductivities comparable to or even higher than Nafion 117 under the same testing conditions. The excellent conductivity might be due to either the high IEC value or the phase-separated morphology of composite membranes. No water swelling was observed with the composite membranes as the crystalline structure of the hydrophobic PVDF matrix constrained the expansion of hybrid nanoparticles. Moreover, this composite system is more cost effective compared to the perfluorinated PEMs due to much easier synthesis and processing.

Experimental Section

Materials

Sodium 4-styrenesulfonate, CuBr (99.999%), $CuBr_2$, (99.999%), cetyltrimethylammonium bromide (CTAB), PVDF (M_w = 534,000 Da), 2, 2'-dipyridyl (bpy, 99+ %), and Nafion 117 were used as received from Sigma-Aldrich except for bpy, which was sublimed prior to use. Snowtex-XS colloidal silica, a gift from the Nissan Chemical Corporation, was received as an aqueous dispersion of pH 9-10. Toluene was distilled over sodium using benzophenone as an indicator and dimethylformamide (DMF) was dried over activated 4Å molecular sieves. The disodium salt of N,N,N',N'-ethylenediaminetetraacetic acid (EDTA·2Na) was purchased from Spectrum. All other chemicals and solvents were ACS reagent grade and used as received from commercial suppliers without further purification unless otherwise specified.

Characterization.

^1H NMR analyses were performed at room temperature in deuterated water on a Varian UnityPlus 500 spectrometer at 500 MHz with the residual solvent proton signals as chemical shift standards. FT-IR spectra were acquired from a Mattson Galaxy 300 spectrometer purged with dry nitrogen, with the signal averaging 128 scans at a resolution of 4 cm^{-1}. All IR samples were dried, mixed with KBr, ground, and then pressed into pellets.

Thermogravimetric analyses (TGA) were carried out in air on Perkin-Elmer TGA 7 instruments at a heating rate of 10 °C/min. TGA samples were dried under

vacuum at 80 °C overnight prior to use. Dried samples were held at 120 °C in the TGA apparatus for 30 min prior to initiating the run.

The microstructure of particles and composite membranes were imaged using either a JEOL-100CX or a JEOL-2200FS transmittance electron microscope. To prepare the TEM sample for dried Snowtex-XS, particles were dispersed in toluene by ultrasonication, and then a drop of the suspension was drop-cast onto a carbon-coated copper mesh grid followed by solvent evaporation in air. The TEM sample of silica-PSSNa particles was prepared in a similar way from their water suspension. To prepare membrane cross-sections for TEM analysis, membranes were immersed in 0.5 M $AgNO_3$ solution overnight to stain the ionic domains by ion exchange of sulfonic acid groups for silver. Samples were rinsed with water, and then dried under vacuum at 80 °C overnight. The stained membranes were embedded in epoxy resin, dried at 50 °C for 24 h, and then sectioned with an ultramicrotome to generate ~100 nm thick slices. The slices were picked up with copper grids for TEM analysis.

Isolation of silica nanoparticles from Snowtex-XS

Cetyltrimethylammonium bromide (3 g) was added to 100 mL of Snowtex-XS and the mixture was stirred at 50 °C for 30 min. The silica particles were then collected by centrifugation and re-dispersed in 100 mL of Milli-Q water to remove excess salt from the particle surfaces. After repeating the washing process four times, the silica particles were dried under vacuum at 80 °C overnight.

Immobilization of ATRP initiators onto silica particles

Dry silica particles (1 g) were dispersed in 100 mL of dry toluene by ultrasonication. Using a syringe, 0.5 mL of freshly synthesized initiator, (11-(2-bromo-2-methyl)propionyloxy)undecyltrichlorosilane,[196] was added to the particles and the reaction mixture was stirred under a N_2 atmosphere at 65 °C overnight. The crude initiator-coated particles (silica-initiator) were isolated by centrifugation, re-dispersed in 20 mL of dry toluene, precipitated from 100 mL of pentane, and then collected by centrifugation. The dispersion-precipitation-centrifugation washing process was repeated six times to remove physisorbed initiators from particle surfaces. Silica-initiator particles were then dried under vacuum at 80 °C overnight.

Surface ATRP of sodium 4-styrenesulfonate

The surface-initiated ATRP of sodium 4-styrenesulfonate was carried out at room temperature under N_2 with CuBr/$CuBr_2$ and bpy as the catalytic system. Sodium *p*-toluenesulfonate was used as an internal standard for determining monomer conversion. The ratios of $[Monomer]_o$:$[standard]_o$:$[surface\ initiator]_o$:$[CuBr]_o$:$[CuBr_2]_o$:$[bpy]_o$ were approximately 70:10:1:2:0.2:6, with the initial concentration of surface initiator estimated from TGA analyses of silica-initiator particles. A typical synthesis is described. Sodium 4-styrenesulfonate (0.43 g, 2.09 mmol), sodium *p*-toluenesulfonate (60 mg, 0.31 mmol), $CuBr_2$ (1.4 mg, 0.006 mmol), bpy (28 mg, 0.18 mmol), 3 mL of Milli-Q water, and 1 mL of methanol were charged into a 10 mL Schlenk flask equipped with a magnetic

stirrer. After complete dissolution of the solids, silica-initiator particles (62 mg, 0.03 mmol of surface initiator (calculated from TGA)) were added and then the mixture was sonicated for 10 min to fully disperse the particles. After four freeze-pump-thaw cycles, the Schlenk flask was filled with nitrogen at room temperature and sonicated for 15 min to afford a fine dispersion of silica-initiator particles. An initial sample (~0.2 mL) was removed via a syringe and diluted with 1 mL of Milli-Q water and designated as sample t = 0. Finally, CuBr (8.6 mg, 0.06 mmol) was charged into the Schlenk flask under a flow of nitrogen and with a rapid stirring.

At various reaction times, 0.2 mL samples were transferred from the reaction mixture to vials, and after diluting with 1 mL of Milli-Q water, the vials were shakened to terminate the surface polymerization. The samples were left undisturbed overnight, allowing the particles to settle at the bottom of the vial as a gel. The upper water layer was removed from the vial and dried under vacuum, and the remaining solids were analyzed by ^{1}H NMR for conversion. An aqueous solution of EDTA·2Na was added to the particle suspension to remove residual Cu^{2+} until the faint blue color associated with the particles had disappeared. The hybrid particles were then isolated by centrifugation and washed extensively with water to remove excess monomer, standard, and EDTA·2Na. Finally, acetone was added to precipitate the particles, which were then collected and dried under vacuum at 80 °C overnight.

General procedure for acidifying silica-PSSNa particles

A 1 M HCl solution was added to an aqueous suspension of silica-PSSNa to exchange Na^+ with H^+. After 48 h, the silica-PSSH nanoparticles were centrifuged, washed extensively with water, precipitated from acetone, and dried under vacuum at 80 °C overnight.

Solution polymerization of sodium 4-styrensulfonate - linear PSSNa

A round-bottom flask was charged with sodium 4-styrenesulfonate (1.0 g, 4.9 mmol) and 5 mL of ethylene glycol, and the mixture was stirred until homogeneous. The reaction system was purged with N_2 for 30 min, and then the flask was transferred to an oil bath maintained at 60 °C. The catalyst system was made by dissolving $Na_2S_2O_5$ (0.035 g, 0.18 mmol) and $K_2S_2O_8$ (0.065 g, 0.24 mmol) in 1 mL and 2 mL of Milli-Q water, respectively. The two solutions were injected into the reaction flask, separately, and then the reaction mixture was stirred under a N_2 atmosphere at 60 °C for 5 h. The crude poly(sodium 4-styrensulfonate) (PSSNa) was precipitated from acetone, washed with acetone, and then dried under vacuum at 80 °C overnight.

Preparation of composite membranes

Composite membranes were fabricated by the solvent-casting method. This procedure describes the preparation of 10 mg membranes. Predetermined amounts of PVDF and silica-PSSH nanoparticles were dissolved in DMF in separate vials. Each solution was fixed at 0.05 g/mL, and the total mass of the

particles and PVDF was 10 mg. The two solutions were combined and stirred until the system was homogeneous. Membranes were solution-cast by pouring the mixture onto a clean glass plate at 50 °C, typically covering 4x1 cm^2 area. After 1 hour, the membrane had turned translucent, and the glass plate was transferred to a vacuum at 50 °C for further drying overnight. The dried membranes (15-35 μm thick) were cut to size (~3×0.5-1 cm^2) and then removed from the substrate by immersing the plate in water. The as-synthesized membranes were soaked in 1 M HCl for 48 h to ensure that all sulfonate groups in the membranes were in their acidic form. The membranes were then washed extensively with water, and prior to conductivity tests, PEMs were stored in Milli-Q water.

Conductivity measurements

The proton conductivities of membranes were measured with an alternating current (AC) impedance analyzer HP 4192A over the frequency range from 5 Hz to 13 MHz. Membranes were placed between two Pt electrodes in a home-made Teflon cell. The entire setup was kept in Milli-Q water at controlled temperatures for at least 10 min to saturate membranes and then impedance was measured in in-plane direction. From the Nyquist plot, the resistance of the membrane was estimated, and then the conductivity of the membrane was calculated using the electrodes distance and membrane cross-sectional area, as shown in equation 1:

$$\sigma = \frac{L}{R \cdot A} \qquad (1)$$

Where σ is the conductivity of the membrane, L represents the distance between two electrodes, A stands for the membrane cross-sectional area, and R is the bulk membrane resistance estimated from the Nyquist plot.

Water uptake

Water uptake of all membranes was measured gravimetrically. After equilibration in Milli-Q water for two days at room temperature, membranes were removed from water, and weighed after the surface water was quickly removed by a Kim-wipe. Membranes were then dried under vacuum at 50 °C overnight and the weight of dried membrane was measured. The membrane water uptake was calculated according to equation 2:

$$\text{Water uptake} = \frac{W_{\text{wet}} - W_{\text{dry}}}{W_{\text{dry}}} \times 100\% \qquad (2)$$

where W_{wet} stands for the mass of wet membranes and W_{dry} represents the weight of dried membranes.

Dimensional stability

Membranes were saturated in Milli-Q water for two days at room temperature prior to measuring the dimensions of swollen membranes. After drying under vacuum at 50 °C overnight, the dimensions of the dried membrane were measured. The swelling ratio was calculated from the length (longest dimension) of the membrane, as shown in equation 3:

$$\text{Swelling ratio} = \frac{l_{wet} - l_{dry}}{l_{dry}} \times 100\% \qquad (3)$$

where l_{wet} and l_{dry} represent the lengths of wet and dried membranes, respectively. The uncertainty in the measurement is <3%.

Theoretic ion exchange capacity (IEC)

The ion exchange capacity of membranes was estimated from the TGA weight retention data of particles and particle weight fractions in membranes. The IEC was calculated according to equation 4:

$$\text{IEC} = \frac{m_{H^+}}{W_{dry}} \qquad (4)$$

where m_{H^+} expresses the quantity of sulfonic acid groups.

Calculation of surface initiator in silica-initiator particles from TGA data

We assume that m_{bs} (900 °C) = m_{si} (900 °C), where m_{bs} and m_{si} denote the masses of a single bare silica particle and a single silica-initiator particle at 900 °C in TGA analysis, respectively. Using the residue mass of the silica (or silica-initiator) as reference, the mass increase of silica-initiator to silica particles is calculated from equation 5:

$$\left[\left(1 - WR_{si}\right)/W \cdot R_{si} - \left(1 - WR_{bs}\right)/WR_{bs}\right] \times 100\% = 22.5\% \qquad (5)$$

Where WR_{bs} and WR_{si} are the weight retentions of bare silica particle (87.6 %) and silica-initiator particle (73.2 %) at 900 °C in TGA, respectively. Therefore, the mass of surface initiator on 62 mg silica-initiator particles is shown in equation 6:

$$22.5\% \times \left(62 \times WR_{si}\right) = 10.21 \text{ mg} \qquad (6)$$

The thermally decomposable moiety of the surface initiator (the hydrocarbon portion) has a molecular weight (M_w) of 320 g/mol. Thus, the calculated amount of surface initiator in 62 mg silica-initiator particles is $10.21/M_w$ = 0.03 mmol.

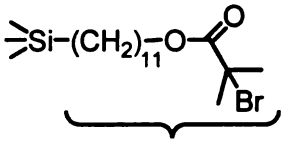

M_w = 320

Calculation of TGA weight retentions of particles isolated at different polymerization time

The calculation of the TGA weight retention of silica-PSSNa-1 particle isolated at 10.4% monomer conversion is illustrated. The weight retentions of silica-PSSNa-2 and silica-PSSNa-3 particles were calculated by the same method and the results are summarized in **Table 2**. In addition to m_{bs} (900 °C) = m_{si} (900 °C), we also assume that the weight retention of silica-PSSNa particles correspond to the residue of silica-initiator and the surface PSSNa. So m_{sp} (900 °C) = m_{si} (900 °C) + m_{pss} (900 °C), where m_{sp} and m_{pss} represent the masses of a single silica-PSSNa particle and PSSNa on a single silica-PSSNa particle at 900 °C in TGA analysis, respectively. **Figure 22** showed that the weight retention of linear PSSNa was 37.1 % at 900 °C, which would be used as a reference for surface PSSNa, and silica-initiator particles retained 73.2 % of its mass at 900 °C in TGA. So the TGA weight retention of silica-PSSNa-1 could be calculated from equation 7:

$$\frac{W_{si} \times 73.2\% + W_{mo} \times C_{onv} \times 37.1\%}{W_{si} + W_{mo} \times C_{onv}} \times 100\% \qquad (7)$$

Where W_{si} and W_{mo} represent the initial weights of silica-initiator particles and monomer charged in the surface polymerization, respectively, and C_{onv} stands for the monomer conversion. For the silica-PSSNa-1 particle, the experimental data are W_{si} = 62 mg, W_{mo} = 430 mg, and C_{onv} = 10.4 %. Therefore, the calculated TGA weight retention is 58.1 %, which is reasonably close to the actual data obtained from the TGA curve.

Chapter 3 Magnetic hybrid nanoparticles: Synthesis, Characterization, and Application in Fuel Cells

Introduction

Recently, there has been considerable interest in the development of fuel cells, especially hydrogen powered fuel cells, which cleanly convert the chemical energy of fuels directly into electric energy and heat with high efficiency. A key component of hydrogen based fuel cells is the proton exchange membrane (PEM), which transports protons from the anode to the cathode and separates fuel and oxidant. Nafion, the prototype PEM, has a high proton conductivity and chemical and mechanical stability at moderate temperatures in the harsh fuel cell environment. Although the actual morphology of hydrated Nafion is still under investigation, it's widely agreed that microphase-separation of Nafion's perfluorocarbon backbone and pendent fluorosulfonic acid groups accounts for its high proton conductivity.[4,14,15] The two domains of Nafion provide two critical properties: the hydrophilic domain supports efficient proton transport while the hydrophobic domain provides mechanical and chemical stability. Despite the high performance of Nafion in fuel cells, its high manufacturing cost, drastically reduced proton conductivity above 80 °C, environmental incompatibility, and severe methanol permeability limit its use in fuel cell applications.

Developing alternatives to Nafion is a major challenge in current fuel cell research. The usual design strategy for such membranes has been to synthesize sulfonated analogues of thermally stable polymers, such as sulfonated poly(arylene ether ether ketone),[14] sulfonated polyimides,[83] sulfonated

polysulfone,[123] and sulfonated polystyrene.[160] Membranes derived from these polymers have advantages over Nafion in terms of cost and reduced methanol cross-over, but in their hydrated state, they generally suffer from poor dimensional, chemical, and mechanical stability.[2,61,161,166,168] The problems associated with sulfonated polymers can be overcome by the use of polymer blends, which are comprised of a hydrophilic polyelectrolyte phase embedded in a non-conductive material for reinforcement.

Composite membranes made from the blending of a hydrophilic proton conductor and PVDF have been investigated in our group. The hydrophilic proton conductors were poly(4-styrenesulfonic acid)-coated silica nanoparticles, which were synthesized by the surface-initiated ATRP of sodium 4-styrenesulfonate from silica nanoparticles followed by acidification. The resulting composite membranes have comparable or better performance than Nafion 117 at the same testing conditions. However, the composite membrane system relied on the self-assembly of the hydrophilic nanoparticles in the hydrophobic PVDF matrix and there was no control over the alignment of particles in matrix material.

The distribution of proton conductors in membranes has a dramatic effect on the performance of membranes. Aligning polyelectrolytes along the proton transport direction could create conductive paths, which reduce the bulk membrane resistance and improve proton conductivity. Electric fields have been ued to align proton conducting polyelectrolytes while casting blend membranes.[101,180,208] The polyelectrolytes were aligned into long linear chains extending across the membranes. Membranes with aligned polyelectrolytes had

higher proton conductivities and less water uptake than membranes with unaligned polyelectrolytes

Although applied electric fields have successfully aligned polyelectrolytes while casting blend membranes, there are limitations to this technique. There must be sufficient dielectric contrast between polyelectrolyte and the matrix, and the matrix must sustain a high field and have sufficient mobility. These restrictions have hindered the broad application of this processing technique due to a limited choice of matrix materials. An alternative technique, using magnetic fields as the external driving force, is more suitable for polyelectrolyte alignment in blend membranes, as most polymers are anti-ferromagetic and hence are good matrix materials. Unlike electric fields, magnetic fields are not restricted in terms of the applied field strength, but only require that the polyelectrolytes have sufficient magnetization to respond to a magnetic field.

Recently, Shaw *et al.* ued a magnetic field to align proton conductive magnetic nanoparticles in sulfonated poly(ether ketone ketone) (SPEKK) during the membrane casting process.[181] Successful alignment of magnetic nanoparticles in SPEEK can be seen in aligned membranes, while randomly dispersed particles showed up in membranes without magnetic field processing. Not surprisingly, the conductivity of membranes with aligned particles was twice that of unaligned controls. However, the proton conductivity of the blend membrane was much lower than a standard SPEKK membrane, which was ascribed to the decreased IEC of the blend membrane.

While Shaw *et al.* showed that magnetic fields can be used to align magnetic nanoparticles in a SPEEK matrix, there are limitations to Shaw's approach. The γ-Fe_2O_3 particles were confined to the surfaces of composite particles instead of being encapsulated by the polymer, making γ-Fe_2O_3 particles vulnerable to the strong acidic environment of PEMs (γ-Fe_2O_3 particles dissolve in acid). Secondly, the magnetic particles were aligned in the plane of the membrane, while real PEMs require through-plane proton conducting paths. Finally, both the magnetic particles and the matrix (SPEEK) are hydrophilic, which would likely result in excessive swelling and low mechanical strength membranes.

Herein, we systematically investigated the synthesis and characterization of proton conducting magnetic nanoparticles, which were composed of magnetite as the core, silica as the middle layer, and poly(4-styrenesulfonic acid) as the polymer coating. The magnetite core enables magnetic alignment, the silica shields magnetite from the acidic environment of PEMs, and the poly(4-styrenesulfonic acid) coating supports proton conduction. "Magnetic" composite membranes were then fabricated from a blend of proton conducting magnetic nanoparticles and PVDF. During the solution casting of membranes, an external magnetic field was applied perpendicularly to the membrane surface to induce the alignment of nanoparticles in PVDF matrix across the membrane. The "magnetic" composite membranes approach may be more cost effective than the perfluorinated PEMs due to the much easier synthesis and simpler processing.

Results and discussion

Synthesis and characterization of magnetic nanoparticles

As displayed in **Scheme 6**, the desired magnetic nanoparticles were synthesized by two different strategies. After coating silica onto magnetite (MNT) particles to form MNT-silica nanoparticles, the particle surface was chemically functionalized with ATRP initiators, providing a macroinitiator (MNT-initiator). In the "post-sulfonation" approach, polystyrene was grown from the surface of the nanoparticles followed by sulfonation to obtain proton conducting magnetic nanoparticles (MNT-PSSH). The second strategy utilized the direct ATRP of sodium 4-styrenesulfonate from MNT-initiator nanoparticles to generate the salt form of proton conducting magnetic nanoparticles (MNT-PSSNa). The magnetic composite nanoparticles, MNT-PSSH, have the dual properties of magnetic susceptibility from the magnetic inorganic core and high proton conductivity from the poly(4-styrenesulfonic acid), anchored to the surface.

Scheme 6. Schematic illustration of two strategies for the synthesis of poly(4-styrene sulfonic acid)-coated magnetic nanoparticles.

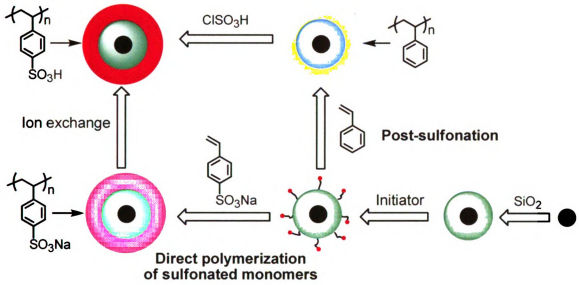

The MNT nanoparticles were synthesized according to a literature procedure.[209] $FeCl_3$ was hydrolyzed by water produced in situ from the reaction between sodium hydroxide and poly(acrylic acid) (PAA) generating $Fe(OH)_3$ (**Scheme 7**). $Fe(OH)_3$ was then reduced to $Fe(OH)_2$ in diethylene glycol (DEG) at 220 ºC, and converted to Fe_3O_4 by dehydration at high temperature. The MNT were stabilized by electrostatic interactions between the iron cations and the carboxylate anions of the polyacrylate surfactant, resulting in water soluble MNT nanoparticles.

Scheme 7. Schematic illustration of **(a)** synthesis of MNT nanopaticles; and **(b)** structure of PAA-capped MNT nanoparticles.

(a)

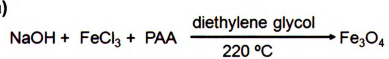

(b)

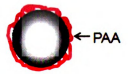

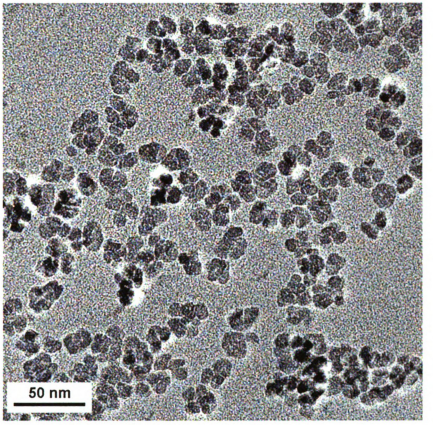

Figure 35. TEM image of MNT nanoparticles.

The high temperature hydrolysis reaction yielded monodisperse magnetite nanocrystals with an average diameter of 12 nm (**Figure 35**). In addition, the high temperature annealing during the reaction provided highly crystalline magnetite nanoparticles, which was confirmed by X-ray diffraction (XRD). The XRD powder pattern in **Figure 36** shows the characteristic 220, 311, 400, 422, 511, and 440 reflections for cubic Fe_3O_4.[209]

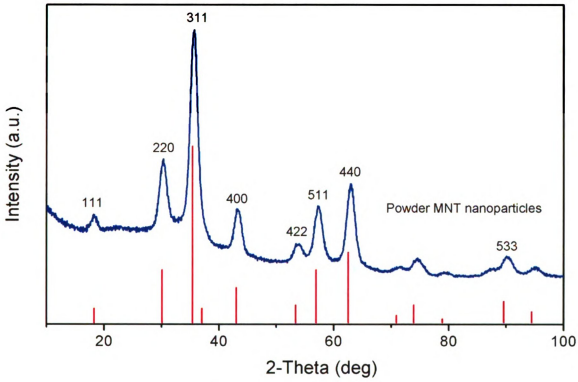

Figure 36. X-ray diffraction pattern of powder MNT nanoparticles. The vertical bars correspond to the reflections and their relative intensity as recorded in ASTM data cards for cubic Fe_3O_4.

The MNT nanoparticles were coated with silica to screen particle-particle dipolar attractions, prevent their aggregation, and shield the MNT nanoparticles from the acidic environment of PEMs. The surface coating was carried out in a basic ethanol/water mixture with the MNTs acting as the nucleation seeds.[210] This strategy provided easy control over the resulting particle (MNT-silica) size since the thickness of silica layer depends on the ratio of base:alcohol:water and the reaction time. The as-synthesized MNT-silica nanoparticles were water soluble due to surface silanol groups.

The size and morphology of MNT-silica nanoparticles were characterized by TEM (**Figure 37**). The monodisperse MNT-silica nanoparticles are spherical

and have an average diameter of 50 nm with very little aggregation. The MNT cores (dark color) are encapsulated by a ~20 nm thick silica layer. Some MNT-silica nanoparticles had a single MNT nanoparticle as its core, but others had multiple MNT cores, which might have resulted from the rapid growth of silica layer onto MNT nanoparticles, or that some particles are ferromagnetic rather than superparamagnetic.

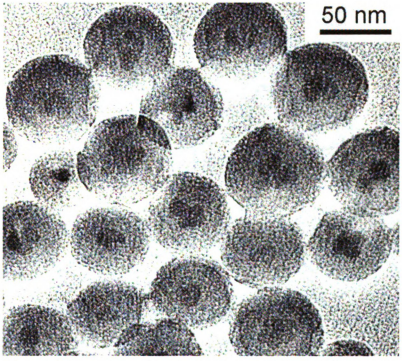

Figure 37. TEM image of MNT-silica nanoparticles.

Energy-filtered transmission electron microscopy (EFTEM) is an efficient analytical tool for obtaining the chemical composition of materials on the nanometer and even subnanometer length scale. In EFTEM, the elemental distributions are displayed as false color images. The images show that iron

(**Figure 38b**) only appears in the core while silicon (**Figure 38c**) is limited to the shell, which was in good agreement with the actual morphology shown in **Figure 38a**.

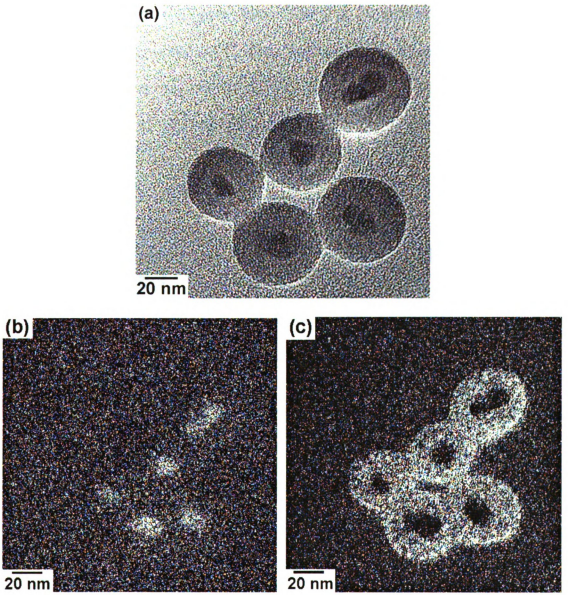

Figure 38. **(a)** TEM image of MNT-silica. **(b)** EFTEM iron map. **(c)** EFTEM silicon map.

The MNT-silica nanoparticles need to be superparamagnetic for their application in fuel cell membranes. Superparamagnetic materials have no net magnetism, but can be aligned in an external magnetic field. MNT-silica nanoparticles were water soluble and did not exhibit any evidence for ferromagnetic properties (**Figure 39a**). However, in presence of an external magnet, the well-dispersed MNT-silica nanoparticles were localized by the magnet demonstrating magnetic properties (**Figure 39b**). The response of MNT-silica nanoparticles to an external magnetic field is very useful for aligning particles.

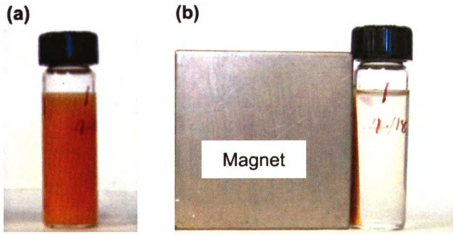

Figure 39. Photos of MNT-silica nanoparticles dispersed in water **(a)** without an external magnetic field (a fine dispersion of particles in water); and **(b)** with an external magnetic field (particles were localized toward the magnet).

The induced alignment of MNT-silica nanoparticles can be examined microscopically. A TEM sample was prepared by adding a drop of the dilute MNT-silica nanoparticle water dispersion to a TEM sample grid which was placed in an external magnetic field. As shown in **Figure 40**, the four images captured

from different positions on the TEM grid show particles aligned into chain-like structures along the magnetic field direction. The aggregation of MNT-silica nanoparticles is consistent with the attractive interaction between magnetic moments generated in response to the external magnetic field. This result suggests the possibility of using an external magnetic field to align proton-conducting magnetic particles while casting membranes.

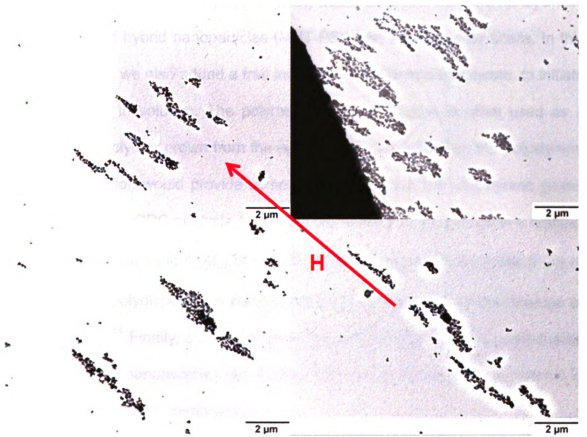

Figure 40. TEM images of chain-like structures formed by MNT-silica in response to an external magnetic field (~1 Tesla).

Synthesis of poly(4-styrenesulfonic acid)-coated magnetic hybrid nanoparticles (MNT-PSSH) by a "post-sulfonation" method

The silica shell of MNT-silica nanoparticles not only improves the chemical stability of MNT nanoparticles in acidic conditions, but also facilitates the introduction of surface functional groups through the reaction between surface silanols and various coupling agents. As illustrated in **Scheme 8**, organosilane initiators were chemically immobilized onto MNT-silica nanoparticle surfaces to generate sites for ATRP. Polystyrene (PSt) was then grown from the nanoparticle surface to yield hybrid nanoparticles (MNT-PSt) with thick polymer shells. In this polymerization, we also added a free initiator, ethyl 2-bromoisobutyrate, to initiate polymerization in solution. The polymer formed in solution is often used as a proxy for the polymer grown from the surface, and characterizing the polystyrene formed in solution would provide some information about the polystyrene grown from the surface. GPC analysis of polystyrene formed in solution gave a number average molecular weight (M_n) of 56,000 Da and a polydispersity index (PDI) of 1.08. The low polydispersity is comparable to ATRP reactions in the absence of nanoparticles.[211] Finally, sulfonation provided poly(4-styrenesulfonic acid)-coated magnetic hybrid nanoparticles (MNT-PSSH) for the proton conducting material in "magnetic" composite membranes.

Scheme 8. Synthesis of poly(4-styrenesulfonic acid)-coated magnetic hybrid nanoparticles.

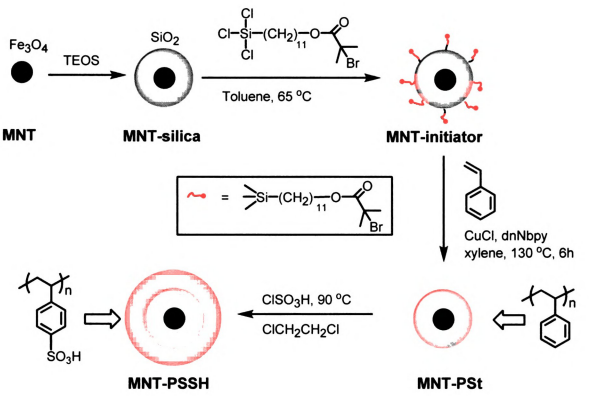

FT-IR was used to confirm each surface reaction (**Figure 41**). The MNT-silica nanoparticles have an absorption band at 1650 cm^{-1}, which was ascribed to the C=O bond from the surfactant (PAA) of Fe_3O_4 core. New bands at 3000 cm^{-1} to 2900 cm^{-1} (aliphatic C–H stretching) and 1750 cm^{-1} (C=O) in the spectrum of MNT-initiator confirmed the successful anchoring of the initiator to MNT-silica nanoparticles. After surface polymerization of styrene, the IR spectrum of the MNT-PSt nanoparticles was dominated by the characteristic bands of polystyrene: aromatic C–H stretching at 3100 cm^{-1} and 3000 cm^{-1}, aliphatic C–H stretching from the polymer backbone at 3000 cm^{-1} to 2900 cm^{-1}, and the overtones and combinations consistent with a mono-substituted benzene ring at

2000-1800 cm^{-1}. After sulfonation, the IR spectrum of MNT-PSSH shows strong O–H stretching modes from 3500 cm^{-1} to 2500 cm^{-1} due to water hydrogen-bonded to surface sulfonic acid groups. Bands for the sulfonic acid groups were partially obscured by a strong absorption band at 1050 to 1300 cm^{-1}, from SiO_2, but the S=O symmetric stretching mode at 1040 cm^{-1} is partially visible.

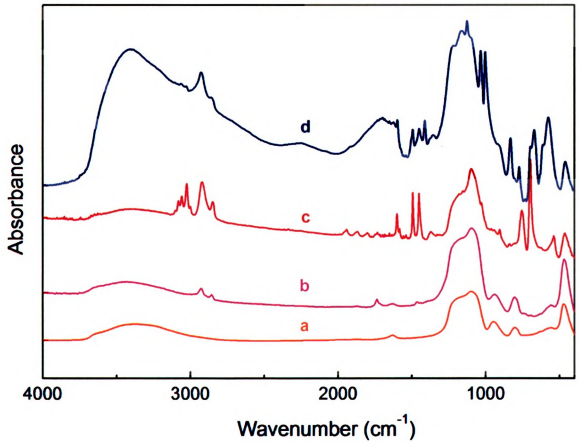

Figure 41. FT-IR spectra of **(a)** MNT-silica nanoparticles; **(b)** MNT-initiator nanoparticles; **(c)** MNT-PSt nanoparticles; and **(d)** MNT-PSSH nanoparticles. Samples were made into pellets with KBr.

Thermal gravimetric analysis (TGA) of the magnetic nanoparticles was used to establish the thermal stability of the polymer layer, and to estimate the surface functional group coverage for the nanoparticles (**Figure 42**). The

cumulative weight loss at 800 °C for MNT-silica particles was ~6 %, which is likely due to the loss of adsorbed water and condensation of surface silanol groups. The TGA trace for MNT-initiator particles shows an additional weight loss of ~10 %, from the degradation of surface initiators. After surface-initiated ATRP of styrene from MNT-initiator nanoparticles, the MNT-PSt particles showed a sharp weight loss at ~300 °C, characteristic of the depolymerization of polystyrene chains. The 86 % weight loss at 800 °C indicates a thick surface coating of PSt. The thermal degradation of MNT-PSSH nanoparticle shows two steps: the first, from 200 to 400 °C, is assigned to desulfonation, while the second, from 400 to 640 °C, is degradation of residual polystyrene.

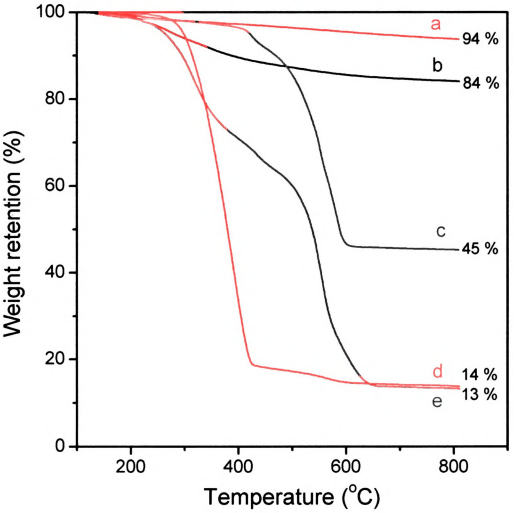

Figure 42. TGA analysis of **(a)** MNT-silica; **(b)** MNT-initiator; **(c)** MNT-PSSNa; **(d)** MNT-PSt; and **(e)** MNT-PSSH.

TEM analysis shows that surface-initiated ATRP yielded MNT-PSt nanoparticles with an average diameter of 150 nm (**Figure 43**). The nanoparticles were well-defined with a black core of Fe_3O_4, a grey middle layer due to silica, and a thick outer shell composed of polystyrene. The polymer shells have an average thickness of 50 nm and were uniform for all nanoparticles, which is consistent with controlled surface growth of polymer chains by ATRP.[211]

The morphology of the Fe_3O_4 and silica layer in MNT-PSt was unchanged from the image shown in **Figure 37** for MNT-silica nanoparticles.

Interestingly, the isolated MNT-PSt nanoparticles shown in **Figure 43a** also formed "coffee ring stain-like" aggregates (**Figure 43b**) due to the way the TEM sample was prepared. A drop of the toluene dispersion of MNT-PSt nanoparticles was dropped to the water surface, and a TEM grid submerged in water was slowly raised to capture nanoparticles. During solvent evaporation, toluene might have carried nanoparticles to solvent frontier, where the particles aggregated.

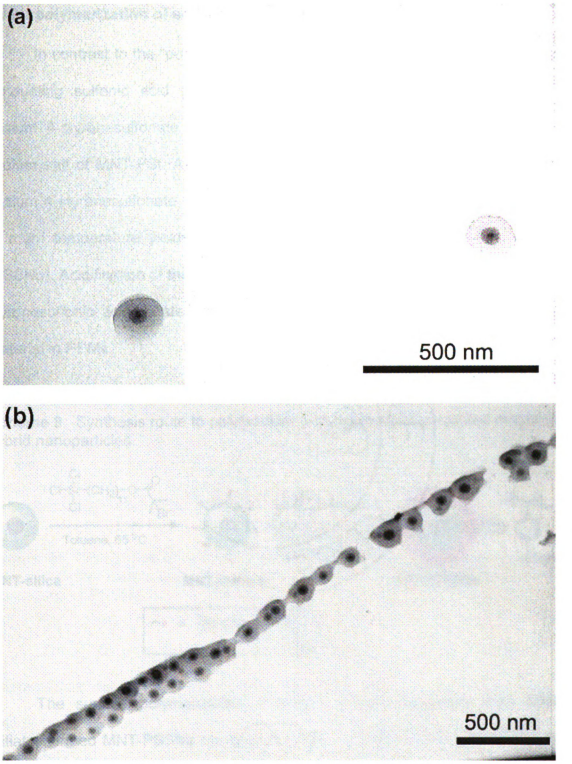

Figure 43. TEM image of **(a)** isolated MNT-PSt nanoparticles; and **(b)** "coffee ring stain"-like aggregated MNT-PSt nanoparticles.

Direct polymerization of sodium 4-styrenesulfonate

In contrast to the "post-sulfonation" approach, which introduces the proton conducting sulfonic acid groups after polymerization, the polymerization of sodium 4-styrenesulfonate from MNT-initiator surfaces directly generates the sodium salt of MNT-PSt. As illustrated in **Scheme 9**, surface-initiated ATRP of sodium 4-styrenesulfonate from MNT-initiator nanoparticles in aqueous solution at room temperature yields a dense shell of poly(sodium 4-styrenesulfonate) (PSSNa). Acidification of the hybrid MNT-PSSNa nanoparticles generates poly(4-styrenesulfonic acid) coated magnetic nanoparticles for the proton conducting material in PEMs.

Scheme 9. Synthesis route to poly(sodium 4-styrenesulfonate)-coated magnetic hybrid nanoparticles.

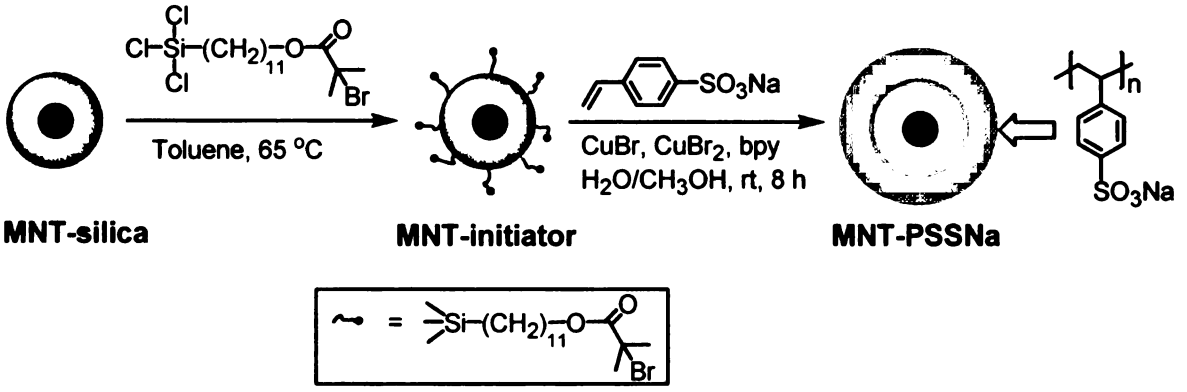

The surface polymerization of sodium 4-styrenesulfonate from MNT-initiator formed MNT-PSSNa nanoparticles with an average diameter of 100 nm (**Figure 44**). The morphology of Fe_3O_4 and silica layer in MNT-PSSNa was similar to the MNT-silica nanoparticles displayed in **Figure 37**. The hybrid silica-PSSNa nanoparticles have uniform polymer shells with an average thickness of

25 nm, which indicated that surface polymer chains were grown at comparable rates.

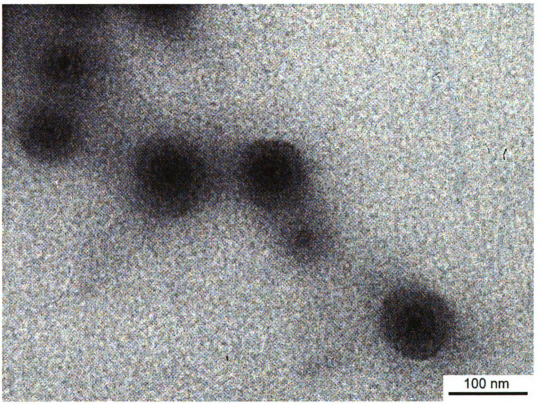

Figure 44. TEM image of MNT-PSSNa nanoparticles. Black spots are the Fe_3O_4 cores, the gray middle layer is the silica coating, and the light gray outer shell is composed of PSSNa.

The FT-IR spectrum of MNT-PSSNa nanoparticles was dominated by the characteristic peaks of PSSNa (**Figure 45**). The strong O–H stretching bands at 3435 cm^{-1} was due to water absorbed by the hygroscopic polyelectrolyte. Absorption peaks between 3100 cm^{-1} and 3000 cm^{-1} were assigned to aromatic C–H stretching, while bands from 3000 cm^{-1} to 2900 cm^{-1} resulted from aliphatic C–H stretching. In addition to the bands at high wavenumbers, the presence of

PSSNa was confirmed by the S=O asymmetric and symmetric stretching bands at 1200 and 1040 cm^{-1}, respectively.

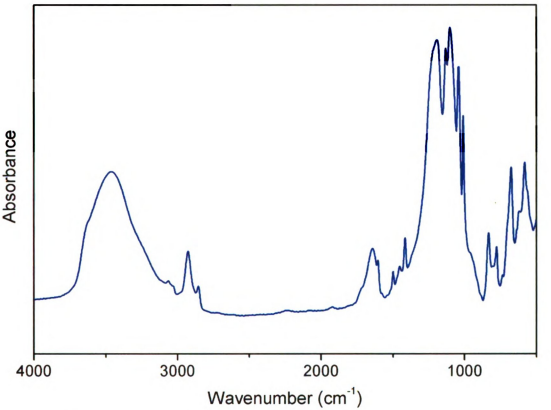

Figure 45. FT-IR spectrum of MNT-PSSNa nanoparticles. The sample was made into a pellet with KBr.

The TGA curve of MNT-PSSNa, as presented in **Figure 42c**, exhibited two major mass loss events, which we interpreted as the loss of sulfonate groups at approximately 400 °C, and degradation of the polymer backbones commencing at around 450 °C. It is noteworthy that PSSNa had a nonvolatile residue (likely Na_2O) at 800 °C in an oxidative atmosphere.[202] Thus, 45 % weight retention of MNT-PSSNa particles at 800 °C underestimates the amount of polymer on the hybrid nanoparticles. A comparison between the TGA traces of

MNT-PSSNa and MNT-PSSH particles suggests that the free acid was thermally less stable than the sodium salt in an oxidative atmosphere. The MNT-PSSNa nanoparticle had its first dramatic weight loss commencing at 400 °C while MNT-PSSH degraded much earlier at ~200 °C.

Fabrication and characterization of "magnetic" composite PEMs

The magnetic properties of different nanoparticles were tested with a vibrating sample magnetometer at room temperature. As shown in **Figure 46**, the nanoparticles had a strong magnetic response to a varying external magnetic field. The field-dependent magnetization plots (inset) indicated that the magnetic nanoparticles were slightly ferromagnetic with very small remanence (the magnetization that persists after an external magnetic field is removed) and coercivity (the intensity of an external magnetic field required to reduce the magnetization of that material to zero after the magnetization of the sample has been driven to saturation), which might be due to some ferromagnetic impurities. The saturation magnetization value of MNT-silica nanoparticles was 4.9 emu/g but decreased in polymer coated magnetic nanoparticles, primarily due to the nonmagnetic polymer shell since the units for magnetization are expressed as per gram of sample.[212]

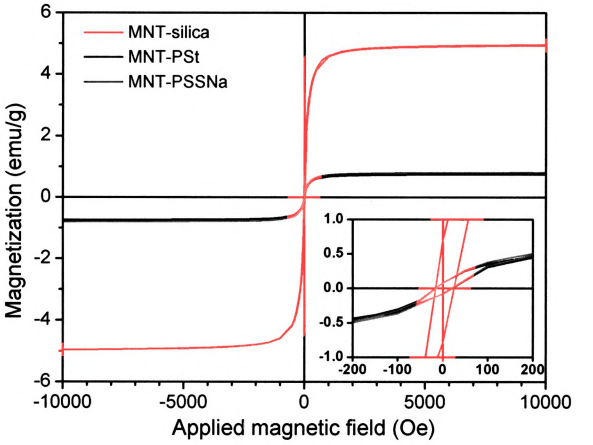

Figure 46. Room temperature hysteresis curves of magnetic nanoparticles. The inset demonstrated the data around zero field from -200 Oe to 200 Oe.

Generally, "magnetic" composite membranes were obtained by solution-casting a DMF mixture of MNT-PSSH hybrid particles and PVDF (**Figure 47**). Membranes with aligned MNT-PSSH nanoparticles were cast in the presence of an external magnet aligned perpendicularly to the membrane plane. The ~1 Tesla field was maintained until all solvent had evaporated to prevent randomization of nanoparticles upon removal of the external magnetic field. Membranes were light brown color, possibly due to the dark color of iron oxide (**Figure 47b**).

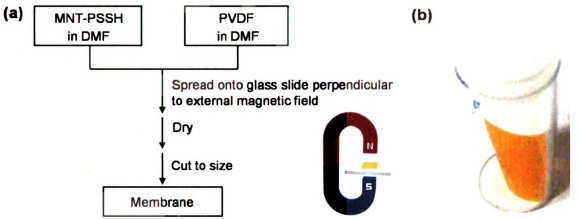

Figure 47. **(a)** Schematic illustration of composite proton exchange membrane fabrication. **(b)** Photo of a 2.5x2.5 cm^2 composite membrane with 30 wt% MNT-PSSH particles cast in presence of an external magnetic field.

The performance of membranes can be evaluated by their polarization curves. Generally, there are three divisions in a polarization curve: activation polarization, ohmic polarization, and concentration polarization. When the current is zero, the open circuit voltage is the cell voltage. When the current starts to flow, the voltage decreases owing to the activation polarization, after which the polarization curve becomes linear due to the ohmic polarization. This region is associated with the ohmic losses and its slope is correlated to the resistance of the membrane-electrode assembly. The polarization behavior of several composite membranes in fuel cells is displayed in **Figure 48**. The experiments were run under fully humidified conditions, with H_2 and O_2 as the fuel and oxidant, respectively. Nafion 117 and pure PVDF membranes were used as controls. Pure PVDF membranes (0 wt% MNT-PSSH nanoparticles) had little or no proton conductivity, which is not surprising since there was no conductive ionomers. The resistance of a membrane with 20 wt% particles was slightly higher than Nafion

117, but membranes with 30 wt% and 40 wt% particles performed better than Nafion 117 in the ohmic region, and the performance of these "magnetic" membranes increased with the MNT-PSSH content.

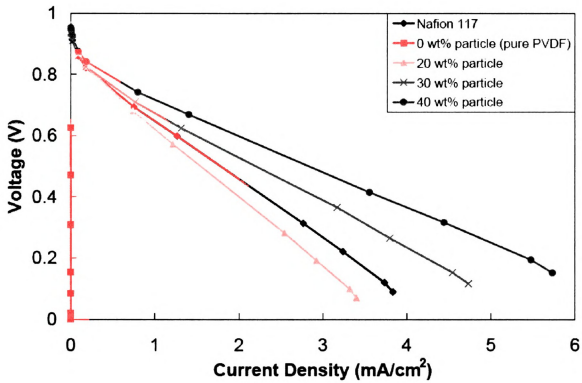

Figure 48. Polarization curves of composite membranes with different magnetic nanoparticle contents and Nafion 117 at room temperature.

Ideally, PEMs should have high proton conductivity and minor membrane swelling. Membrane dimensional stability was obtained by measuring the dimensional changes between the dry and water saturated states. Membranes that swell excessively can detach from the electrode surfaces as most electrodes do not swell, resulting in mechanical stress.[208] Nafion 117, equilibrated in water for 48 h, increased 18 % in length compared to the dry film.[15] The severe expansion of Nafion 117 explains its poor performances in direct methanol fuel

cells, as the permeability of Nafion to methanol is related to the high swelling of Nafion in water. However, all of the "magnetic" membranes swelled <3 %. The low water swelling behavior may be due to the rigid matrix of crystalline PVDF, which suppressed the water swelling of MNT-PSSH particles in hydrated membranes.

Cross-sections of a 30 wt% MNT-PSSH aligned membrane were studied by TEM (**Figure 49**). The dark area represents nanoparticles and the light regions are PVDF. The magnetic nanoparticles aligned into elongated domains within the PVDF matrix, presumably due to the application of an external magnetic field during the film casting process.

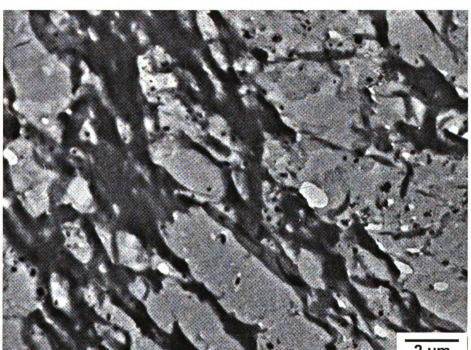

Figure 49. Cross-sectional TEM image of a 30 wt% MNT-PSSH aligned membrane.

Dispersive X-ray (EDX) line scanning was used to determine the elemental composition of the phases seen in the TEM images (**Figure 50a**). Fluorine, which is associated with the PVDF matrix, was found evenly along the scan line (**Figure 50b**). Sulfur, carbon, and oxygen, associated with the proton conducting MNT-PSSH nanoparticles, were concentrated in the dark area, which confirmed the phase-separated morphology of composite membranes. Nearly all of the dark regions are connected into a network of conducting channels, which likely contributed to the outstanding performance of the aligned composite membrane with 30 wt% MNT-PSSH particles shown in **Figure 48**.

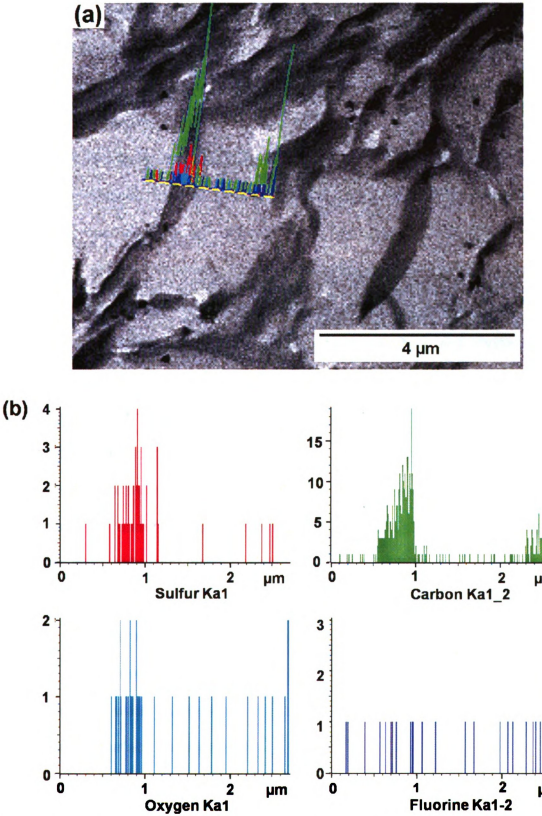

Figure 50. **(a)** Cross-sectional TEM image of aligned composite membrane with 30 wt% MNT-PSSH content. **(b)** EDX line-scan along the line displayed in **(a)**.

Conclusion

Proton conducting magnetic nanoparticles with a magnetite core, silica buffer layer, and a polyelectrolyte outer shell were synthesized by two different strategies, both of which utilized surface ATRP from the same macroinitiator. All synthesized magnetic nanoparticles had narrow size distributions. The uniform thickness of surface polymer shell in MNT-PSt and MNT-PSSNa nanoparticles implied the controlled "living" polymerization characteristics of surface ATRP. Applying an external magnetic field to MNT-silica nanoparticles aligned these nanoparticles in magnetic field direction.

Solution-casting the mixture of MNT-PSSH particles and PVDF formed "magnetic" composite proton exchange membranes, which were associated with advantages including low cost, and easy design, synthesis, and processing compared to perfluorinated PEMs. In the polarization experiments, "magnetic" composite membranes with 30 and 40 wt% particles revealed better performance than Nafion 117 under the same testing conditions. The magnetic nanoparticles in aligned composite membranes were noted to form chain-like aggregates in PVDF matrix leading to a phase-separated morphology.

In addition to proton exchange membrane, the polyelectrolyte coated magnetic hybrid nanoparticles might find applications in other areas, like ion exchange resin, water purification, and biology due to the versatile properties of magnetite and surface polyelectrolytes.

Experimental Section

Materials

Styrene, sodium 4-styrenesulfonate, CuBr (99.999%), $CuBr_2$ (99.999%), PVDF (M_w = 534,000 Da), 2, 2'-dipyridyl (bpy, 99+ %), 4,4'-dinonyl-2,2'-dipyridyl (dnNbpy), and Nafion 117 were obtained from Sigma-Aldrich. Poly(acrylic acid) (PAA, M_w = 2,000 Da) was purchased from Monomer-Polymer & Dajac Labs. Styrene was purified by passing through activated basic alumina column followed by distillation and bpy was sublimed prior to use. Toluene and tetrahydrofuran (THF) were distilled over sodium and benzophenone. Dimethylformamide (DMF) was dried over activated 4Å molecular sieves. The disodium salt of N,N,N',N'-ethylenediaminetetraacetic acid (EDTA·2Na) and diethylene glycol (DEG) were purchased from Spectrum and Fisher Scientific, respectively. All other chemicals and solvents were ACS reagent grade and used as received from commercial suppliers without further purification unless otherwise specified.

Characterization

IR spectra were acquired from a Mattson Galaxy 300 spectrometer purged with dry nitrogen, with the signal averaging 128 scans at a resolution of 4 cm^{-1}. All IR samples were dried, mixed with KBr, ground, and then pressed into pellets. Thermogravimetric analyses (TGA) were carried out in air on Perkin-Elmer TGA 7 instruments at a heating rate of 10 °C/min. TGA samples were dried under vacuum at 80 °C overnight prior to use. Dried samples were held at 120 °C in the TGA apparatus for 30 min prior to initiating the run.

The crystallographic study of the synthesized magnetite powder was performed on a Rigaku X-ray diffractometer using Cu Kα radiation at room temperature. The magnetic properties of different magnetic nanoparticles were studied at room temperature with a Quantum Design magnetic property measurement system (MPMS), which utilized a superconducting quantum interference device (SQUID) magnetometer.

The microstructure of particles and composite membranes were imaged using either a JEOL-100CX or a JEOL-2200FS transmittance electron microscope. To prepare TEM samples for MNT and MNT-PSSNa nanoparticles, their dilute water solutions were drop-casted onto carbon-coated copper mesh grids followed by solvent evaporation in air. For MNT-PSSH, a toluene solution of particles was dropped onto Milli-Q water, and as the toluene spread, it carried nanoparticles on water surface. A TEM grid submersed in water was slowly moved up to water surface to "fish" the nanoparticles. To prepare TEM sample of membrane cross-sections, membranes were processed as follows: dried under vacuum at 80 °C overnight, embedded in epoxy resin, dried at 50 °C for 24 h, and finally sectioned with an ultramicrotome to generate ~100 nm thick slices. The slices were picked up with copper grids for TEM analysis.

Polymer molecular weights were acquired with gel permeation chromatography (GPC). This characterization was done at 35 °C using two PLgel 10mixed-B columns in series with THF as the eluting solvent at a flow rate of 1 mL/min and a Waters 2410 differential refractometer as the detector. Mono-disperse polystyrene standards were used to calibrate the molecular weights.

The absolute polymer molecular weights could be calculated using an Optilab rEX (Wyatt Technology Co.) and a DAWN EOS 18 angle light scattering detector (Wyatt Technology Co.) with a laser wavelength of 684 nm.

Synthesis of magnetite (MNT, Fe_3O_4) nanoparticles

The magnetite nanoparticles were synthesized according to the procedure of Yin's work with some modifications.[209] A solution of NaOH (2 g, 50 mmol) and 20 mL of DEG was heated at 120 °C for 1 h under a nitrogen purge, and then was cooled to 70 °C with stirring until the solution turned to dark red so the dissolution of NaOH in DEG was complete. To a 50 mL 3-neck round bottom flask, were added poly(acrylic acid) (0.432 g, 6 mmol acrylic acid repeating units), $FeCl_3$ (0.488 g, 3 mmol), and 22.5 mL of DEG. The mixture was heated at 220 °C under nitrogen for 30 min with mechanic stirring, and then 6 mL of NaOH/DEG stock solution was quickly added. The mixture rapidly turned black, and was kept at 220 °C for another 20 min before slowly cooling to room temperature. The particles were collected with the help of a permanent magnet and after adding nitrogen-purged ethanol, they were re-dispersed in 0.5 mL of nitrogen-purged Milli-Q water. This washing process was repeated for three times to remove excess reactant and especially physisorbed poly(acrylic acid). The Milli-Q water and ethanol must be purged by nitrogen for at least 30 min prior to use and the washing process must be finished very quickly to prevent further air oxidation of the magnetic particles. Finally, the magnetite nanoparticles (MNT) were made into 0.5 wt% dispersion by dispersing in 45 mL of Milli-Q water.

Coating MNT nanoparticles with silica to synthesize MNT-silica

Using the method described by Deng *et al.* with some modification, silica-coated magnetic nanoparticles were prepared in basic alcohol/water mixture at room temperature with MNT as nucleation seeds.[210] To 11 mL water suspension of MNT, were added 110 mL of Milli-Q water, 480 mL of ethanol, and 10 mL of ammonia solution. After ultrasonication for 15 min, the mixture was vigorously stirred. Then, 2 mL of tetraethyl orthosilicate (TEOS) was added to the dispersion and the mixture was stirred at room temperature for 2 h forming silica coating on the surface of MNT nanoparticles. A solution of 2 M HCl was then added dropwise to flocculate the fine dispersion. The resulting particles (MNT-silica) were then collected with a permanent magnet and washed with ethanol and water six times until the supernatant was neutral. Finally, the MNT-silica nanoparticles were dried under vacuum at 80 °C overnight.

Immobilization of organosilane initiator onto MNT-silica to make MNT-intiator

Dry MNT-silica nanoparticles (0.2 g) were dispersed in 60 mL of dry toluene by ultrasonication. Using a syringe, 0.1 mL of freshly synthesized initiator, (11-(2-bromo-2-methyl)propionyloxy)undecyltrichlorosilane,[196] was added to the particles, and the reaction mixture was stirred under a N_2 atmosphere at 65 °C overnight. The resulting initiator immobilized magnetic nanoparticles (MNT-initiator) were collected with a permanent magnet, washed with dry THF six times, and dried under vacuum at 80 °C overnight.

Surface ATRP of styrene from MNT-initiator to make MNT-PSt

A 10 mL Schlenk flask was charged with styrene (2.7 mL, 23.3 mmol), MNT-initiator (0.05 g), ethyl 2-bromoisobutyrate (3.4 μL, 0.023 mmol), 4,4'-dinonyl-2,2'-dipyridyl (dnNbpy) (0.29 g, 0.714 mmol), and 1.1 mL of xylenes. After four freeze-pump-thaw cycles, the flask was backfilled with nitrogen and CuCl (23.3 mg, 0.238 mmol) was added. The mixture was treated with another three freeze-pump-thaw cycles and then stirred at 130 °C for 6 h in a nitrogen atmosphere. After quickly cooling down to room temperature in air, the polymerization system was diluted with 20 mL of THF and the magnetic particles were collected with a magnet. The supernatant containing linear polystyrene was condensed and precipitated from methanol to yield the polystyrene homopolymer. The isolated magnetic particles were washed by redispersing in THF and then being collected with a magnet. This washing process was repeated three times to fully remove linear polystyrene formed in solution. Finally, polystyrene and the magnetic nanoparticles (MNT-PSt) were dried under vacuum at 80 °C overnight, respectively.

Sulfonation of MNT-PSt to make MNT-PSSH nanoparticles

The sulfonation reaction was carried out by adding 0.05 mL of chlorosulfonic acid to a refluxing dispersion of MNT-PS nanoparticles (0.1 g) in 50 mL of 1,2-dichloroethane. Dark brown precipitate immediately formed from the homogeneous dispersion. The precipitate was washed with THF, being careful to remove physisorbed acid, and finally dried under vacuum at 80 °C overnight.

Surface ATRP of sodium 4-styrenesulfonate from MNT-initiator surface to synthesize MNT-PSSNa

In this surface-initiated ATRP reaction of sodium 4-styrenesulfonate, $CuBr/CuBr_2$ and bpy were applied as the catalytic system. Sodium 4-styrenesulfonate (0.43 g, 2.09 mmol), MNT-initiator nanoparticles (62 mg), $CuBr_2$ (1.4 mg, 0.006 mmol), bpy (28 mg, 0.18mmol), Milli-Q water (3 mL), and methanol (1 mL) were added to a 10 mL Schlenk flask equipped with a magnetic stirrer. Particles were dispersed in the reaction mixture by ultrasonication for 10 min. After four freeze-pump-thaw cycles, the Schlenk flask was backfilled with nitrogen and CuBr (8.6 mg, 0.06 mmol) was added. The polymerization was carried out in a nitrogen atmosphere at room temperature for 8 h. The as-synthesized magnetic nanoparticles were collected with a permanent magnet and then washed with Milli-Q water for further purification. Finally, the magnetic nanoparticles (MNT-PSSH) were dried under vacuum at 80 °C overnight.

Fabrication of "magnetic" composite membranes

Composite membranes were fabricated by the solvent-casting method. This procedure describes the preparation of 40 mg membranes. Predetermined amounts of PVDF and MNT-PSSH nanoparticles were dissolved in DMF in separate vials. Each solution was fixed at 0.05 g/mL, and the total mass of the particles and PVDF was 40 mg. The two solutions were combined and stirred until the system was homogeneous. Membranes were solution-cast by pouring the mixture onto a clean glass plate at 50 °C, typically covering 4x4 cm^2 area, with an external magnetic field applied perpendicularly to the glass slide surface

until all solvent evaporated. After 1 hour, the membrane had turned translucent, and the glass plate was transferred to a vacuum at 50 °C for further drying overnight. The dried membranes (15-35 μm thick) were then removed from the substrate by immersing the plate in water. The as-synthesized membranes were stored in Milli-Q water prior to tests.

Dimensional stability

Membranes were saturated in Milli-Q water for two days at room temperature prior to measuring the dimensions of swollen membranes. After drying under vacuum at 50 °C overnight, the dimensions of the dried membrane were measured. The swelling ratio was calculated from the length (longest dimension) of the membrane, as shown in equation 1:

$$\text{Swelling ratio} = \frac{l_{\text{wet}} - l_{\text{dry}}}{l_{\text{dry}}} \times 100\% \qquad (1)$$

where l_{wet} and l_{dry} represent the lengths of wet and dried membranes, respectively. The uncertainty in the measurement is <3%.

Chapter 4 Sulfonated Polyimide and PVDF based Blend Proton Exchange Membranes for Application in Fuel Cells

Introduction

Recently, there has been considerable interest in the development of fuel cells, especially hydrogen powered fuel cells, which cleanly convert the chemical energy of fuels directly into electric energy and heat with high efficiency. A key component of hydrogen based fuel cells is the proton exchange membrane (PEM), which transports protons from the anode to the cathode and separates fuel and oxidant. Nafion, the prototype PEM, has a high proton conductivity and chemical and mechanical stability at moderate temperatures in the harsh fuel cell environment. Although the actual morphology of hydrated Nafion is still under investigation, it's widely agreed that microphase-separation of Nafion's perfluorocarbon backbone and pendent perfluorosulfonic acid groups accounts for its high proton conductivity.[4,14,15] The two domains of Nafion provide separate properties: the hydrophilic domain supports efficient proton transport while the hydrophobic domain provides mechanical and chemical stability. Despite the high performance of Nafion in fuel cells, its high manufacturing cost, drastically reduced proton conductivity above 80 °C, environmental incompatibility, and severe methanol permeability limit its use in fuel cell applications.

Developing alternatives to Nafion, and especially those that can operate at high temperatures, is a major challenge in current fuel cell research. The usual design strategy for such membranes has been to synthesize sulfonated analogues of thermally stable polymers, such as sulfonated poly(arylene ether

ether ketone),[14] sulfonated polyimides,[83] sulfonated polysulfone,[123] and sulfonated polystyrene[160]. Membranes derived from these polymers have advantages over Nafion in terms of cost and reduced methanol cross-over, but in their hydrated state, they generally suffer from poor dimensional, chemical, and mechanical stability.[2,61,161,166,168] The problems associated with sulfonated polymers can be overcome by the use of polymer blends, which are comprised of a hydrophilic polyelectrolyte phase embedded in a non-conductive material for reinforcement.

The two components of a blend membrane provide complementary functions, with the polyelectrolyte providing proton conductivity while a second polymer affords mechanical integrity. In addition, blending usually involves commercially available polymers or inexpensive polymer precursors and thus blending is a simple and cost-effective route to produce PEMs. More importantly, the blending approach eliminates the need to optimize the mechanical, chemical and physical properties in a single polymer chain and it has the potential to develop a wide variety of PEMs.

The blend morphology is crucial since the conducting phase must be continuous for meaningful proton conductivity. Nafion's high proton conductivity has been ascribed to the development of a continuous channel morphology when hydrated, and analogous bicontinuous blends should also exhibit high proton conductivities. The selection of appropriate hydrophilic and hydrophobic blending materials must consider the interactions between the two blending

components,[170] in order to form continuous conducting channels and high proton conductivities analogous to Nafion.[157]

The naphthalenic sulfonated polyimides (SPIs) are a widely studied polyelectrolyte system due to their excellent thermal, chemical, and mechanical stability, high proton conductivity, good film-forming ability, and low gas permeability.[1,82,83,114,149,157,158] However, SPIs also tend to swell extensively. Poly(vinylidene fluoride) (PVDF) is an excellent candidate for the hydrophobic host in blend membranes; PVDF is commercially available, chemically and mechanically stable, and can be easily processed into membranes.[49,108,171-173] In addition, PVDF based membranes have reduced methanol permeability and swelling ratios, and exhibit good performance in direct methanol fuel cells (DMFC).[108,213]

Herein, we describe blend membranes derived from SPI and PVDF. The SPI was synthesized by direct polymerization of nathphalenic dianhydride and sulfonated diamine monomers. With its high degree of sulfonation, SPI has excellent proton conductivity, while the rigid PVDF matrix, incompatible with SPI, provides excellent mechanical and dimensional integrity. In addition, micro-phase separation of the two incompatible materials generates proton conducting channels comprised of SPI aggregates, and enhances proton conductivity.

Results and discussion

Synthesis and characterization of sulfonated polyimide (SPI)

The sulfonated polyimide homopolymer was synthesized by step growth polymerization as illustrated in **Scheme 10**.[214] 4,4'-Diaminobiphenyl 2,2'-

disulfonic acid (BDSA) was firstly converted to its triethylammonium salt, and then benzoic acid was introduced as the catalyst for the polycondensation of 1,4,5,8-naphthalene tetracarboxylic dianhydride (NTDA) and BDSA in *m*-cresol at 180 °C. The high reaction temperature helps remove water from the system and drive the reaction toward polymer formation, which ensured the synthesis of high molecular weight SPI. Furthermore, under the reaction conditions, polymer growth (amide formation) and imidization occurred spontaneously. The as-synthesized SPI in its triethylammonium salt form was a hard and tough solid and was difficult to grind, implying a high polymer molecular weight. Using the sulfonated diamine monomer avoided the drawbacks associated with "post-sulfonation" method, which usually results in low sulfonation degrees, cross-linking, and polymer chain degradation.[2]

Scheme 10. Synthesis of sulfonated polyimide (SPI).

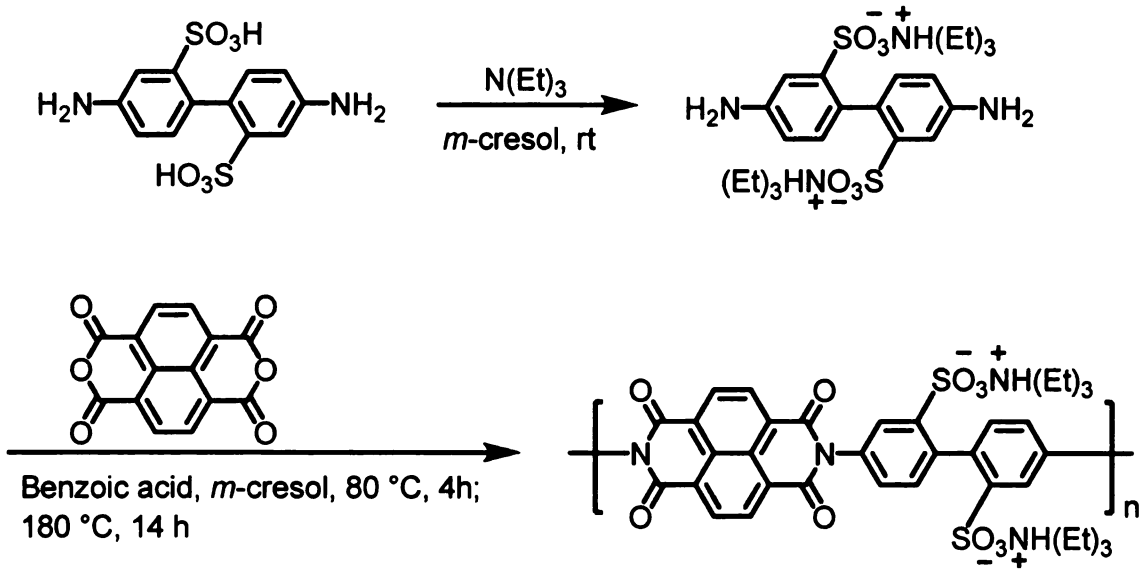

The chemical structure of the SPI triethylammonium salt was confirmed by ^{1}H NMR spectroscopy (**Figure 51a**). Proton peaks from the ethyl groups at ~1.1 and 3.0 ppm confirm the presence of the triethylammonium moiety in the polymer. Genies and others[158,214] assigned peaks at 8.7-8.8 ppm to the naphthalenic and ammonium protons, while the peaks at 7.35, 7.8, and 8.0 ppm were attributed to phenylene protons in the BDSA polymer segments. While our spectra showed comparable data, we found that the peaks were broadened, and the peak areas for the resonances at 8.9 ppm, and 8.0 ppm were significantly larger than the peaks at 7.35 and 7.8 ppm. The broadening of the NMR resonances is consistent with a rigid, high molecular weight polymer.

The diminution of the peaks at 7.35 and 7.8 ppm suggests that they are related to the polymer end groups, and that our material may have a higher molecular weight. Usually, the starting materials for polycondensation reactions are dried, but reagents and solvents are often used as received,[158,214] In our SPI syntheses, we dried or distilled all starting materials (BDSA and NTDA), reagents (benzoic acid and triethyl amine), and solvent (*m*-cresol) prior to the polycondensation reaction in order to obtain high molecular weight. We surmised that trace amounts of water in reagents and/or solvents limit the molecular weight, and to confirm this assumption, we carried out the polycondensation of dried BDSA and NTDA, but used reagents and solvents as received. As shown in **Figure 51b**, the ^{1}H NMR spectrum of the as-synthesized SPI is consistent with that reported in the literature.[158,214]

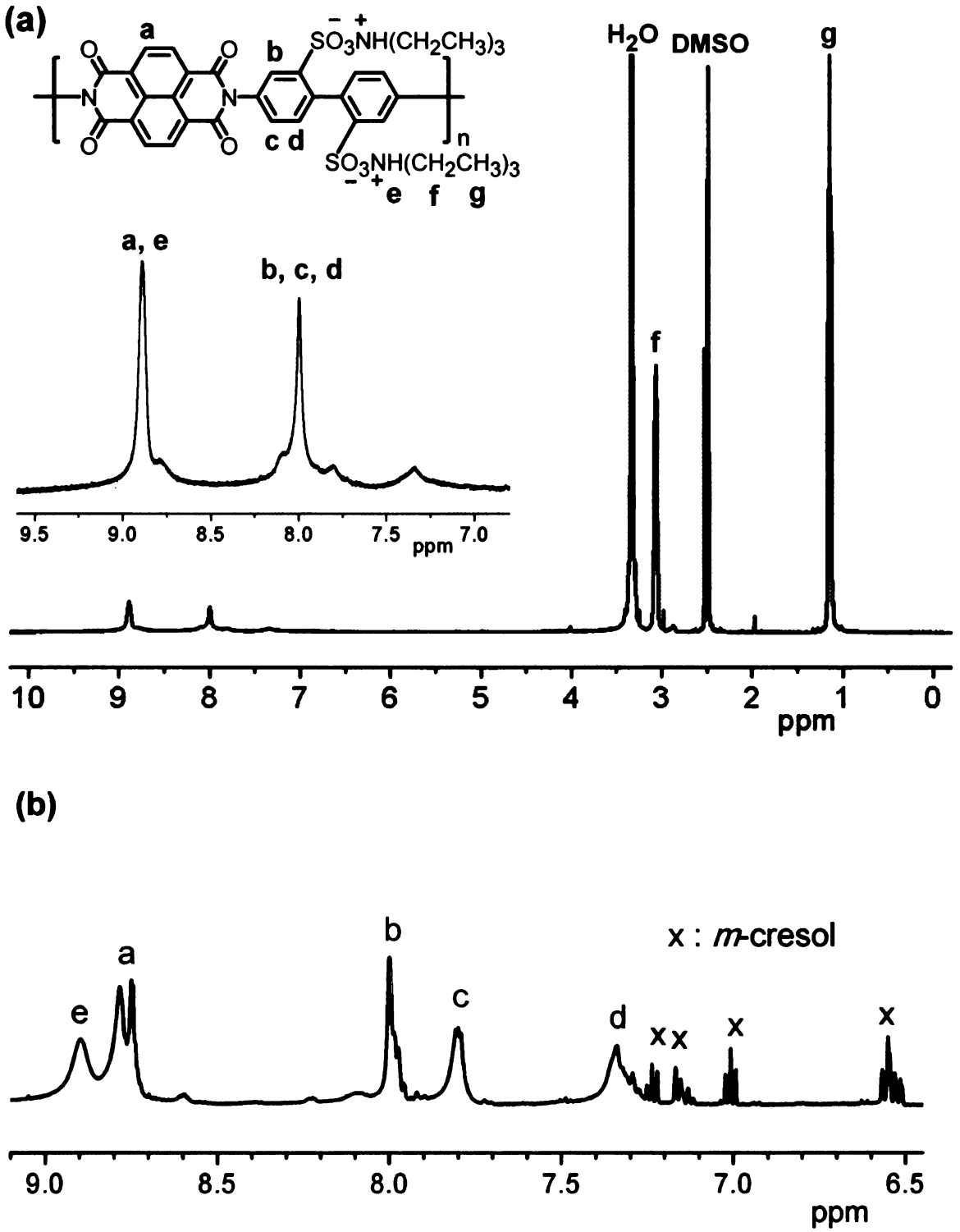

Figure 51. 500 MHz ^{1}H NMR spectra of the triethylammonium salt form of SPI synthesized with **(a)** dried starting materials, reagents, and solvents; and **(b)** dried starting materials, but reagents and solvents used as received.

FT-IR spectroscopy confirms the triethylammonium salt form of SPI (**Figure 52**). The spectrum shows strong, broad, O–H stretching bands at 3435 cm^{-1} due to water absorbed by the hygroscopic polymer. Bands between 3200 cm^{-1} and 3000 cm^{-1} were assigned to aromatic C–H stretching while bands from 3000 cm^{-1} to 2900 cm^{-1} resulted from aliphatic C–H stretching of the triethylammonium moiety. The characteristic C=O symmetric and antisymmetric stretching bands at 1718 cm^{-1} and 1680 cm^{-1}, and the C–N–C bending mode at 1345 cm^{-1} confirmed the presence of the naphthalenic imide. In addition to the characteristic peaks at high wavenumbers, the SPI structure was supported by the S=O antisymmetric and S=O symmetric stretching bands at 1185 cm^{-1} and 1035 cm^{-1}, respectively. The absence of the characteristic peak at 1780 cm^{-1} for a polyamic acid indicates a high degree of imidization.

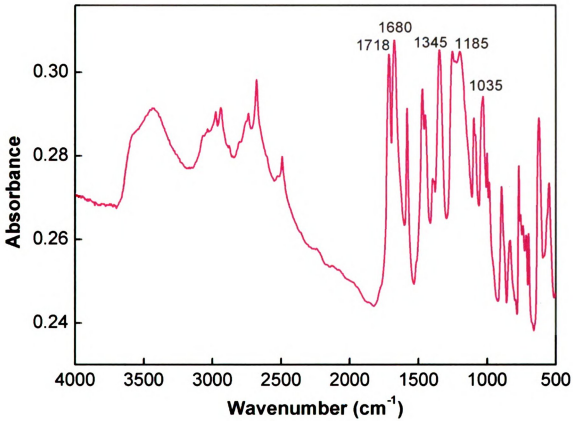

Figure 52. FTIR spectrum of SPI in its triethylammonium salt form. The sample was made into a pellet with KBr.

Thermogravimetric analysis (TGA) was performed to investigate the thermal stability of SPI in its triethylammonium salt form. As presented in **Figure 53**, there are two major weight loss events. The first weight loss (~30 %) commenced at ~200 °C and continued to 400 °C, which is likely due to desulfonation.[214] The weight loss observed above 400 °C corresponds to the oxidative degradation of the aromatic backbone of the polymer. The onset for weight loss is at ~200 °C, which demonstrates that the thermal stability of the SPI polymer is suitable for high temperature PEM applications.

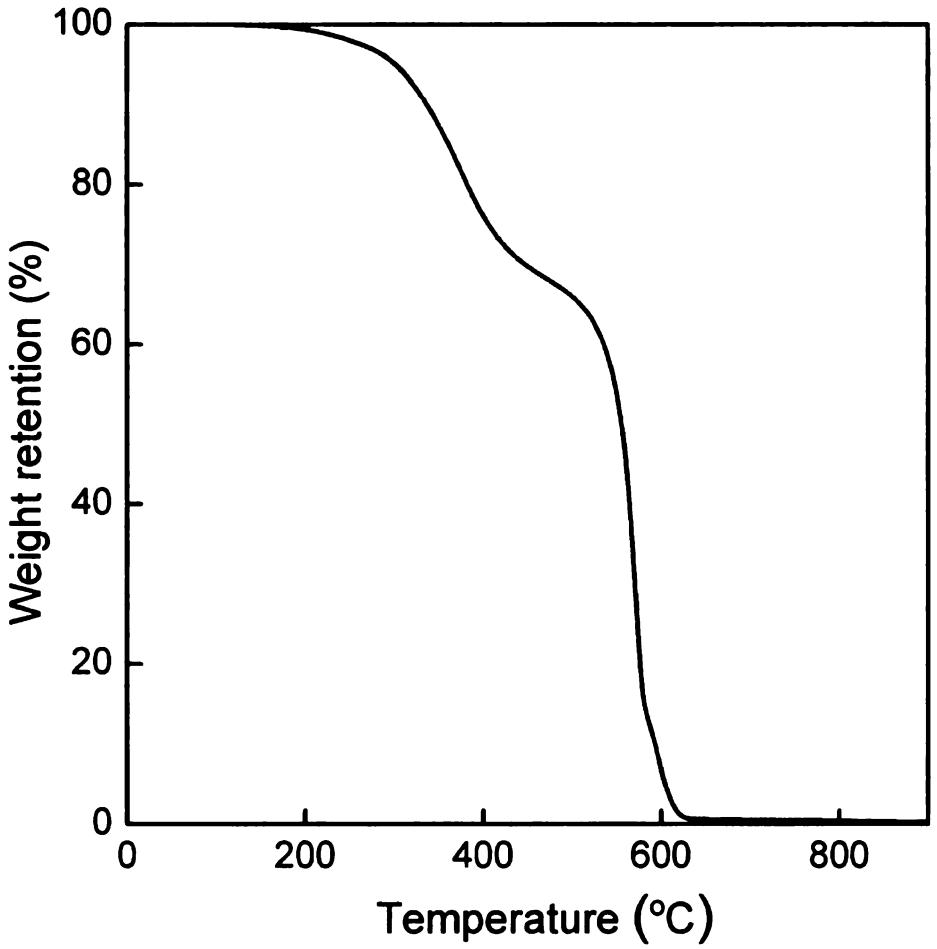

Figure 53. Thermogravimetric analysis of SPI (triethylammonium salt), run at a heating rate of 10 °C/min in air.

Fabrication and characterization of PEMs from the blending of SPI (triethylammonium salt) and PVDF

The triethylammonium salt of SPI was soluble in aprotic solvents (NMP and DMSO) and *m*-cresol. Blend membranes were obtained by solution-casting a DMSO mixture of the SPI (triethylammonium salt) and PVDF onto flat glass surfaces. Once soaked in water, the dried membrane samples were easily peeled from the glass substrate, and after acidification, the membranes were tough and yellow. **Table 3** summarizes the composition and experimental results from the blend membranes.

Table 3. Summary of SPI/PVDF membrane characteristics.

PEMs (SPI wt%)	IEC (meq/g)	Conductivity at rt (mS/cm)	Swelling ratio (%)	Water uptake (wt%)
0	0 [a]	0	<3	0
10	0.26 [a]	0	<3	2
20	0.51 [a]	0	<3	6
30	0.77 [a]	7	<3	11
40	1.03 [a]	41	<3	25
50	1.29 [a]	75	<3	47
Nafion 117 [b]	0.91[15]	62	18[15]	21

[a] IEC values were calculated from the SPI repeating unit (M_n = 778 g/mol) and the composition of blend membranes.
[b] Nafion 117 was included for comparison.

A key parameter of PEMs is water absorption. Membranes require water to dissociate SO_3H groups and act as "vehicles" to transport protons from the anode to the cathode; however, too much water usually results in severe swelling and poor mechanical strength. Ideally, the water uptake facilitates high proton conductivity without sacrificing a membrane's mechanical properties. As shown in **Figure 54**, water uptake by SPI blends increased linearly up to about 28 wt% SPI content. However, beyond 30 wt% SPI, water uptake increased drastically, indicating a change in the membrane morphology.[215] Since PVDF is hydrophobic, the SPI phase is primarily responsible for water absorption. When the SPI content in blend membranes is low, most sulfonic acid groups are isolated in

ionic clusters distributed throughout the continuous PVDF matrix, and water may be accessible to only few clusters. As the SPI content increases, accessible ionic clusters either increase in size or link to adjacent clusters, increasing the measured water uptake. When the SPI content in blend membranes exceeded ~30 wt%, the membrane morphology of isolated ionic clusters in PVDF transformed to a bicontinuous network of water swollen channels in a PVDF matrix. Above the apparent percolation threshold, water uptake increased linearly, but at a higher rate. Not surprisingly, a pure PVDF membrane (0 wt% SPI) had zero water absorption.

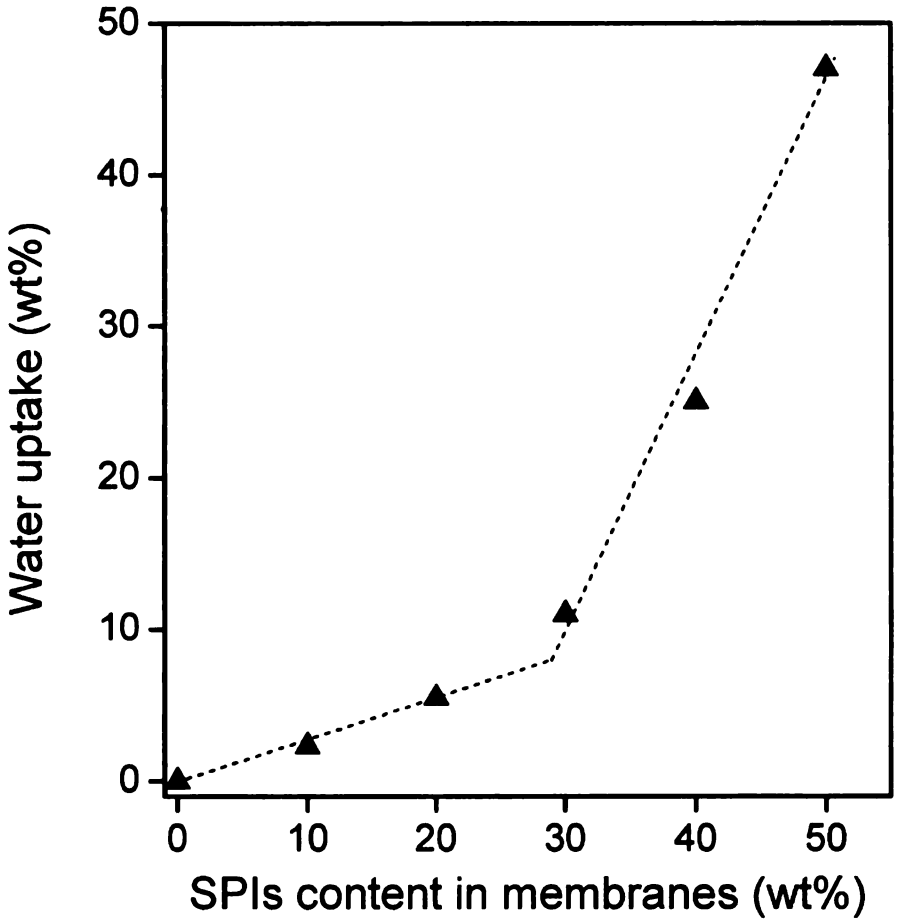

Figure 54. Water uptakes of blend membrane as a function of the SPI content. The membrane water uptake was measured gravimetrically at room temperature. (The dotted line is a guide to the eye)

The ion exchange capacity (IEC), expressed as mmol acid/g of sample, defines the number of charge carriers in a membrane and is directly correlated to a membrane's ability to absorb and retain water. As demonstrated in **Figure 55**, the water uptake is linearly correlated with the IEC values of the membranes up to about 0.78 meq/g (~28 wt% SPI). However, beyond this value, water uptake increased more rapidly, indicating a change in the membrane morphology. This sharp increase in water uptake is consistent with a percolation phenomenon

where isolated hydrophilic domains transform to a continuous network in the PVDF matrix.[50,206,215]

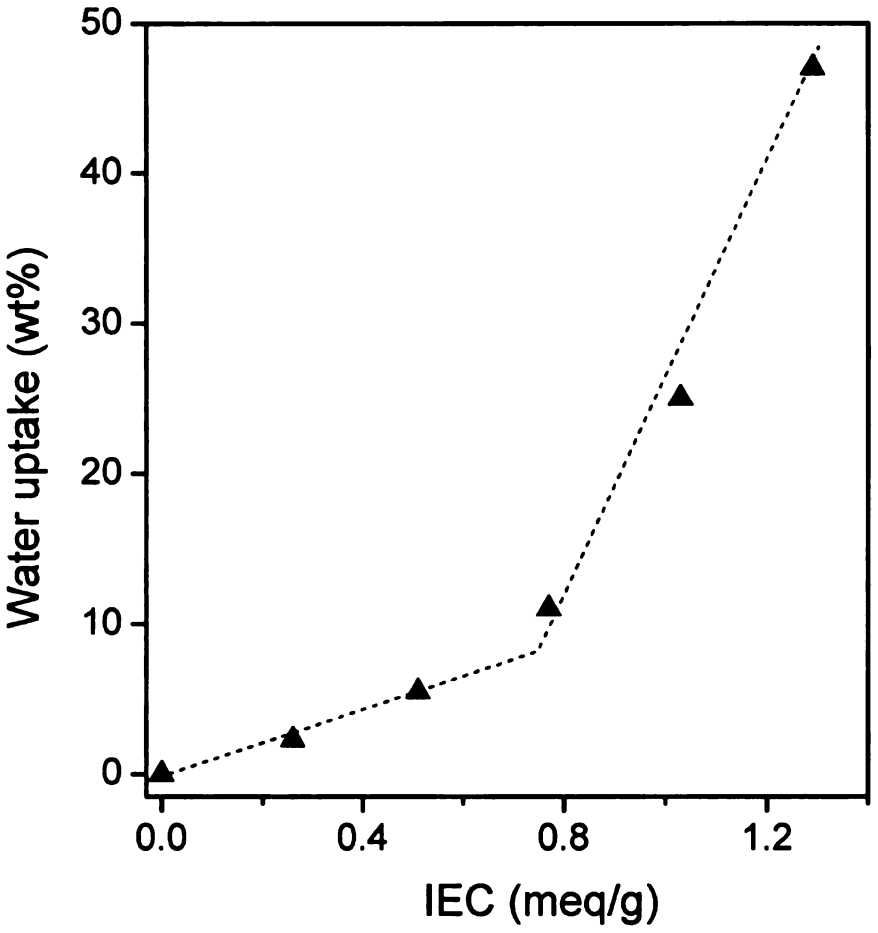

Figure 55. Water uptakes as a function of membrane IEC. The membrane water uptake was measured gravimetrically at room temperature. (The dotted lines are a guide to the eye)

Proton conductivity is one of the most important parameters for evaluating the performance of PEMs as well as the practicability of fuel cells. It is widely accepted that the proton conductivity of PEMs is strongly related to the number of charge carriers (H^+), so an ideal membrane would have a high sulfonic acid content without sacrificing the PEMs' mechanical properties. The conductivity tests were conducted with the cell submersed in Milli-Q water (100% RH), and

proton conductivities were measured for the series of blend membranes as a function of the weight fraction of SPI (**Figure 56**). Pure PVDF membranes (0 wt% SPI) and blend membranes with <30 wt% SPI fraction had no measurable proton conductivity, which is consistent with isolated ionic clusters. However, beginning at 30 wt% SPI, the presumed percolation threshold, proton conductivity increased linearly from 7 to 75 mS/cm at 50 wt% SPI.

The proton conductivity of Nafion 117 was measured as a control for conductivity experiments. At room temperature, the conductivity of Nafion 117 was 62 mS/cm, which is reasonably close to the reported conductivity data (60 mS/cm) for Nafion 117 at room temperature.[207] The proton conductivity of a 50 wt% SPI blend PEM was higher than Nafion 117 at both room temperature and 60 °C. The high conductivity of the blend membranes is consistent with a continuous proton conducting SPI phase separated from the hydrophobic PVDF analogous to Nafion 117.[11]

The proton conductivity of blend membranes and Nafion 117 were relatively low at room temperature but increased rapidly as the temperature was raised to 60 °C. The elevation of temperature might have stimulated the dynamics of proton transport and structural reorganization, which favors fast proton conduction.[216] Moreover, temperature increase might activate both the proton diffusion and molecular diffusion leading to improved proton conductivities at high temperatures.[216]

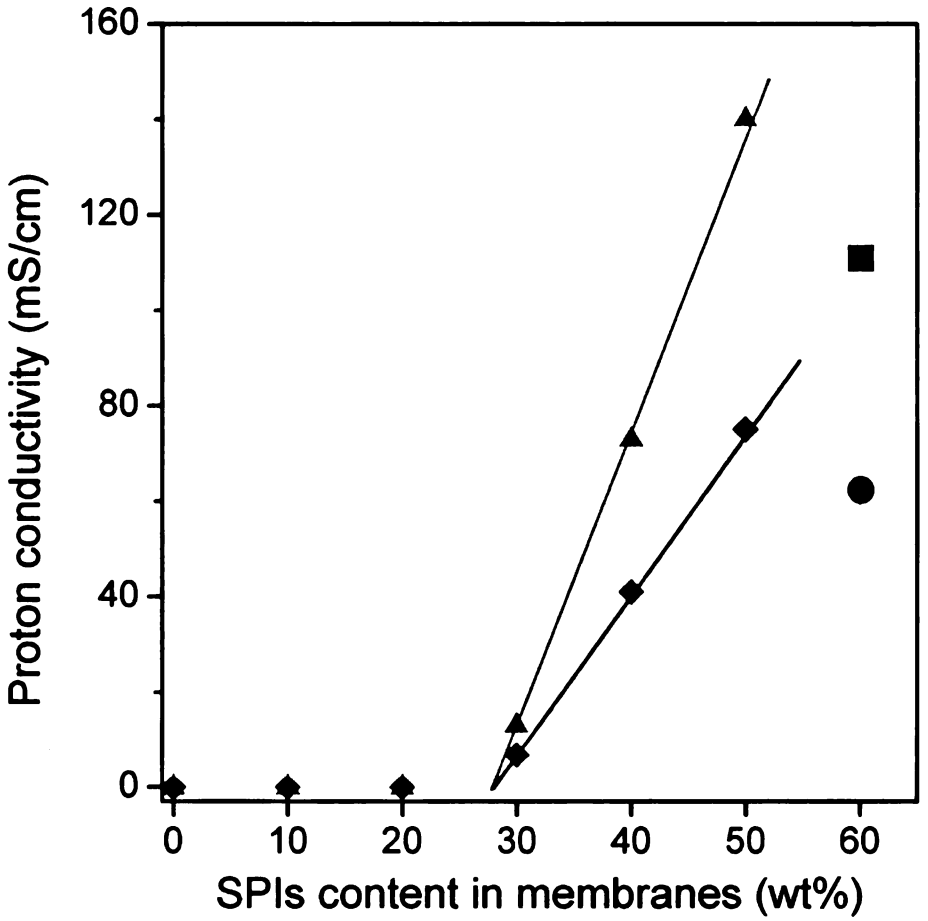

Figure 56. Blend membrane proton conductivity as a function of SPI content for composite PEMs at 100 % RH and room temperature (◆) and 60 °C (▲). Data for Nafion 117 at room temperature (●) and at 60 °C (■) was shown for comparison. (The lines are a guide to the eye)

Proton conductivity is strongly correlated to the IEC and generally the proton conductivity of PEMs increase with the IEC. **Figure 57** shows the proton conductivity as a function of membrane IEC. As with the water uptake data, there is an apparent percolation threshold at ~ 0.7 meq/g, followed by a linear increase in conductivity with increasing IEC.

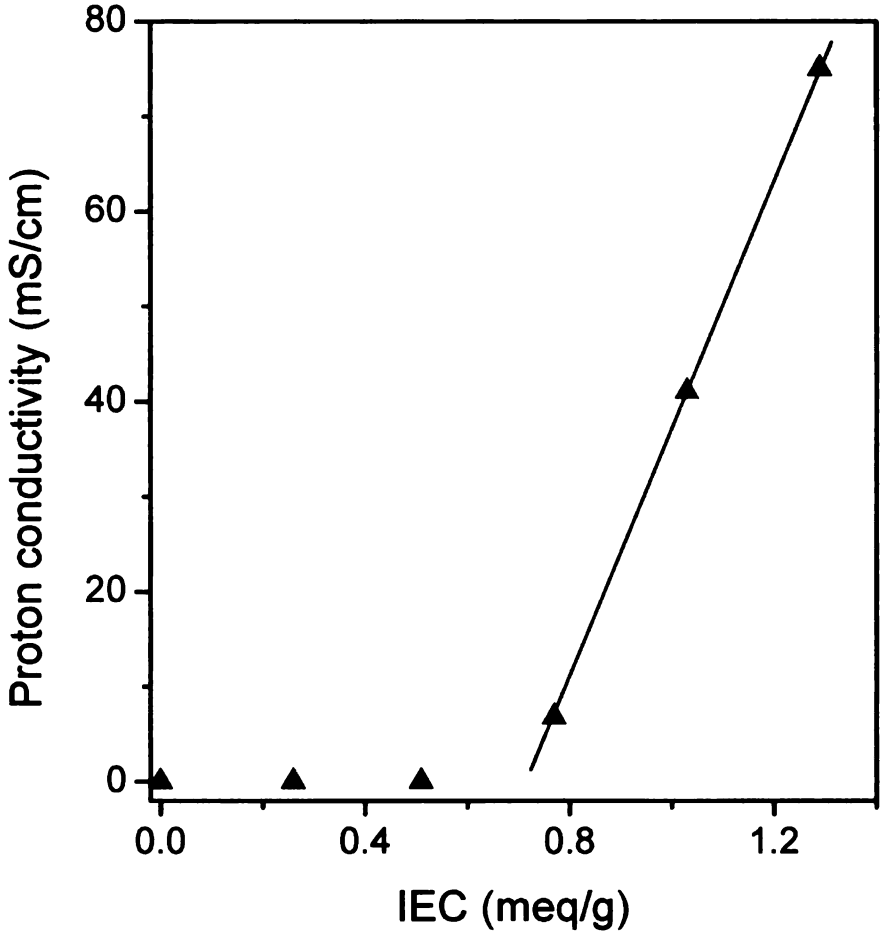

Figure 57. Membrane proton conductivity (room temperature, 100 % RH) as a function of IEC. (The line is a guide to the eye)

It was of great interest to investigate the proton conductivity vs water uptake, as water molecules were needed as the mobile phase to facilitate proton transport. As demonstrated in **Figure 58**, there was an almost linear increasing relationship between proton conductivity and water uptake above ~10 wt%, which was assumed to be the percolation threshold.

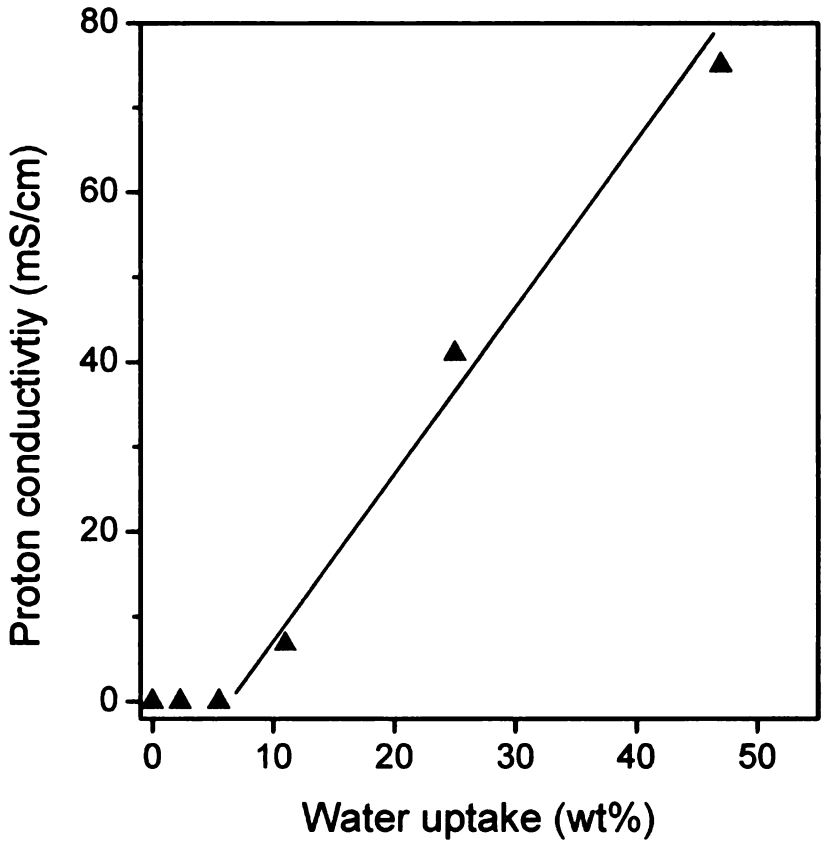

Figure 58. Blend membrane proton conductivity (room temperature, 100 % humidity) as a function of water uptake. (The lines are a guide to the eye)

The nature of acid groups, chemical composition, and membrane microstructure all contribute to the properties of PEMs. To obtain direct morphologic information, ~100-nm-thick cross-sectional slices of blend membranes were analyzed by TEM. **Figure 59** displays images of SPI/PVDF blend membranes with different blending ratios. After staining with Ag^+, the SPI appears as dark regions, while the matrix material, PVDF, is bright. A phase-separated morphology was seen for all compositions. Blend membranes with 10 - 30 wt% SPI show randomly distributed ionic domains; the domain size seems constant, but the areal density of domains increases. TEM images of membranes with >30 wt% SPI content show ionic domains interconnected into a continuous

network. The images in **Figures 59c** and **Figures 59d** provide direct evidence for a percolation phenomenon near 30 wt% SPI. The TEM image of a membrane with 40 wt% SPI content shows an apparent bicontinuous morphology with conducting paths for proton transport, which is consistent with the conductivity and water uptake studies. The ionic domains have sizes of 30-100 nm. A finer phase-separated morphology was found in the 50 wt% SPI blend membrane, and the domain size dropped to 20-40 nm. Scattered black dots seen in most images are likely silver oxide clusters generated through the photolysis of silver nitrate, which was applied for staining blend membranes. While the cross-sectional TEM images provide direct evidence for a phase-separated structure in dried membranes, water saturated membranes might have different ionic domain sizes or domain connections.

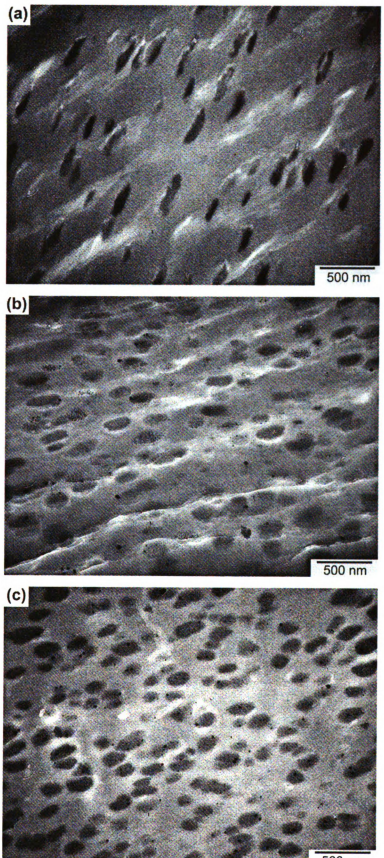
(a)
500 nm
(b)
500 nm
(c)
500 nm

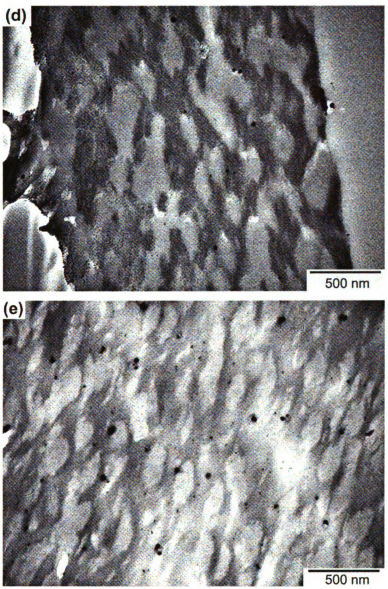

Figure 59. Cross-sectional TEM images of blend membranes with different SPI content: **(a)** 10 wt%; **(b)** 20 wt%; **(c)** 30 wt%; **(d)** 40 wt%; and **(e)** 50 wt%.

As PEMs are used as not only a proton conductor but also a separator to prevent the mixing of fuels with the oxidant, PEMs cannot have pin holes, which will allow permeation of fuels. We used SEM to obtain the surface microstructure of blend membranes that had been kept in water for over a week, and then dried (**Figure 60**). No holes were seen for any compositions. The SEM image of the

membrane with 10 wt% SPI content shows a homogeneous surface structure. The roughness of the blend membrane surfaces increases with the SPI content. The image in **Figure 60d** shows a spherical morphology in a 50 wt% SPI membrane. It is noteworthy that the SEM images were taken from the blend membranes which had been kept in water for over a week, implying that blend membranes are hydrolytically stable.

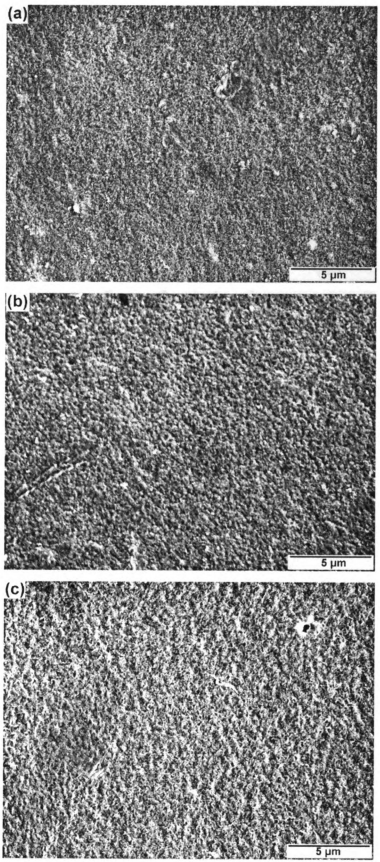
(a)
5 µm
(b)
5 µm
(c)
5 µm

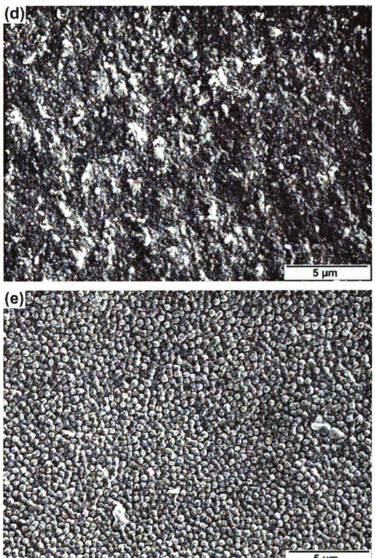

Figure 60. Surface SEM images of blend membranes with different SPI content: **(a)** 10 wt%; **(b)** 20 wt%; **(c)** 30 wt%; **(d)** 40 wt%; and **(e)** 50 wt%.

Ideally, PEMs should have high proton conductivity and minimal membrane swelling. Membrane dimensional stability was characterized by measuring the dimensional changes between the dry and water saturated states. Membranes that swell excessively can detach from the electrode surfaces as most electrodes do not swell, resulting in mechanical stress.[208] As illustrated in **Table 3**, Nafion 117 equilibrated in water increased 18 % in length compared to

the dry film. The severe expansion of Nafion 117 explains its poor performances in direct methanol fuel cells, as the permeability of Nafion to methanol is related to the high swelling of Nafion in water. However, all of the blend membranes swelled <3 %. The very low water swelling behavior may be due to the rigid matrix of crystalline PVDF, which suppressed the water swelling of SPI in hydrated membranes.

Conclusion

A SPI with a 100 % degree of sulfonation was prepared by the direct polycondensation reaction of a naphthalenic dianhydride monomer and a sulfonated diamine monomer, which avoided the disadvantages associated with "post-sulfonation" method. The chemical structure of the SPI was verified by ^{1}H NMR and FT-IR spectra. A series of tough and smooth proton conducting membranes were prepared using SPI to blend with PVDF followed by acidification, which revealed comparable or even higher proton conductivity than Nafion 117 at the same testing conditions. The proton conductivity and water uptake of blend membranes were proportional to the SPI content above the percolation threshold, which was confirmed by TEM cross-sectional images. Membranes with higher SPI content also showed a coarser surface morphology. The blend membranes showed a high dimensional stability which might be due to the rigid hydrophobic PVDF matrix. This blend membrane system is more cost effective compared to Nafion due to much easier synthesis and processing.

Experimental Section

Materials

Unless otherwise specified, all chemicals and solvents were ACS reagent grade and used as received from commercial suppliers without further purification. Dimethyl sulfoxide (DMSO) was dried over activated 4 Å molecular sieves, and triethylamine (TEA) and *m*-cresol were distilled before use. 4,4'-Diamino-biphenyl 2,2'-disulfonic acid (BDSA), received from TCI, was purple. BDSA was dissolved in an aqueous TEA and then precipitated upon addition of 1M HCl BDSA. The process was repeated until BDSA was obtained as a white solid, and then it was dried under vacuum at 70 °C overnight prior to use. Nafion 117, PVDF (M_w = 534,000 Da), and 1,4,5,8-naphthalene tetracarboxylic dianhydride (NTDA) were purchased from Sigma-Aldrich. NTDA and benzoic acid were dried under vacuum at 170 °C and 60 °C overnight, respectively, prior to the polycondensation reaction.

Synthesis of sulfonated polyimide (SPI)

Under N_2, BDSA (0.69 g, 2mmol), TEA (0.7 mL, 5 mmol), and *m*-cresol (6 mL) were added to a 100 mL three-neck round bottom flask and were vigorously stirred with a mechanical stirrer. After the BDSA was completely dissolved, NTDA (0.53g, 2 mmol) and benzoic acid (0.34 g, 2.8 mmol) were added. The reaction system was stirred at 80 °C for 4 h, and then additional *m*-cresol (20 mL) was added to dilute the viscous mixture. The reaction temperature was increased to 180 °C. After 14 h, the heating was discontinued, 100 mL of DMSO was added,

and the system was allowed to cool. The mixture was poured into 500 mL of ethyl acetate to precipitate the polymer. The crude polymer was isolated by filtration and was re-precipitated twice by dissolving the polymer in 100 mL of DMSO and precipitating into 500 mL of ethyl acetate. Finally, the sulfonated polyimide (SPI) was dried under vacuum at 80 °C overnight (1.1 g).

Film casting and membrane acidification

Blend membranes were fabricated by the solvent-casting method. This procedure describes the preparation of 10 mg membranes. Predetermined amounts of PVDF and SPI (triethylammonium salt) were dissolved in DMSO in separate vials. Each solution was fixed at 0.02 g/mL, and the total mass of the particles and PVDF was 10 mg. The two solutions were combined and stirred until the system was homogeneous. Membranes were solution-cast by pouring the mixture onto a clean glass plate, typically covering ~4x1 cm^2 area, and carefully dried with infrared heat at ~60 °C. After 3 hours, the membrane had turned translucent, and the glass plate was transferred to a vacuum at 80 °C for further drying overnight. The dried membranes (5-15 μm thick) were cut to size (~3×0.5-1 cm^2) and then removed from the substrate by immersing the plate in water. The as-synthesized membranes were soaked in 1 M HCl for 48 h to ensure that all sulfonate groups in the membranes were in their acidic form. The membranes were then washed extensively with water, and prior to conductivity tests, PEMs were stored in Milli-Q water.

Characterization.

^{1}H NMR analyses were performed at room temperature in deuterated dimethyl sulfoxide (DMSO) on a Varian UnityPlus 500 spectrometer at 500 MHz with the residual solvent proton signals as chemical shift standards. FT-IR spectra were acquired from a Mattson Galaxy 300 spectrometer purged with dry nitrogen, with the signal averaging 128 scans at a resolution of 4 cm^{-1}. All IR samples were dried, mixed with KBr, ground, and then pressed into pellets.

Thermogravimetric analyses (TGA) were carried out in air on Perkin-Elmer TGA 7 instruments at a heating rate of 10 °C/min. TGA samples were dried under vacuum at 80 °C overnight prior to use. Dried samples were held at 120 °C in the TGA apparatus for 30 min prior to initiating the run.

The microstructure of blend membranes was imaged using a JEOL-100CX transmittance electron microscope. To prepare membrane cross-sections for TEM analysis, membranes were immersed in 0.5 M $AgNO_3$ solution overnight to stain the ionic domains by ion exchange of sulfonic acid groups for silver. Samples were rinsed with water, and then dried under vacuum at 80 °C overnight. The stained membranes were embedded in epoxy resin, dried at 50 °C for 24 h, and then sectioned with an ultramicrotome to generate ~100 nm thick slices. The slices were picked up with copper grids for TEM analysis.

Conductivity measurements

The proton conductivities of membranes were measured with an alternating current (AC) impedance analyzer HP 4192A over the frequency range

from 5 Hz to 13 MHz. Membranes were placed between two Pt electrodes in a home-made Teflon cell. The entire setup was kept in Milli-Q water at controlled temperatures for at least 10 min to saturate membranes and then impedance was measured in in-plane direction. From the Nyquist plot, the resistance of the membrane was estimated, and then the conductivity of the membrane was calculated using the electrodes distance and membrane cross-sectional area, as shown in equation 1:

$$\sigma = \frac{L}{R \cdot A} \qquad (1)$$

Where σ is the conductivity of the membrane, L represents the distance between two electrodes, A stands for the membrane cross-sectional area, and R is the bulk membrane resistance estimated from the Nyquist plot.

Water uptake

Water uptake of all membranes was measured gravimetrically. After equilibration in Milli-Q water for two days at room temperature, membranes were removed from water, and weighed after the surface water was quickly removed by a Kim-wipe. Membranes were then dried under vacuum at 50 °C overnight and the weight of dried membrane was measured. The membrane water uptake was calculated according to equation 2:

$$\text{Water uptake} = \frac{W_{\text{wet}} - W_{\text{dry}}}{W_{\text{dry}}} \times 100\% \qquad (2)$$

where W_{wet} stands for the mass of wet membranes and W_{dry} represents the weight of dried membranes.

Dimensional stability

Membranes were saturated in Milli-Q water for two days at room temperature prior to measuring the dimensions of swollen membranes. After drying under vacuum at 50 °C overnight, the dimensions of the dried membrane were measured. The swelling ratio was calculated from the length (longest dimension) of the membrane, as shown in equation 3:

$$\text{Swelling ratio} = \frac{l_{wet} - l_{dry}}{l_{dry}} \times 100\% \qquad (3)$$

where l_{wet} and l_{dry} represent the lengths of wet and dried membranes, respectively. The uncertainty in the measurement is <3%.

Theoretic ion exchange capacity (IEC)

The ion exchange capacity (IEC) of membranes was calculated from the molecular weight of SPI repeating unit and SPI weight content in each membrane. The IEC was calculated as shown in equation 4:

$$\text{IEC} = \frac{m_{H^+}}{W_{dry}} \qquad (4)$$

where m_{H^+} expresses the quantity of sulfonic acid groups.

Chapter 5 Synthesis and characterization of poly(4-styrenephosphonate) for high temperature fuel cell application

Introduction

The proton exchange membrane (PEM) is one of the most important components of a fuel cell. It must have high proton conductivity, dimensional stability, controlled swelling in water, thermal and chemical stability, and low cost. These requirements place conflicting demands on materials, such as a high proton conductivity (favored by liquid-like materials) with dimensional stability, making it difficult to realize all desired features in a single material. A significant limitation of current PEMs is poor performance at elevated temperatures >100 °C and under low humidity conditions.

The primary challenge is the design of polymer morphologies that provide dynamic hydrogen bonding networks and high conductivities at low relative humidities, with retention of the physical characteristics required of practical membranes. Kreuer *et al.* have proposed criteria for proton conducting membranes that operate under anhydrous conditions: [217] (1) a high concentration of charge carriers, preferentially via self ionization (self dissociation), (2) a high dielectric constant, (3) and a dynamic hydrogen bonding network that facilitates proton transport without externally supplied water. A significant number of phosphonated membranes have been reported,[2,218-223] most following the design strategies previously used for sulfonic acids. There also have been several attempts to construct phosphonic acid-based membranes that satisfy the criteria

elucidated by Kreuer but the conductivities of the resulting membranes were modest.[224,225]

Compared to sulfonic acid-based polymers, the synthesis of phosphonated polymers is limited by the available phosphonation reagents and more complex synthetic procedures. In addition, high proton conductivities require a high degree of phosphonation because of the lower acidity of phosphonic acid than sulfonic acid. There are several reports on proton conductive polymers, in which phosphonic acid groups were connected to aromatic rings through alkylene linkers.[162,226] However, the benzylic alkylene spacer was very vulnerable to the oxidizing environment of fuel cells. Directly tethering phosphonic acids from aromatic ring would provide materials with greater thermal and chemical stability.

One route to phosphonated polymer materials is the direct polymerization of phosphonic acid-functionalized monomers. Nevertheless, because of side reactions, most attempts to polymerize phosphonic acid-functionalized monomers have resulted with oligomeric products.[227] Thus, post-polymerization functionalization of suitable aromatic polymers is a more practical route. A few procedures have been studied for introducing phosphonic functional groups into aromatic polymers. The Friedel-Crafts reaction with phosphorus trichloride as the starting material is one of the most common, efficient, and cost-effective procedures for the direct phosphonation of aromatic rings, but the reaction has poor selectivity and its application to polystyrene system led to cross-linked products.[227] There has been some success in creating direct aryl-phosphonate

functional groups in various polymers, such as poly(arylene ether), poly(phenylene oxide), and poly(phenylsulfone) by using the Michaelis-Arbuzov reaction and Pd(0)-catalyzed P–C coupling reaction.[220,221,227] However, purification of the polymer product and the expense of the Pd catalyst limits this approach.

Recently Allcock and coworkers reported the successful incorporation of phosphonic moieties into the aromatic rings of polyphosphazene by bromination, lithiation, and finally reaction with diethyl chlorophosphate.[228] In the present study, we use a similar strategy to prepare poly(4-styrenephosphonate) from brominated polystyrene and study its properties.

Results and discussion

The synthetic route to poly(4-styrene phosphonate) is shown in **Scheme 11**, The Cu(I) catalyze ATRP of 4-bromostyrene at 110 °C in xylenes was well-controlled. GPC analysis of the poly(4-bromostyrene) product after precipitation into methanol provided an M_n of 16,500 Da and a PDI of 1.01. To avoid inter- and intramolecular coupling of the polymer,[228] *n*-BuLi in THF at -78 °C was added dropwise to the THF solution containing poly(4-bromostyrene) at -78 °C. The addition of diethyl chlorophosphate provided the white phosphonated product after precipitation from THF into water, and cyclohexane, respectively. GPC analysis of the polymer showed a narrow molecular weight distribution (PDI=1.1) and a molecular weight (M_n = ~16,200 Da) comparable to the parent poly(4-

bromostyrene), consistent with negligible backbone cleavage and side reaction in the lithiation-phosphonation reaction.

Scheme 11. Synthesis route to poly(4-styrene phosphonate).

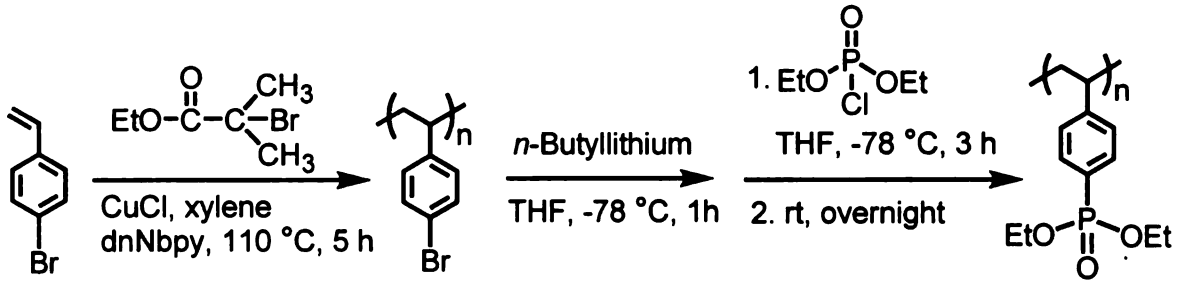

The ^{1}H NMR spectra of poly(4-bromostyrene) and poly(4-styrenephosphonate) are shown in **Figure 61**. The broad peaks in poly(4-bromostyrene) at ~6.3 and 7.2 ppm, associated with a *para*-substituted aromatic ring, shifted to 6.4 and 7.4 ppm after the phosphonation reaction. The peaks at 1.3 and 4.1 ppm corresponding to the phosphate-ester groups in poly(4-styrenephosphonate) were assigned to the methylene and methyl protons, separately. Integrations of peaks at 4.1 and 6.4 ppm indicate that ~80 % of the bromo groups have been phosphonated. **Figure 62** shows the ^{31}P NMR spectrum of poly(4-styrenephosphonate). The single resonance at ~19 ppm rules out intramolecular phosphonation

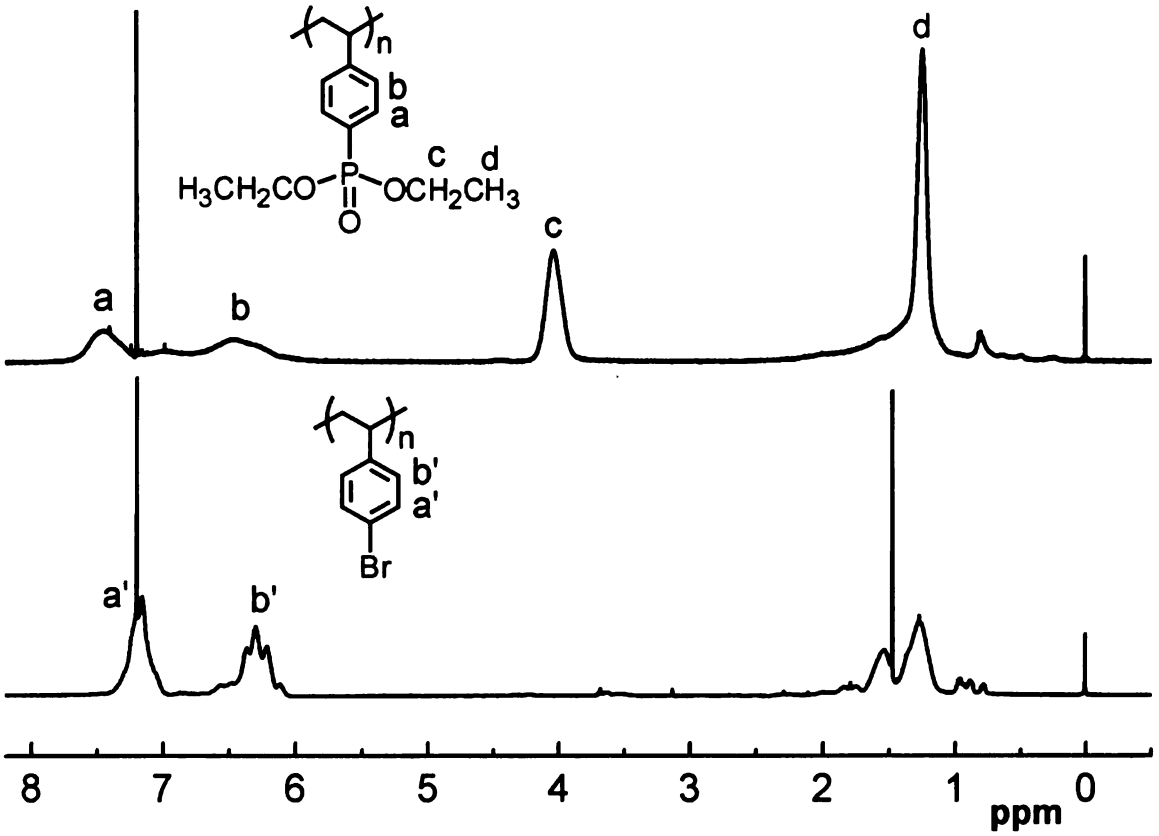

Figure 61. 1H NMR spectra of poly(4-bromostyrene) and poly(4-styrenephosphonate).

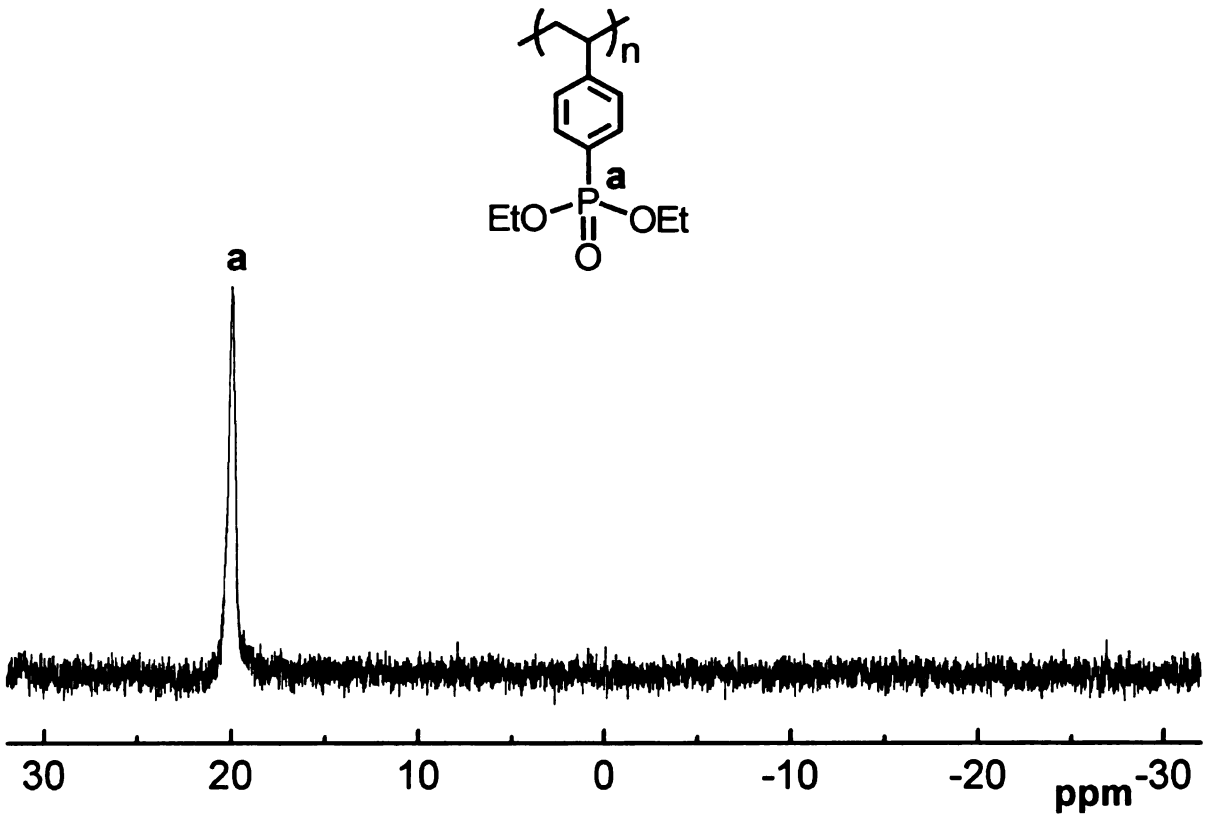

Figure 62. ^{31}P NMR spectrum of poly(4-styrenephosphonate).

The glass transition temperature (T_g) is related to the polymer free volume, and often correlates with transport of small molecules or ions. The DSC scan of poly(4-bromostyrene) showed a glass transition temperature (T_g) of 125 °C (**Figure 63**). The phosphonated product, poly(4-styrenephosphonate), revealed a T_g of 95 °C, which was ~30 °C lower than that of the parent polymer. The decrease in T_g in the phosphonated product might be due to the increase of free volume as the diethyl phosphonate group was bulkier than the bromo group.

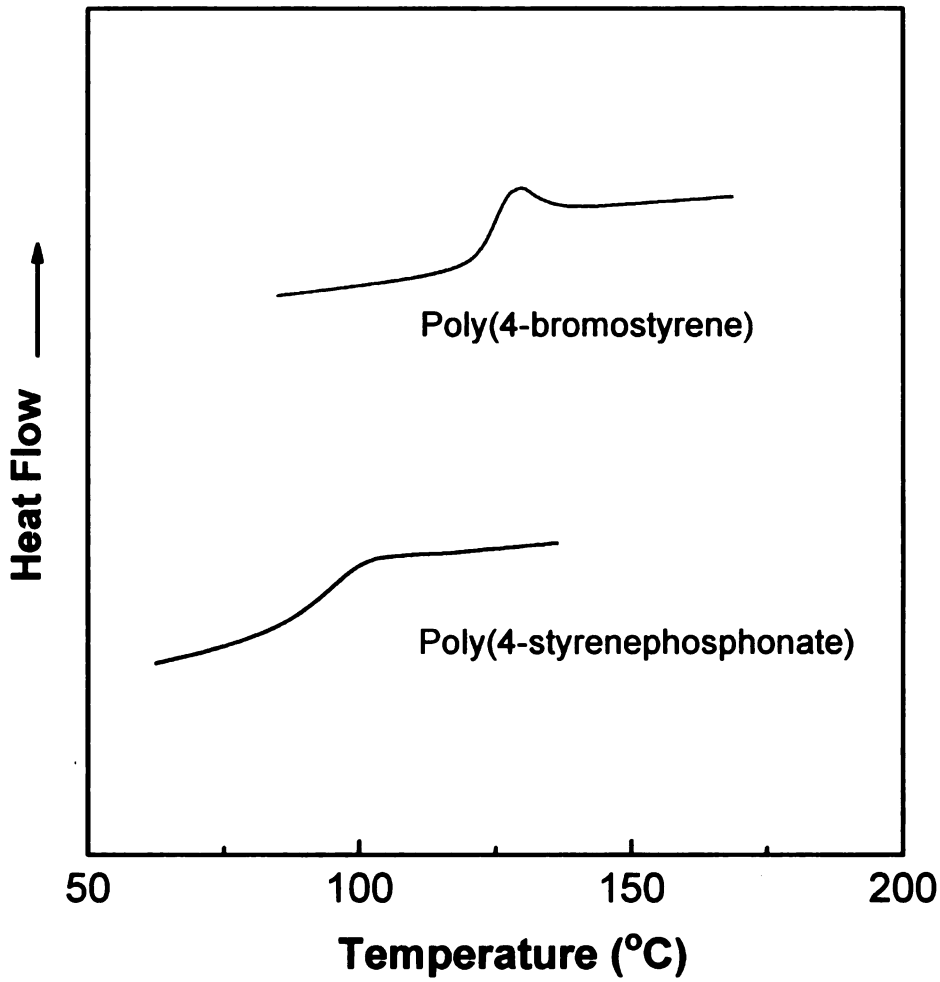

Figure 63. DSC analyses of poly(4-bromostyrene) and poly(4-styrenephosphonate). DSC samples were run in a nitrogen atmosphere at a heating rate of 10 °C/min.

Figure 64 shows FT-IR spectra that confirm the phosphonation reaction. Both poly(4-bromostyrene) and poly(4-styrenephosphonate) showed the expected absorption bands at 3200-3000 cm^{-1} and 3000-2800 cm^{-1} from aromatic and aliphatic C–H stretching vibrations, respectively. The two sharp absorption peaks of C–Br at 1010 and 1073 cm^{-1} are characteristic peaks of poly(4-bromostyrene). New absorption peaks due to the diethyl phosphonate groups are found in the spectrum of poly(4-styrenephosphonate). Absorption peaks at 1025

and 1052 cm^{-1} were both attributed to P–O and the peak at 1246 cm^{-1} to P=O, which confirmed the happening of the phosphonation reaction to poly(4-bromostyrene).

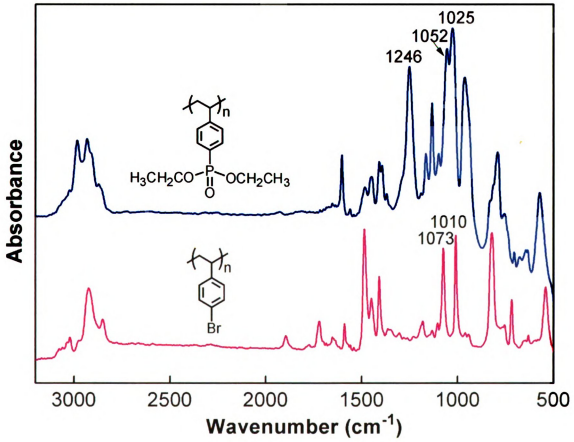

Figure 64. FTIR spectra of poly(4-bromostyrene) and poly(4-styrene phosphonate). Samples were made into pellets with KBr.

Figure 65 compares the thermal stability of the parent polymer and the phosphonated product. The TGA trace of poly(4-bromostyrene) indicated a dramatic mass loss at around 250 °C, which is likely due to depolymerization, and a minor weight loss occurred at 420 C, probably related to some crosslinking

during degradation. The TGA curve of poly(4-styrenephosphonate) exhibited three mass loss events. The initial mass loss started at about 230 °C and continued to about 270 °C, which might be attributed to the dissociation of diethyl phosphonate groups into free acid and ethylene. The second stage occurred between 270 and 295 °C due to the cross-linking of phosphonic acids in terms of P–O–P linkage forming anhydrides.[220] The last mass loss beginning at around 420 °C might result from the degradation of polymer backbone.

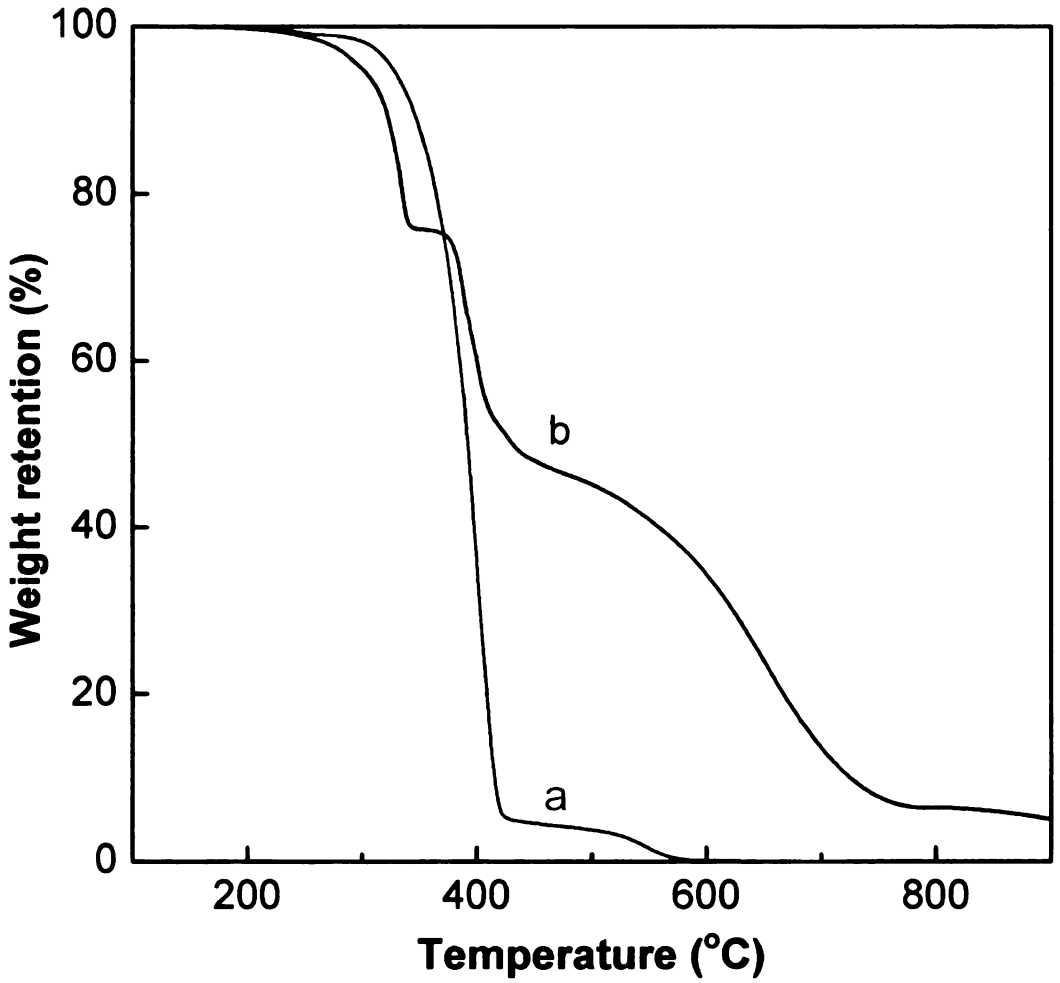

Figure 65. Thermogravimetric analysis of **(a)** poly(4-bromostyrene); and **(b)** poly(4-styrenephosphonate). All samples were run in an air atmosphere at a heating rate of 10 °C/min.

Conclusion

Poly(4-styrenephosphonate) was successfully prepared from poly(4-bromostyrene) via lithiation and subsequent phosphonation. The as-synthesized polymer was soluble in common organic solvents, such as THF. This approach generated phosphonated polymers with a high degree of phosphonation and no apparent side reactions. The phosphonated polymer might find its application in fuel cell applications at low humidity conditions.

Experimental Section

Materials

Unless otherwise specified, all chemicals and solvents were ACS reagent grade and used as received from commercial suppliers without further purification. *N*-Butyllithium (2.5 M in hexanes), 4,4'-dinonyl-2,2'-dipyridyl (dnNbpy), and 4-bromostyrene were obtained from Sigma-Aldrich. 4-Bromostyrene was passed through an activated basic alumina column followed by distillation prior to use. Tetrahydrofuran (THF) was distilled over sodium and benzophenone.

Characterization.

^{1}H NMR (500 MHz) spectroscopy was performed at room temperature in $CDCl_3$ solvent on a Varian UnityPlus 500 spectrometer with the residual solvent proton signals as chemical shift standards. ^{31}P NMR (121 MHz) spectra were obtained on a Varian UnityPlus 300 spectrometer. IR spectra were acquired from

a Mattson Galaxy 300 spectrometer purged with dry nitrogen, with the signal averaging 128 scans at a resolution of 4 cm^{-1}. All IR samples were dried, ground and mixed with KBr and then pressed into pellets.

Thermogravimetric analyses (TGA) were carried out in air on Perkin-Elmer TGA 7 instruments at a heating rate of 10 °C /min. TGA samples were dried under vacuum at 80 °C overnight prior to test. Dried samples were held at 120 °C in the TGA apparatus for 30 min before the heating proceeded. Differential scanning calorimetry (DSC) measurements were performed using a TA DSC Q100 with a heating/cooling rate of 10 °C /min under nitrogen.

Polymer molecular weights were measured by gel permeation chromatography (GPC) at 35 °C using two PLgel 10μ mixed-B columns in series with THF as the eluting solvent at a flow rate of 1 mL/min. A Waters 2410 differential refractometer was used as the detector. Mono-disperse polystyrene standards were used to calibrate the molecular weights.

Synthesis of poly(4-bromostyrene) by ATRP

To a 10 mL Schlenk flask equipped with a magnetic stirrer, were added 4-bromostyrene (4.5 mL, 34.4 mmol), ethyl 2-bromoisobutyrate (50 μL, 0.34 mmol), dnNbpy (0.42 g, 1.02 mmol), and xylenes (1.5 mL). After four freeze-pump-thaw cycles, the flask was backfilled with nitrogen and CuCl (34 mg, 0.34 mmol) was added. The mixture was degassed by three additional freeze-pump-thaw cycles, and then stirred at 110 °C for 5 h in a nitrogen atmosphere. The polymerization system was quickly cooled to room temperature, exposed to air, and diluted with

5 mL of xylenes. Precipitation from methanol gave poly(4-bromostyrene) as a white solid. The polymer was redissolved in THF and precipitated by the addition of methanol to remove impurities. Finally, the poly(4-bromostyrene) was dried under vacuum at 80 °C overnight.

Synthesis of poly(4-styrenephosphonate)

Under a nitrogen purge, *n*-butyllithium (5 mL, 12.5 mmol) was added dropwise to 250 mL of THF in a 1 L three-neck round bottom flask equipped with a magnetic stirrer and equilibrated at -78 °C. A THF solution (150 mL) of poly(4-bromostyrene) (0.32 g, 1.75 mmol repeating unit) was cooled to -78 °C and then transferred to the *n*-butyllithium solution via cannula. The mixture was held at -78 °C for 1 h and then diethyl chlorophosphate (3.9 mL, 27 mmol) was injected dropwise. After an additional 3 h at -78 °C, the reaction mixture was allowed to warm to room temperature overnight. The crude polymer was collected by filtering the reaction mass, condensing the THF solution, and then precipitating into water. The polymer was purified by precipitating from THF into water and cyclohexane, respectively. Finally, the solid polymer was dried under vacuum at 50 °C overnight.

References

(1) Einsla, B. R.; Kim, Y. S.; Hickner, M. A.; Hong, Y. T.; Hill, M. L.; Pivovar, B. S.; McGrath, J. E. *J. Membr. Sci.* **2005**, *255*, 141-148.

(2) Hickner, M. A.; Ghassemi, H.; Kim, Y. S.; Einsla, B. R.; McGrath, J. E. *Chem. Rev.* **2004**, *104*, 4587-4611.

(3) Kerres, J. A. *J. Membr. Sci.* **2001**, *185*, 3-27.

(4) Mauritz, K. A.; Moore, R. B. *Chem. Rev.* **2004**, *104*, 4535-4585.

(5) Hsu, W. Y.; Gierke, T. D. *Macromolecules* **1982**, *15*, 101-105.

(6) Gierke, T. D.; Munn, G. E.; Wilson, F. C. *J. Polym. Sci. Pt. B-Polym. Phys.* **1981**, *19*, 1687-1704.

(7) Hsu, W. Y.; Gierke, T. D. *J. Membr. Sci.* **1983**, *13*, 307-326.

(8) Rubatat, L.; Rollet, A. L.; Gebel, G.; Diat, O. *Macromolecules* **2002**, *35*, 4050-4055.

(9) Rubatat, L.; Gebel, G.; Diat, O. *Macromolecules* **2004**, *37*, 7772-7783.

(10) Rollet, A. L.; Diat, O.; Gebel, G. *J. Phys. Chem. B* **2002**, *106*, 3033-3036.

(11) Schmidt-Rohr, K.; Chen, Q. *Nat. Mater.* **2008**, *7*, 75-83.

(12) Roche, E. J.; Pineri, M.; Duplessix, R.; Levelut, A. M. *J. Polym. Sci. Pt. B-Polym. Phys.* **1981**, *19*, 1-11.

(13) Choi, P.; Jalani, N. H.; Datta, R. *J. Electrochem. Soc.* **2005**, *152*, E123-E130.

(14) Zhao, C. J.; Li, X. F.; Wang, Z.; Dou, Z. Y.; Zhong, S. L.; Na, H. *J. Membr. Sci.* **2006**, *280*, 643-650.

(15) Chuy, C.; Ding, J. F.; Swanson, E.; Holdcroft, S.; Horsfall, J.; Lovell, K. V. *J. Electrochem. Soc.* **2003**, *150*, E271-E279.

(16) Zaluski, C.; Xu, G. *Macromolecules* **1994**, *27*, 6750-6754.

(17) Jagur-Grodzinski, J. *Polym. Adv. Technol.* **2007**, *18*, 785-799.

(18) Flint, S. D.; Slade, R. C. T. *Solid State Ion.* **1997**, *97*, 299-307.

(19) Pereira, F.; Valle, K.; Belleville, P.; Morin, A.; Lambert, S.; Sanchez, C. *Chem. Mat.* **2008**, *20*, 1710-1718.

(20) Tang, H. L.; Pan, M. *J. Phys. Chem. C* **2008**, *112*, 11556-11568.

(21) Yuan, J. J.; Pu, H. T.; Yang, Z. L. *J. Polym. Sci. Pol. Chem.* **2009**, *47*, 2647-2655.

(22) Jin, Y. G.; Qiao, S. Z.; Zhang, L.; Xu, Z. P.; Smart, S.; da Costa, J. C. D.; Lu, G. Q. *J. Power Sources* **2008**, *185*, 664-669.

(23) Lin, Y. F.; Yen, C. Y.; Ma, C. C. M.; Liao, S. H.; Lee, C. H.; Hsiao, Y. H.; Lin, H. P. *J. Power Sources* **2007**, *171*, 388-395.

(24) Yen, C. Y.; Lee, C. H.; Lin, Y. F.; Lin, H. L.; Hsiao, Y. H.; Liao, S. H.; Chuang, C. Y.; Ma, C. C. M. *J. Power Sources* **2007**, *173*, 36-44.

(25) Kannan, A. G.; Choudhury, N. R.; Dutta, N. K. *J. Membr. Sci.* **2009**, *333*, 50-58.

(26) Chalkova, E.; Pague, M. B.; Fedkin, M. V.; Wesolowski, D. J.; Lvov, S. N. *J. Electrochem. Soc.* **2005**, *152*, A1035-A1040.

(27) Chalkova, E.; Fedkin, M. V.; Wesolowski, D. J.; Lvov, S. N. *J. Electrochem. Soc.* **2005**, *152*, A1742-A1747.

(28) Lepiller, C.; Gauthier, V.; Gaudet, J.; Pereira, A.; Lefevre, M.; Guay, D.; Hitchcock, A. *J. Electrochem. Soc.* **2008**, *155*, B70-B78.

(29) Jalani, N. H.; Dunn, K.; Datta, R. *Electrochim. Acta* **2005**, *51*, 553-560.

(30) Tang, H. L.; Pan, M.; Jiang, S. P.; Wan, Z. H.; Yuan, R. Z. *Colloid Surf. A-Physicochem. Eng. Asp.* **2005**, *262*, 65-70.

(31) Mu, S. C.; Tang, H. L.; Wan, Z. H.; Pan, M.; Yuan, R. Z. *Electrochem. Commun.* **2005**, *7*, 1143-1147.

(32) Pan, M.; Tang, H. L.; Jiang, S. P.; Liu, Z. C. *J. Electrochem. Soc.* **2005**, *152*, A1081-A1088.

(33) Uchida, H.; Mizuno, Y.; Watanabe, M. *J. Electrochem. Soc.* **2002**, *149*, A682-A687.

(34) Uchida, H.; Ueno, Y.; Hagihara, H.; Watanabe, M. *J. Electrochem. Soc.* **2003**, *150*, A57-A62.

(35) Zhang, W. J.; Li, M. K. S.; Yue, P. L.; Gao, P. *Langmuir* **2008**, *24*, 2663-2670.

(36) Sangeetha, D. *Eur. Polym. J.* **2005**, *41*, 2644-2652.

(37) Chuy, C.; Basura, V. I.; Simon, E.; Holdcroft, S.; Horsfall, J.; Lovell, K. V. *J. Electrochem. Soc.* **2000**, *147*, 4453-4458.

(38) Lee, W.; Kim, H.; Lee, H. *J. Membr. Sci.* **2008**, *320*, 78-85.

(39) Brijmohan, S. B.; Shaw, M. T. *Polymer* **2006**, *47*, 2856-2864.

(40) Gubler, L.; Prost, N.; Gursel, S. A.; Scherer, G. G. *Solid State Ion.* **2005**, *176*, 2849-2860.

(41) Gasa, J. V.; Boob, S.; Weiss, R. A.; Shaw, M. T. *J. Membr. Sci.* **2006**, *269*, 177-186.

(42) Ding, J. F.; Chuy, C.; Holdcroft, S. *Macromolecules* **2002**, *35*, 1348-1355.

(43) Ding, J. F.; Chuy, C.; Holdcroft, S. *Adv. Funct. Mater.* **2002**, *12*, 389-394.

(44) Ding, J. F.; Chuy, C.; Holdcroft, S. *Chem. Mat.* **2001**, *13*, 2231-2233.

(45) Shi, Z. Q.; Holdcroft, S. *Macromolecules* **2005**, *38*, 4193-4201.

(46) Sherazi, T. A.; Ahmad, S.; Kashmiri, M. A.; Kim, D. S.; Guiver, M. D. *J. Membr. Sci.* **2009**, *333*, 59-67.

(47) Li, D. R.; Chen, J. H.; Zhai, M. L.; Asano, M.; Maekawa, Y.; Oku, H.; Yoshida, M. *Nucl. Instrum. Methods Phys. Res. Sect. B-Beam Interact. Mater. Atoms* **2009**, *267*, 103-107.

(48) Huang, Y. F.; Hwang, B. J.; Lin, C. W. *J. Appl. Polym. Sci.* **2009**, *113*, 342-350.

(49) Choi, W. H.; Jo, W. H. *J. Power Sources* **2009**, *188*, 127-131.

(50) Zhang, Z. C.; Chalkova, E.; Fedkin, M.; Wang, C. M.; Lvov, S. N.; Komarneni, S.; Chung, T. C. M. *Macromolecules* **2008**, *41*, 9130-9139.

(51) Silva, A. L. A.; Takase, I.; Pereira, R. P.; Rocco, A. M. *Eur. Polym. J.* **2008**, *44*, 1462-1474.

(52) Sahu, A. K.; Selvarani, G.; Bhat, S. D.; Pitchumani, S.; Sridhar, P.; Shukla, A. K.; Narayanan, N.; Banerjee, A.; Chandrakumar, N. *J. Membr. Sci.* **2008**, *319*, 298-305.

(53) Rao, S. S.; Ojha, P. K.; Rath, S. K.; Palla, K. B.; Patri, M. *J. Appl. Polym. Sci.* **2008**, *110*, 2041-2046.

(54) Qiu, J. Y.; Zhao, L.; Zhai, M. L.; Ni, J. F.; Zhou, H. H.; Peng, J.; Li, J. Q.; Wei, G. S. *J. Power Sources* **2008**, *177*, 617-623.

(55) Fu, R. Q.; Woo, J. J.; Seo, S. J.; Lee, J. S.; Moon, S. H. *J. Membr. Sci.* **2008**, *309*, 156-164.

(56) Lin, C. W.; Huang, Y. F.; Kannan, A. M. *J. Power Sources* **2007**, *164*, 449-456.

(57) Elabd, Y. A.; Napadensky, E.; Walker, C. W.; Winey, K. I. *Macromolecules* **2006**, *39*, 399-407.

(58) Miyatake, K.; Zhou, H.; Matsuo, T.; Uchida, H.; Watanabe, M. *Macromolecules* **2004**, *37*, 4961-4966.

(59) Zheng, G. W.; Gong, C. L.; Wen, S.; Xie, X. L. *Acta Phys.-Chim. Sin.* **2008**, *24*, 855-860.

(60) Wang, L.; Yi, B. L.; Zhang, H. M.; Xing, D. M. *J. Phys. Chem. B* **2008**, *112*, 4270-4275.

(61) Shu, Y. C.; Chuang, F. S.; Tsen, W. C.; Chow, J. D.; Gong, C.; Wen, S. *J. Appl. Polym. Sci.* **2008**, *108*, 1783-1791.

(62) Zhang, G. M.; Guo, X. X.; Fang, J. H.; Chen, K. C.; Okamoto, K. I. *J. Membr. Sci.* **2009**, *326*, 708-713.

(63) Sutou, Y.; Yin, Y.; Hu, Z.; Chen, S.; Kita, H.; Okamoto, K.; Wang, H.; Kawasato, H. *J. Polym. Sci. Pol. Chem.* **2009**, *47*, 1463-1477.

(64) Chen, X. B.; Chen, P.; Okamoto, K. I. *J. Appl. Polym. Sci.* **2009**, *112*, 3560-3568.

(65) Chen, K. C.; Chen, X. B.; Yaguchi, K.; Endo, N.; Higa, M.; Okamoto, K. I. *Polymer* **2009**, *50*, 510-518.

(66) Zhu, X. L.; Pan, H. Y.; Liang, Y. F.; Jian, X. G. *Eur. Polym. J.* **2008**, *44*, 3782-3789.

(67) Zhao, L.; Huang, Y. D.; Song, Y. J.; Piao, Y. M. *e-Polymers* **2008**.

(68) Loredo, D. E. S.; Paredes, M. L.; Sena, M. E. *Mater. Lett.* **2008**, *62*, 3319-3321.

(69) Li, W. M.; Cui, Z. M.; Zhou, X. C.; Zhang, S. B.; Dai, L.; Xing, W. *J. Membr. Sci.* **2008**, *315*, 172-179.

(70) Li, N. W.; Cui, Z. M.; Zhang, S. B.; Li, S. H. *J. Polym. Sci. Pol. Chem.* **2008**, *46*, 2820-2832.

(71) Lee, C. H.; Park, C. H.; Lee, Y. M. *J. Membr. Sci.* **2008**, *313*, 199-206.

(72) Deligoz, H.; Vatansever, S.; Oksuzomer, F.; Koc, S. N.; Ozgumus, S.; Gurkaynak, M. A. *Polym. Adv. Technol.* **2008**, *19*, 1792-1802.

(73) Deligoz, H.; Vantansever, S.; Koc, S. N.; Oksuzomer, F.; Oezgumus, S.; Gurkaynak, M. A. *J. Appl. Polym. Sci.* **2008**, *110*, 1216-1224.

(74) Chen, X. B.; Yin, Y.; Chen, P.; Kita, H.; Okamoto, K. I. *J. Membr. Sci.* **2008**, *313*, 106-119.

(75) Wang, L.; Meng, Y. Z.; Wang, S. J.; Zhu, G. M. *Chem. J. Chin. Univ.-Chin.* **2007**, *28*, 1408-1410.

(76) Pinto, B. P.; Maria, L. C. D.; Sena, M. E. *Mater. Lett.* **2007**, *61*, 2540-2543.

(77) Li, Y. H.; Jin, R. Z.; Wang, Z.; Cui, Z. M.; Xing, W.; Gao, L. X. *J. Polym. Sci. Pol. Chem.* **2007**, *45*, 222-231.

(78) Li, Y. H.; Jin, R. Z.; Cui, Z. M.; Wang, Z.; Xing, W.; Qiu, X. P.; Ji, X. L.; Gao, L. X. *Polymer* **2007**, *48*, 2280-2287.

(79) Li, N. W.; Cui, Z. M.; Zhang, S. B.; Xing, W. *Polymer* **2007**, *48*, 7255-7263.

(80) Lee, S.; Jang, W.; Choi, S.; Tharanikkarasu, K.; Shul, Y.; Han, H. S. *J. Appl. Polym. Sci.* **2007**, *104*, 2965-2972.

(81) Hu, Z. X.; Yin, Y.; Chen, S. W.; Yamada, O.; Tanaka, K.; Kita, H.; Okamoto, K. *J. Polym. Sci. Pol. Chem.* **2006**, *44*, 2862-2872.

(82) Asano, N.; Miyatake, K.; Watanabe, M. *J. Polym. Sci. Pol. Chem.* **2006**, *44*, 2744-2748.

(83) Nakano, T.; Nagaoka, S.; Kawakami, H. *Polym. Adv. Technol.* **2005**, *16*, 753-757.

(84) Yin, Y.; Fang, J. H.; Watari, T.; Tanaka, K.; Kita, H.; Okamoto, K. *J. Mater. Chem.* **2004**, *14*, 1062-1070.

(85) Li, W.; Fu, Y. Z.; Manthiram, A.; Guiver, M. D. *J. Electrochem. Soc.* **2009**, *156*, B258-B263.

(86) Zhong, S. L.; Liu, C. G.; Na, H. *J. Membr. Sci.* **2009**, *326*, 400-407.

(87) Zhang, G.; Fu, T. Z.; Shao, K.; Li, X. F.; Zhao, C. J.; Na, H.; Zhang, H. *J. Power Sources* **2009**, *189*, 875-881.

(88) Norddin, M.; Ismail, A. F.; Rana, D.; Matsuura, T.; Tabe, S. *J. Membr. Sci.* **2009**, *328*, 148-155.

(89) Lin, C. K.; Kuo, J. F.; Chen, C. Y. *J. Power Sources* **2009**, *187*, 341-347.

(90) Fu, T. Z.; Zhong, S. L.; Cui, Z. M.; Zhao, C. J.; Shi, Y. H.; Yu, W. Z.; Na, H.; Xing, W. *J. Appl. Polym. Sci.* **2009**, *111*, 1335-1343.

(91) Colicchio, I.; Wen, F.; Keul, H.; Simon, U.; Moeller, M. *J. Membr. Sci.* **2009**, *326*, 45-57.

(92) Zhong, S. L.; Cui, X. J.; Fu, T. Z.; Na, H. *J. Power Sources* **2008**, *180*, 23-28.

(93) Zhao, C.; Li, X.; Lin, H.; Shao, K.; Na, H. *J. Appl. Polym. Sci.* **2008**, *108*, 671-680.

(94) Wang, J. L.; Song, Y. L.; Zhang, C.; Ye, Z. B.; Liu, H.; Lee, M. H.; Wang, D. H.; Ji, J. B. *Macromol. Chem. Phys.* **2008**, *209*, 1495-1502.

(95) Seo, D. W.; Park, H. S.; Choi, S. W.; Jeong, Y. G.; Hong, T. W.; Kim, W. G. *Polym. J.* **2008**, *40*, 979-985.

(96) Ramani, V.; Swier, S.; Shaw, M. T.; Weiss, R. A.; Kunz, H. R.; Fenton, J. M. *J. Electrochem. Soc.* **2008**, *155*, B532-B537.

(97) Park, H. S.; Seo, D. W.; Choi, S. W.; Jeong, Y. G.; Lee, J. H.; Il Kim, D.; Kim, W. G. *J. Polym. Sci. Pol. Chem.* **2008**, *46*, 1792-1799.

(98) Li, X. F.; De Feyter, S.; Vankelecom, I. F. J. *J. Membr. Sci.* **2008**, *324*, 67-75.

(99) Kim, D. S.; Guiver, M. D. *J. Polym. Sci. Pol. Chem.* **2008**, *46*, 989-1002.

(100) Hasani-Sadrabadi, M. M.; Emami, S. H.; Ghaffarian, R.; Moaddel, H. *Energy Fuels* **2008**, *22*, 2539-2542.

(101) Gasa, J. V.; Weiss, R. A.; Shaw, M. T. *J. Membr. Sci.* **2008**, *320*, 215-223.

(102) Fu, T. Z.; Wang, J.; Ni, J.; Cui, Z. M.; Zhong, S. L.; Zhao, C. J.; Na, H.; Xing, W. *Solid State Ion.* **2008**, *179*, 2265-2273.

(103) Fu, T. Z.; Cui, Z. M.; Zhong, S. L.; Shi, Y. H.; Zhao, C. J.; Zhang, G.; Shao, K.; Na, H.; Xing, W. *J. Power Sources* **2008**, *185*, 32-39.

(104) Do, K. N. T.; Kim, D. *J. Appl. Polym. Sci.* **2008**, *110*, 1763-1770.

(105) Zhong, S. L.; Cui, X. J.; Cai, H. L.; Fu, T. Z.; Zhao, C.; Na, H. *J. Power Sources* **2007**, *164*, 65-72.

(106) Zhao, C. J.; Wang, Z.; Bi, D. W.; Lin, H. D.; Shao, K.; Fu, T. Z.; Zhong, S. L.; Na, H. *Polymer* **2007**, *48*, 3090-3097.

(107) Li, X. F.; Zhang, G.; Xu, D.; Zhao, C. J.; Na, H. *J. Power Sources* **2007**, *165*, 701-707.

(108) Jung, H. Y.; Park, J. K. *Electrochim. Acta* **2007**, *52*, 7464-7468.

(109) Huang, M. Y.; Chen, H. Y.; Guo, J. Z.; Wang, Z. T.; Xu, L.; Wang, Y. X. *Acta Phys.-Chim. Sin.* **2007**, *23*, 44-49.

(110) Fu, Y. Z.; Manthiram, A.; Guiver, M. D. *Electrochem. Solid State Lett.* **2007**, *10*, B70-B73.

(111) Cai, H. L.; Shao, K.; Zhong, S. L.; Zhao, C. J.; Zhang, G.; Li, X. F.; Na, H. *J. Membr. Sci.* **2007**, *297*, 162-173.

(112) Zhong, S. L.; Liu, C. G.; Dou, Z. Y.; Li, X. F.; Zhao, C. J.; Fu, T. Z.; Na, H. *J. Membr. Sci.* **2006**, *285*, 404-411.

(113) Zhao, C. J.; Lin, H. D.; Shao, K.; Li, X. F.; Ni, H. Z.; Wang, Z.; Na, H. *J. Power Sources* **2006**, *162*, 1003-1009.

(114) Wu, H. L.; Ma, C. C. M.; Li, C. H.; Lee, T. M.; Chen, C. Y.; Chiang, C. L.; Wu, C. *J. Membr. Sci.* **2006**, *280*, 501-508.

(115) Wang, Z.; Li, X. F.; Zhao, C. J.; Ni, H. Z.; Na, H. *J. Power Sources* **2006**, *160*, 969-976.

(116) Mikhailenko, S. D.; Robertson, G. P.; Guiver, M. D.; Kaliaguine, S. *J. Membr. Sci.* **2006**, *285*, 306-316.

(117) Mecheri, B.; D'Epifanio, A.; Di Vona, M. L.; Traversa, E.; Licoccia, S.; Miyayama, M. *J. Electrochem. Soc.* **2006**, *153*, A463-A467.

(118) Liu, B. J.; Robertson, G. P.; Guiver, M. D.; Sun, Y. M.; Liu, Y. L.; Lai, J. Y.; Mikhailenko, S.; Kaliaguine, S. *J. Polym. Sci. Pt. B-Polym. Phys.* **2006**, *44*, 2299-2310.

(119) Fu, Y. Z.; Manthiram, A.; Guiver, M. D. *Electrochem. Commun.* **2006**, *8*, 1386-1390.

(120) Xing, D. M.; Yi, B. L.; Liu, F. Q.; Fu, Y. Z.; Zhang, H. M. *Fuel Cells* **2005**, *5*, 406-411.

(121) Li, X. F.; Liu, C. P.; Lu, H.; Zhao, C. J.; Wang, Z.; Xing, W.; Na, H. *J. Membr. Sci.* **2005**, *255*, 149-155.

(122) Karlsson, L. E.; Jannasch, P. *J. Membr. Sci.* **2004**, *230*, 61-70.

(123) Yang, Y. S.; Shi, Z. Q.; Holdcroft, S. *Macromolecules* **2004**, *37*, 1678-1681.

(124) Shahi, V. K. *Solid State Ion.* **2007**, *177*, 3395-3404.

(125) Zheng, G. W.; Gong, C. L.; Wen, S.; Zhou, H. B.; Xie, X. L. *Acta Phys.-Chim. Sin.* **2009**, *25*, 575-582.

(126) Ni, H. Z.; Wang, Z.; Chu, M. L.; Zhang, M. Y.; Na, H. *Acta Polym. Sin.* **2007**, 868-874.

(127) Wang, Z.; Ni, H. Z.; Zhao, C. J.; Zhang, M. Y.; Na, H. *J. Appl. Polym. Sci.* **2009**, *112*, 858-866.

(128) Takamuku, S.; Akizuki, K.; Abe, M.; Kanesaka, H. *J. Polym. Sci. Pol. Chem.* **2009**, *47*, 700-712.

(129) Qi, Y. H.; Gao, Y.; Tian, S. H.; Hlil, A. R.; Gaudet, J.; Guay, D.; Hay, A. S. *J. Polym. Sci. Pol. Chem.* **2009**, *47*, 1920-1929.

(130) Matsumoto, K.; Higashihara, T.; Ueda, M. *Macromolecules* **2009**, *42*, 1161-1166.

(131) Lee, J. K.; Li, W.; Manthiram, A. *J. Membr. Sci.* **2009**, *330*, 73-79.

(132) Feng, S. G.; Shang, Y. M.; Xie, X. F.; Wang, Y. Z.; Xu, J. M. *J. Membr. Sci.* **2009**, *335*, 13-20.

(133) Bai, Z.; Shumaker, J. A.; Houtz, M. D.; Mirau, P. A.; Dang, T. D. *Polymer* **2009**, *50*, 1463-1469.

(134) Badami, A. S.; Roy, A.; Lee, H. S.; Li, Y. X.; McGrath, J. E. *J. Membr. Sci.* **2009**, *328*, 156-164.

(135) Yang, J.; Li, Y. X.; Roy, A.; McGrath, J. E. *Polymer* **2008**, *49*, 5300-5306.

(136) Paul, M.; Park, H. B.; Freeman, B. D.; Roy, A.; McGrath, J. E.; Riffle, J. S. *Polymer* **2008**, *49*, 2243-2252.

(137) Schuster, M.; Kreuer, K. D.; Andersen, H. T.; Maier, J. *Macromolecules* **2007**, *40*, 598-607.

(138) Chang, B. J.; Kim, D. J.; Kim, J. H.; Lee, S. B.; Joo, H. J. *J. Membr. Sci.* **2008**, *325*, 989-996.

(139) Bae, B.; Miyatake, K.; Watanabe, M. *J. Membr. Sci.* **2008**, *310*, 110-118.

(140) Zhang, X. P.; Liu, S. Z.; Yin, J. *J. Polym. Sci. Pt. B-Polym. Phys.* **2006**, *44*, 665-672.

(141) Zhang, X. P.; Liu, S. Z.; Yin, J. *J. Membr. Sci.* **2006**, *275*, 119-126.

(142) Liu, D.; Kyriakides, S.; Case, S. W.; Lesko, J. J.; Li, Y. X.; McGrath, J. E. *J. Polym. Sci. Pt. B-Polym. Phys.* **2006**, *44*, 1453-1465.

(143) Olson, D. A.; Chen, L.; Hillmyer, M. A. *Chem. Mat.* **2008**, *20*, 869-890.

(144) Yu, X.; Roy, A.; Dunn, S.; Badami, A. S.; Yang, J.; Good, A. S.; McGrath, J. E. *J. Polym. Sci. Pol. Chem.* **2009**, *47*, 1038-1051.

(145) Ghassemi, H.; McGrath, J. E.; Zawodzinski, T. A. *Polymer* **2006**, *47*, 4132-4139.

(146) Roy, A.; Hickner, M. A.; Yu, X.; Li, Y. X.; Glass, T. E.; McGrath, J. E. *J. Polym. Sci. Pt. B-Polym. Phys.* **2006**, *44*, 2226-2239.

(147) Wang, H.; Badami, A. S.; Roy, A.; McGrath, J. E. *J. Polym. Sci. Pol. Chem.* **2007**, *45*, 284-294.

(148) Li, Y. X.; Roy, A.; Badami, A. S.; Hill, M.; Yang, J.; Dunn, S.; McGrath, J. E. *J. Power Sources* **2007**, *172*, 30-38.

(149) Lee, H. S.; Badami, A. S.; Roy, A.; McGrath, J. E. *J. Polym. Sci. Pol. Chem.* **2007**, *45*, 4879-4890.

(150) Roy, A.; Yu, X.; Dunn, S.; McGrath, J. E. *J. Membr. Sci.* **2009**, *327*, 118-124.

(151) Badami, A. S.; Lane, O.; Lee, H. S.; Roy, A.; McGrath, J. E. *J. Membr. Sci.* **2009**, *333*, 1-11.

(152) Roy, A.; Lee, H. S.; McGrath, J. E. *Polymer* **2008**, *49*, 5037-5044.

(153) Nakabayashi, K.; Matsumoto, K.; Ueda, M. *J. Polym. Sci. Pol. Chem.* **2008**, *46*, 3947-3957.

(154) Nakabayashi, K.; Matsumoto, K.; Higashihara, T.; Ueda, M. *J. Polym. Sci. Pol. Chem.* **2008**, *46*, 7332-7341.

(155) Matsumoto, K.; Ozaki, F.; Matsuoka, H. *J. Polym. Sci. Pol. Chem.* **2008**, *46*, 4479-4485.

(156) Lee, H. S.; Roy, A.; Lane, O.; Dunn, S.; McGrath, J. E. *Polymer* **2008**, *49*, 715-723.

(157) Okazaki, Y.; Nagaoka, S.; Kawakami, H. *J. Polym. Sci. Pt. B-Polym. Phys.* **2007**, *45*, 1325-1332.

(158) Zou, L.; Anthamatten, M. *J. Polym. Sci. Pol. Chem.* **2007**, *45*, 3747-3758.

(159) Park, M. J.; Downing, K. H.; Jackson, A.; Gomez, E. D.; Minor, A. M.; Cookson, D.; Weber, A. Z.; Balsara, N. P. *Nano Lett.* **2007**, *7*, 3547-3552.

(160) Tsang, E. M. W.; Zhang, Z.; Shi, Z.; Soboleva, T.; Holdcroft, S. *J. Am. Chem. Soc.* **2007**, *129*, 15106.

(161) Di Vona, M. L.; Sgreccia, E.; Licoccia, S.; Khadhraoui, M.; Denoyel, R.; Knauth, P. *Chem. Mat.* **2008**, *20*, 4327-4334.

(162) Cho, C. G.; Kim, S. H.; Park, Y. C.; Kim, H.; Park, J. W. *J. Membr. Sci.* **2008**, *308*, 96-106.

(163) Robeson, L. M.; Hwu, H. H.; McGrath, J. E. *J. Membr. Sci.* **2007**, *302*, 70-77.

(164) Kim, D. H.; Choi, J.; Hong, Y. T.; Kim, S. C. *J. Membr. Sci.* **2007**, *299*, 19-27.

(165) Compan, V.; Fernandez-Carretero, F. J.; Riande, E.; Linares, A.; Acosta, J. L. *J. Electrochem. Soc.* **2007**, *154*, B159-B164.

(166) Wu, H. L.; Ma, C. C. M.; Liu, F. Y.; Chen, C. Y.; Lee, S. J.; Chiang, C. L. *Eur. Polym. J.* **2006**, *42*, 1688-1695.

(167) Swier, S.; Shaw, M. T.; Weiss, R. A. *J. Membr. Sci.* **2006**, *270*, 22-31.

(168) Gasa, J. V.; Weiss, R. A.; Shaw, M. T. *J. Polym. Sci. Pt. B-Polym. Phys.* **2006**, *44*, 2253-2266.

(169) Swier, S.; Ramani, V.; Fenton, J. M.; Kunz, H. R.; Shaw, M. T.; Weiss, R. A. *J. Membr. Sci.* **2005**, *256*, 122-133.

(170) Kerres, J. A. *Fuel Cells* **2005**, *5*, 230-247.

(171) Mokrini, A.; Huneault, M. A. *J. Power Sources* **2006**, *154*, 51-58.

(172) Piboonsatsanasakul, P.; Wootthikanokkhan, J.; Thanawan, S. *J. Appl. Polym. Sci.* **2008**, *107*, 1325-1336.

(173) Mokrini, A.; Huneault, M. A.; Gerard, P. *J. Membr. Sci.* **2006**, *283*, 74-83.

(174) Hong, L.; Chen, N. P. *J. Polym. Sci. Pt. B-Polym. Phys.* **2000**, *38*, 1530-1538.

(175) Fu, Y. Z.; Manthiram, A.; Guiver, M. D. *Electrochem. Commun.* **2007**, *9*, 905-910.

(176) Zhong, S. L.; Cui, X. J.; Cai, H. L.; Fu, T. Z.; Shao, K.; Na, H. *J. Power Sources* **2007**, *168*, 154-161.

(177) Mikhailenko, S. U. D.; Wang, K. P.; Kaliaguine, S.; Xing, P. X.; Robertson, G. P.; Guiver, M. D. *J. Membr. Sci.* **2004**, *233*, 93-99.

(178) Gao, J.; Lee, D.; Yang, Y. S.; Holdcroft, S.; Frisken, B. J. *Macromolecules* **2005**, *38*, 5854-5856.

(179) Oren, Y.; Freger, V.; Linder, C. *J. Membr. Sci.* **2004**, *239*, 17-26.

(180) Boob, S. B.; Shaw, M. T. *ANTEC* **2005**, 1731-1735.

(181) Brijmohan, S. B.; Shaw, M. T. *J. Membr. Sci.* **2007**, *303*, 64-71.

(182) Hou, J.; Baker, G. L. *Chem. Mat.* **1998**, *10*, 3311-3318.

(183) Qiao, J.; Chen, Y. Y.; Baker, G. L. *Chem. Mat.* **1999**, *11*, 2542-2547.

(184) Harrison, W. L.; Hickner, M. A.; Kim, Y. S.; McGrath, J. E. *Fuel Cells* **2005**, *5*, 201-212.

(185) Miyatake, K.; Watanabe, M. *J. Mater. Chem.* **2006**, *16*, 4465-4467.

(186) Pyun, J.; Matyjaszewski, K. *Chem. Mat.* **2001**, *13*, 3436-3448.

(187) Liu, T. Q.; Jia, S. J.; Kowalewski, T.; Matyjaszewski, K.; Casado-Portilla, R.; Belmont, J. *Macromolecules* **2006**, *39*, 548-556.

(188) Li, D. J.; Sheng, X.; Zhao, B. *J. Am. Chem. Soc.* **2005**, *127*, 6248-6256.

(189) Unsal, E.; Elmas, B.; Caglayan, B.; Tuncel, M.; Patir, S.; Tuncel, A. *Anal. Chem.* **2006**, *78*, 5868-5875.

(190) Bridger, K.; Vincent, B. *Eur. Polym. J.* **1980**, *16*, 1017-1021.

(191) Bridger, K.; Fairhurst, D.; Vincent, B. *J. Colloid Interface Sci.* **1979**, *68*, 190-195.

(192) Dorris, A.; Rucareanu, S.; Reven, L.; Barrett, C. J.; Lennox, R. B. *Langmuir* **2008**, *24*, 2532-2538.

(193) Radhakrishnan, B.; Ranjan, R.; Brittain, W. J. *Soft Matter* **2006**, *2*, 386-396.

(194) Zhang, X. H.; Hong, L.; Liu, Z. L.; Lee, J. Y. *Colloid Polym. Sci.* **2008**, *286*, 1351-1360.

(195) Wang, Y. P.; Pei, X. W.; He, X. Y.; Yuan, K. *Eur. Polym. J.* **2005**, *41*, 1326-1332.

(196) Matyjaszewski, K.; Miller, P. J.; Shukla, N.; Immaraporn, B.; Gelman, A.; Luokala, B. B.; Siclovan, T. M.; Kickelbick, G.; Vallant, T.; Hoffmann, H.; Pakula, T. *Macromolecules* **1999**, *32*, 8716-8724.

(197) Pyun, J.; Jia, S. J.; Kowalewski, T.; Patterson, G. D.; Matyjaszewski, K. *Macromolecules* **2003**, *36*, 5094-5104.

(198) Zhao, H. Y.; Kang, X. L.; Liu, L. *Macromolecules* **2005**, *38*, 10619-10622.

(199) Chen, X. Y.; Randall, D. P.; Perruchot, C.; Watts, J. F.; Patten, T. E.; von Werne, T.; Armes, S. P. *J. Colloid Interface Sci.* **2003**, *257*, 56-64.

(200) Vo, C. D.; Schmid, A.; Armes, S. P.; Sakai, K.; Biggs, S. *Langmuir* **2007**, *23*, 408-413.

(201) Han, S. J.; Hyeon, T. *Chem. Commun.* **1999**, 1955-1956.

(202) Jiang, D. D.; Yao, Q.; McKinney, M. A.; Wilkie, C. A. *Polym. Degrad. Stabil.* **1999**, *63*, 423-434.

(203) Summer, M. J.; Harrison, W. L.; Weyers, R. M.; Kim, Y. S.; McGrath, J. E.; Riffle, J. S.; Brink, A.; Brink, M. H. *J. Membr. Sci.* **2004**, *239*, 199-211.

(204) Wiles, K. B.; Wang, F.; McGrath, I. E. *J. Polym. Sci. Pol. Chem.* **2005**, *43*, 2964-2976.

(205) Kim, Y. S.; Hickner, M. A.; Dong, L. M.; Pivovar, B. S.; McGrath, J. E. *J. Membr. Sci.* **2004**, *243*, 317-326.

(206) Sankir, M.; Kim, Y. S.; Pivovar, B. S.; McGrath, J. E. *J. Membr. Sci.* **2007**, *299*, 8-18.

(207) Fontanella, J. J.; McLin, M. G.; Wintersgill, M. C.; Calame, J. P.; Greenbaum, S. G. *Solid State Ion.* **1993**, *66*, 1-4.

(208) Liu, D.; Yates, M. Z. *J. Membr. Sci.* **2009**, *326*, 539-548.

(209) Ge, J. P.; Hu, Y. X.; Biasini, M.; Dong, C. L.; Guo, J. H.; Beyermann, W. P.; Yin, Y. D. *Chem.-Eur. J.* **2007**, *13*, 7153-7161.

(210) Deng, Y. H.; Wang, C. C.; Hu, J. H.; Yang, W. L.; Fu, S. K. *Colloid Surf. A-Physicochem. Eng. Asp.* **2005**, *262*, 87-93.

(211) Wang, Y.; Teng, X. W.; Wang, J. S.; Yang, H. *Nano Lett.* **2003**, *3*, 789-793.

(212) Vestal, C. R.; Zhang, Z. J. *J. Am. Chem. Soc.* **2002**, *124*, 14312-14313.

(213) Xue, S. N.; Yin, G. P. *Polymer* **2006**, *47*, 5044-5049.

(214) Genies, C.; Mercier, R.; Sillion, B.; Cornet, N.; Gebel, G.; Pineri, M. *Polymer* **2001**, *42*, 359-373.

(215) Sumner, M. J.; Harrison, W. L.; Weyers, R. M.; Kim, Y. S.; McGrath, J. E.; Riffle, J. S.; Brink, A.; Brink, M. H. *J. Membr. Sci.* **2004**, *239*, 199-211.

(216) Jang, W.; Sundar, S.; Choi, S.; Shul, Y. G.; Han, H. *J. Membr. Sci.* **2006**, *280*, 321-329.

(217) Schuster, M.; Rager, T.; Noda, A.; Kreuer, K. D.; Maier, J. *Fuel Cells* **2005**, *5*, 355-365.

(218) Lafitte, B.; Jannasch, P. In *Advances in Fuel Cells*; Kreuer, K.-D., Nguyen, T., Zhao, T., Eds.; Elsevier: 2007; Vol. 1, p 119-185.

(219) Bock, T.; Mulhaupt, R.; Mohwald, H. *Macromol. Rapid Commun.* **2006**, *27*, 2065-2071.

(220) Subianto, S.; Choudhury, N. R.; Dutta, N. K. *J. Polym. Sci. Pol. Chem.* **2008**, *46*, 5431-5441.

(221) Bock, T.; Mohwald, H.; Mulhaupt, R. *Macromol. Chem. Phys.* **2007**, *208*, 1324-1340.

(222) Kreuer, K. D. *Chem. Mat.* **1996**, *8*, 610-641.

(223) Souzy, R.; Ameduri, B. *Prog. Polym. Sci.* **2005**, *30*, 644-687.

(224) Rager, T.; Schuster, M.; Steininger, H.; Kreuer, K. D. *Adv. Mater.* **2007**, *19*, 3317.

(225) Steininger, H.; Schuster, M.; Kreuer, K. D.; Maier, J. *Solid State Ion.* **2006**, *177*, 2457-2462.

(226) Itoh, T.; Hirai, K.; Tamura, M.; Uno, T.; Kubo, M.; Aihara, Y. *J. Power Sources* **2008**, *178*, 627-633.

(227) Jakoby, K.; Peinemann, K. V.; Nunes, S. P. *Macromol. Chem. Phys.* **2003**, *204*, 61-67.

(228) Allcock, H. R.; Hofmann, M. A.; Wood, R. M. *Macromolecules* **2001**, *34*, 6915-6921.